1992

Radiation induced flux pinning in YBa2Cu3O7-[delta] single crystal

Qiang Qian
Iowa State University

INFORMATION TO USERS

This manuscript has been reproduced from the microfilm master. UMI films the text directly from the original or copy submitted. Thus, some thesis and dissertation copies are in typewriter face, while others may be from any type of computer printer.

The quality of this reproduction is dependent upon the quality of the copy submitted. Broken or indistinct print, colored or poor quality illustrations and photographs, print bleedthrough, substandard margins, and improper alignment can adversely affect reproduction.

In the unlikely event that the author did not send UMI a complete manuscript and there are missing pages, these will be noted. Also, if unauthorized copyright material had to be removed, a note will indicate the deletion.

Oversize materials (e.g., maps, drawings, charts) are reproduced by sectioning the original, beginning at the upper left-hand corner and continuing from left to right in equal sections with small overlaps. Each original is also photographed in one exposure and is included in reduced form at the back of the book.

Photographs included in the original manuscript have been reproduced xerographically in this copy. Higher quality 6" x 9" black and white photographic prints are available for any photographs or illustrations appearing in this copy for an additional charge. Contact UMI directly to order.

U·M·I

University Microfilms International
A Bell & Howell Information Company
300 North Zeeb Road, Ann Arbor, MI 48106-1346 USA
313/761-4700 800/521-0600

Order Number 9311528

Radiation induced flux pinning in $YBa_2Cu_3O_{7-\delta}$ single crystal

Qian, Qiang, Ph.D.

Iowa State University, 1992

U·M·I
300 N. Zeeb Rd.
Ann Arbor, MI 48106

Radiation induced flux pinning in $YBa_2Cu_3O_{7-\delta}$ single crystal

by

Qiang Qian

A Dissertation Submitted to the

Graduate Faculty in Partial Fulfillment of the

Requirements for the Degree of

DOCTOR OF PHILOSOPHY

Department: Physics and Astronomy
Major: Solid State Physics

Approved:

Signature was redacted for privacy.

In Charge of Major Work

Signature was redacted for privacy.

For the Major Department

Signature was redacted for privacy.

For the Graduate College

Iowa State University
Ames, Iowa

1992

TABLE OF CONTENTS

CHAPTER 1. INTRODUCTION

The discovery of the first cupric oxide superconductor $La_{2-x}Ba_xCuO_{4-y}$ opened a new area of research because it was a new class of superconductor with unusually high T_c of 36 K [J. G. Bednorz and K. A. Muller, 1986]. Subsequent research led to the discovery of a related but different compound, $YBa_2Cu_3O_{7-\delta}$, with T_c around 93 K [Wu et al., 1987]. Many other cupric oxide high T_c superconductors were found since then, such as $RBa_2Cu_3O_{7-\delta}$ (R = Y, Nd, Sm, Eu, Gd, Dy, Ho, Er, Tm, Yb, and Lu), the Bi-Sr-Ca-Cu-O compounds, and the Tl-Ba-Ca-Cu-O compounds. This occurrence of superconductivity above LN_2 temperature (77 K) attracted a huge interest among both science community and general public with speculation of many potential applications.

One of the big obstacles limiting their application as high T_c superconductors was low critical current density, J_c, above LN_2 temperature. For example, the basal plane critical current density, J_c^{ab}, for $YBa_2Cu_3O_{7-\delta}$ is typically 5×10^5 A/cm^2 at 10 K and 1 T and almost zero at 77 K and 1 T for a single crystal sample. Therefore, the enhancement of the critical current density has become a very important area of research.

This dissertation is devoted to study the technique of J_c enhancement by 200 MeV proton irradiation with a special emphasis on the effects of anisotropy. The research is focused on J_c enhancement, the anisotropy of the J_c enhancement, annealing of J_c in room temperature after the enhancement and T_c suppression by the irradiation. Because there are many possible combinations of magnetic field direction, current direction, and irradiation direction relative to the two primary

crystallographic axes, the c axis and the a-b plane, the amount of data is considerably large. To limit the amount of measuring time, two temperatures, 10 K and 77 K, were selected as typical values to show the effects of the irradiation.

The dissertation is organized in the following way. In chapter 1, the general properties of conventional superconductors and high T_c superconductors are reviewed. In chapter 2, the theories that are related to this research such as Bean model and pinning theory are summarized. In chapter 3, the experimental techniques are presented including crystal growth and the irradiation. In chapter 4, the results of this experiment are discussed covering low fluence irradiation parallel to the a-b plane, high fluence irradiation parallel to the a-b plane and the c axis, and finally, the annealing of J_c at room temperature. In chapter 5, the conclusions of the experiment are stated.

1.1 Conventional Superconductors

In 1911, H. K. Onnes first observed that the resistivity of mercury fell sharply to zero at 4.15 K in a temperature interval of 0.01K [H. K. Onnes, 1911]. Since then, nearly half elements in the periodic table and many other metal compounds and alloys had been found to show this effect. Initially, zero resistivity was the distinguishing property of these so called superconductors. Indeed, detailed measurement of these superconductors found their resistivity were smaller than 10^{-21} Ω cm, the detectable limit. In 1933, Meissner and Ochsenfeld observed that perfect diamagnetism was also a property of the superconductors in that the magnetic flux was completely expelled out of the superconductors as samples were cooled below the superconducting transition temperature. This effect (Meissner

effect) is a unique property of the superconductors and distinguishes a superconductor from a perfect conductor. Zero resistivity and perfect diamagnetism are two characteristic properties of the superconductors.

Conventional superconductors are classified into two types. In the presence of a magnetic field H, a type I superconductor undergoes a first order phase transition from the superconducting to normal state when H increases to the thermal dynamic critical field H_c at which magnetic flux suddenly collapse into the sample. It is assumed here that the demagnetizing factor is negligible such for a long cylinder. As shown in Fig. 1.1a, the magnetization of the type I superconductor is perfectly diamagnetic when the field H is below H_c and suddenly becomes paramagnetic when the H increases to H_c. The typical type I superconductors are pure single element materials such as lead, tin, zinc, etc., which have a coherent length ξ much larger than the magnetic penetration depth λ. Fig 1.2a shows a phase diagram for a typical type I superconductor. By contrast, a type II superconductor has a more gradual phase transition. The magnetic flux begins to penetrates some region of the type II superconductor in form of vortices as the field H increases to a lower critical field H_{c1} and gradually penetrates entire sample as the H increases to a upper critical field H_{c2}. The transitions at H_{c1} and H_{c2} are both second order. As shown in Fig. 1.1b, the magnetization of the type II superconductor is also perfectly diamagnetic when the field H is below H_{c1}, however it becomes partially diamagnetic when H is between H_{c1} and H_{c2}, and finally becomes normal when H is larger than H_{c2}. Although the magnetic flux partially penetrates the sample for $H_{c1} \leq H \leq H_{c2}$, the superconductor remains zero resistivity electronically as long as the vortices don't move. For $0 \leq H \leq H_{c1}$, it is called Meissner state; for $H_{c1} \leq H \leq H_{c2}$, it is called vortex state; and for

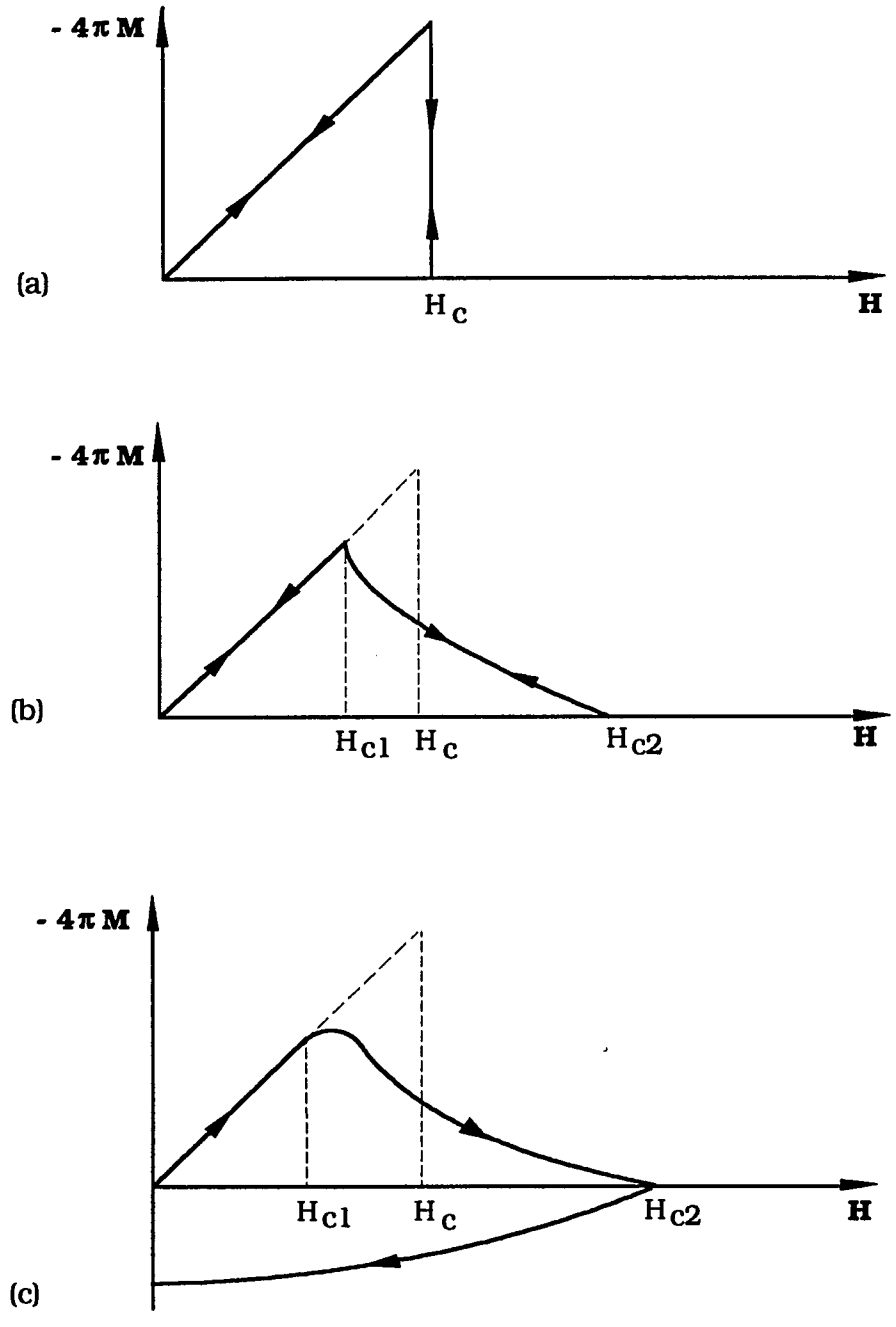

Fig. 1.1 Magnetization of superconductors: (a) type I; (b) ideal type II; (c) non-ideal type II (irreversible magnetization).

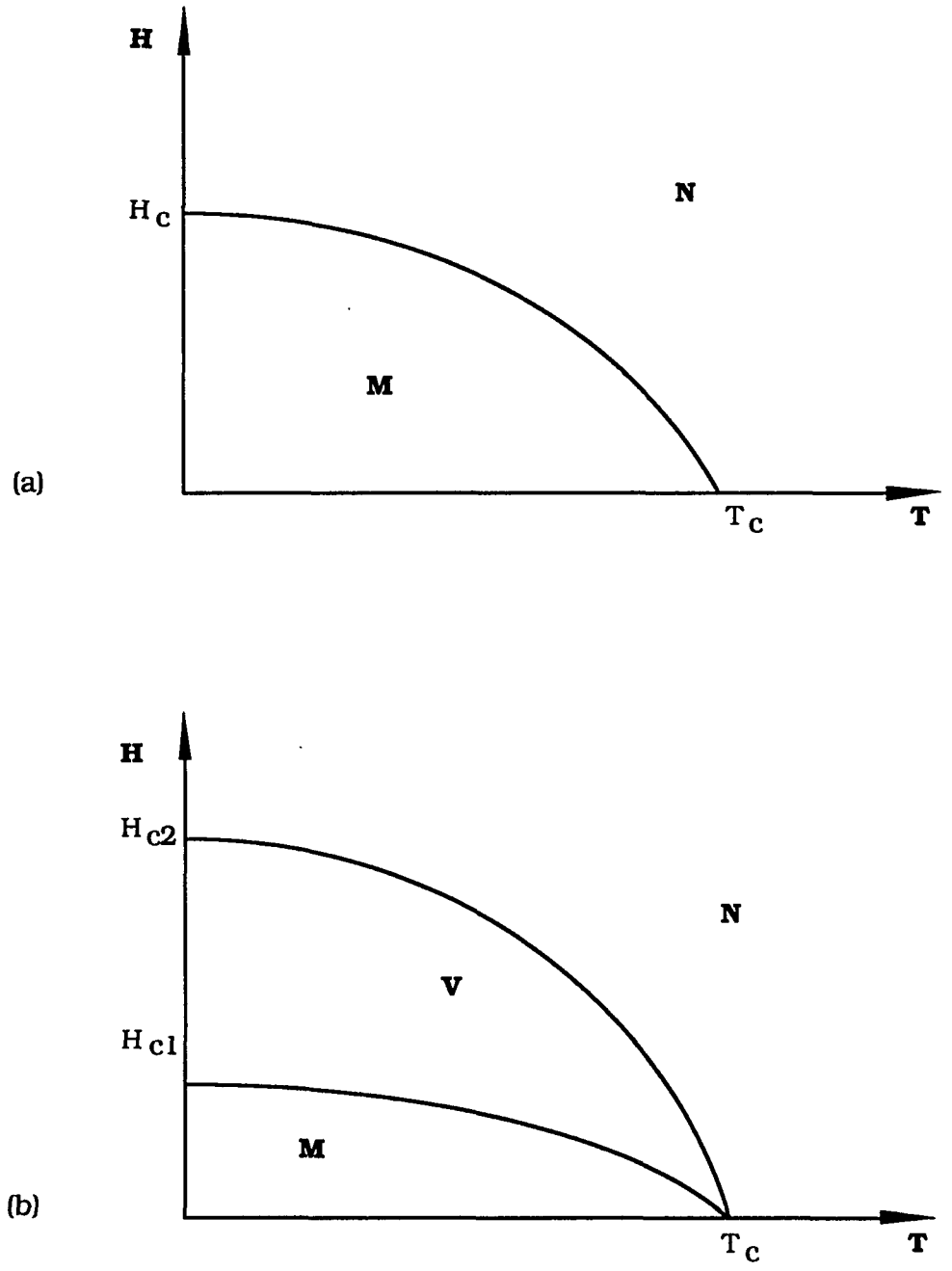

Fig. 1.2 The phase diagrams of superconductors: (a) type I; (b) type II (**M** for Meissner state, **V** vortex state, **N** for normal state).

$H \geq H_{c2}$, it is called normal state. There are a few type II superconductors in which this kind reversible magnetization behavior is observed, such as Nb and V in very pure form. These are called ideal type II superconductors. In reality most of the type II superconductors are non-ideal and show hysteresis in the magnetization. The impurities and inhomogeneities act as pinning centers preventing flux lines from coming in or going out the superconductors. The magnetization curve thus become irreversible as shown in Fig. 1.1c. The typical non-ideal type II superconductors are impure single element superconductors and alloys such as Nb-Sn, In-Pb, Bi-Pb, In-Hg, etc. The type II superconductors, ideal or non-ideal, have similar phase diagrams on which are a Meissner state, a vortex state and a normal state, as shown in Fig. 1.2b.

Although the basic mechanism causing the condensing of electrons into the superconducting ground state is the same for both types of superconductors, there are differences that rely on the competition between the two parameters, the magnetic penetration depth λ and the coherent length ξ. In 1957, Abrikosov first predicted the existence of type II superconductors [A. A. Abrikosov, 1957]. He demonstrated there were two different kinds of solutions to the Ginzburg-Landau (GL) equation depending on the GL parameter $\kappa = \lambda/\xi$. According to his theory, the superconductors with $\kappa < 1/\sqrt{2}$ would have first order phase transitions and were classified as type I; the superconductors with $\kappa > 1/\sqrt{2}$ would have second order phase transitions and were classified as type II. For the type II superconductors with $\kappa > 1/\sqrt{2}$, the surface energy between the normal and superconducting regions becomes negative. Then the appearance of normal regions in the superconducting state would reduce total free energy if the increase of the free energy due to the appearance of the normal region is outweighed by the decrease of

the free energy due to the negative surface energy. This is what happens in the vortex state when $H_{c1} < H < H_{c2}$. Normal regions appear in the superconducting state and magnetic flux penetrates the superconductor through these normal regions. In order to realize bigger surface area to achieve larger negative surface energy, a normal region would subdivide itself into smaller regions. But there is limit to the subdivision in that magnetic flux must be quantized. Therefore, in the vortex state where $H_{c1} \leq H \leq H_{c2}$, the magnetic flux penetrates the superconductor in a form of an array of vortices each carrying a single flux quanta $\Phi_0 = hc/2e = 2.0678 \times 10^{-7}$ G-cm^2, having a normal core of radius ξ and being circulated by supercurrents in a radius λ. A typical structure of an Abrikosov vortex is shown in Fig. 1.3. From this illustration, the relation of H_{c1} to Φ_0 and λ and that of H_{c2} to Φ_0 and ξ in GL theory are not hard to understand.

$$H_{c1} = \frac{\Phi_0}{4\pi\lambda^2} \ln \kappa \qquad (1.1)$$

$$H_{c2} = \frac{\Phi_0}{2\pi\xi^2} \qquad (1.2)$$

The vortices repel against each other organizing themselves into a periodic triangular lattice, called Abrikosov lattice. Because of the penetration of the vortices, the magnetization of the type II superconductor gradually declines to zero when H increases from H_{c1} to H_{c2}.

In summary, according to GL theory, the superconductors could be classified by the parameter $\kappa = \lambda/\xi$. If $\kappa > 1/\sqrt{2}$, the superconductor is type II; if $\kappa < 1/\sqrt{2}$, the superconductor is type I.

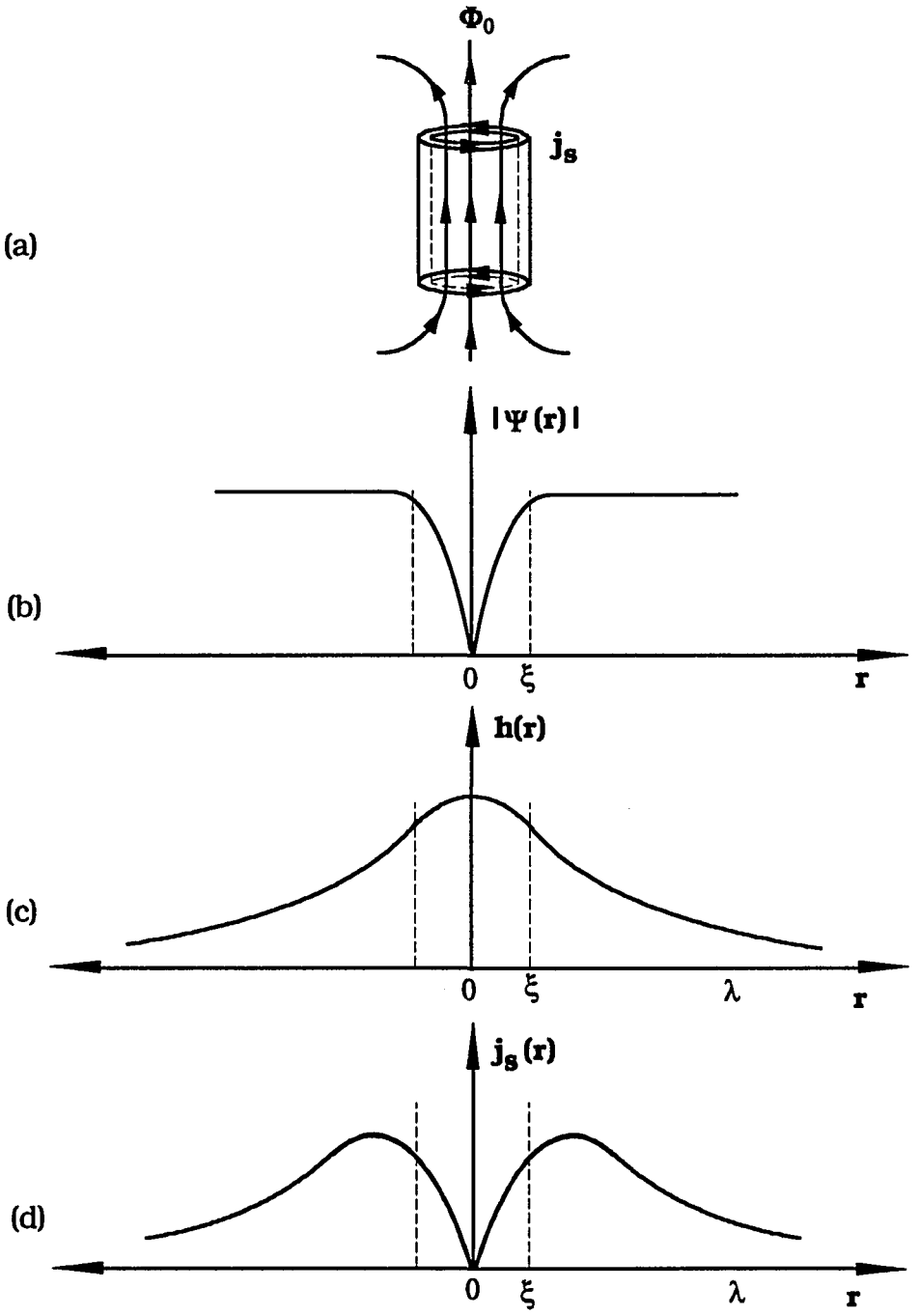

Fig. 1.3 Structure of an Abrikosov vortex: (a) the vortex; (b) the order parameter; (c) the local magnetic field distribution; (d) the supercurrent distribution.

1.2 High T_c Superconductors

High T_c superconductors are very different than conventional superconductors. They are part of a class of metal oxides which have traditionally been found to be insulators. In room temperature (300 K), $YBa_2Cu_3O_{7-\delta}$ has resistivities $\rho_a = 6.2 \times 10^{-4}$ Ω-cm, $\rho_b = 3.4 \times 10^{-4}$ Ω-cm and $\rho_c = 1.4 \times 10^{-2}$ Ω-cm [U. Welp et al., 1990; P. B. Allen, 1989]. These values are much larger than those of good conductors (~ 10^{-6} Ω-cm), much smaller than those of insulators (~ 10^{14} - 10^{22} Ω-cm), but close to those of semiconductors (~ 10^{-2} - 10^{9} Ω-cm). However, the linear decrease of ρ_a and ρ_b as temperature decrease indicates a metallic nature in the a-b plane, but rising of ρ_c as temperature decrease suggests a semiconductor behavior along the c axis.

Obviously, there is a strong anisotropy of the high T_c superconductors between the a-b plane and the c axis. As derived for the above values, the anisotropic ratio ρ_c/ρ_a ~ 20 and ρ_c/ρ_b ~ 40 for $YBa_2Cu_3O_{7-\delta}$. In a superconducting state, measurement of the upper critical field H_{c2} indicates that the electron effective mass along the c axis is 5 times larger than the effective mass in the a-b plane. This large anisotropy is related to the layered structure. As shown in Fig. 1.4, the structure of the $YBa_2Cu_3O_{7-\delta}$ contains the Cu-O planes and chains separated by Y and BaO layers. It is a perovskite-like structure that is made highly anisotropic by oxygen vacancies in the Y layers and in the CuO chains. The CuO layers are typical among the cupric oxide high T_c superconductors. Many research efforts have been devoted to study the mechanism of superconductivity in these high T_c materials. It is believed now these Cu-O planes contain charge carriers which form the Cooper pairs and produce the supercurrents.

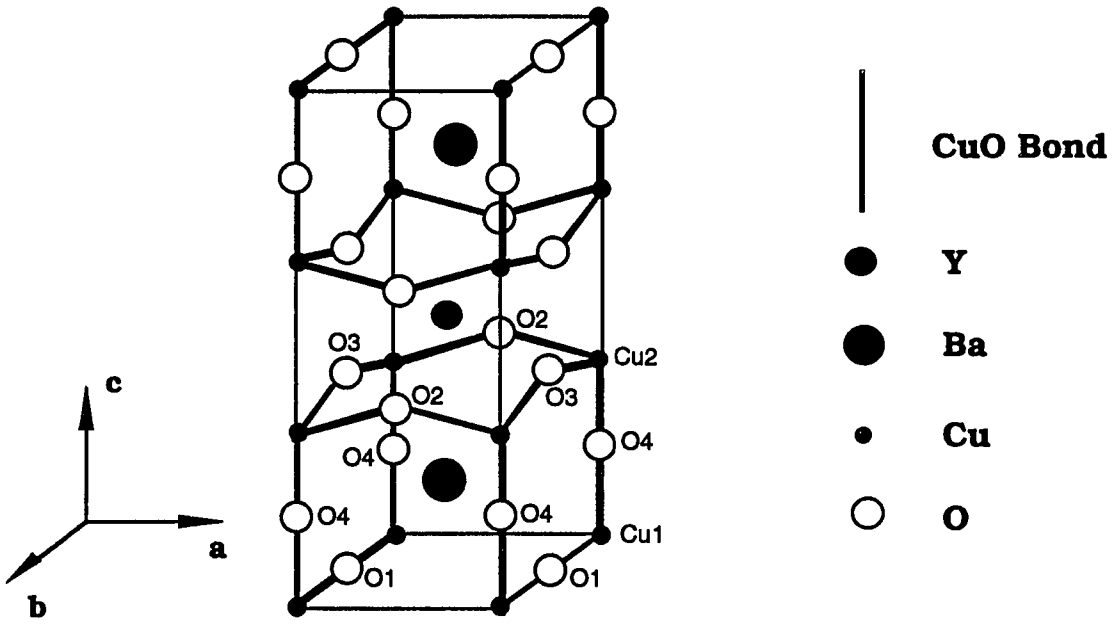

T_c = 93 K	$\xi_{ab}(0)$ = 1.5-1.7 nm
a = 0.38591 nm	$\xi_c(0)$ = 0.3-0.5 nm
b = 0.39195 nm	$\lambda_{ab}(0)$ = 140 nm
c = 1.18431 nm	$\lambda_c(0)$ > 700 nm

Fig. 1.4 The structure and some parameters of $YBa_2Cu_3O_{7-\delta}$

The high T_c superconductors are extreme type II superconductors. Because T_c is high, the coherent length $\xi = \hbar v_F / 2\pi k T_c$ is very short. On the other hand, the magnetic penetration depth λ is not affected by high T_c. Therefore $\kappa = \lambda/\xi$ is very high for high T_c superconductors ($\kappa(0) \sim 80$ for $YBa_2Cu_3O_{7-\delta}$). The magnetization of a high T_c superconductor is like that of a typical non-ideal type II conventional superconductor with a reversible magnetization region. As shown in Fig. 1.5a, the M vs. H curve is reversible in the high field region of the vortex state, i.e., for $H_{irr} < H < H_{c2}$. On the phase diagram, the $H_{irr}(T)$ defines a "Irreversibility Line", as shown in Fig. 1.5b. The irreversibility line is a subject of many researches.

The coherent length ξ of the high T_c superconductors is very short comparable with the lattice constants. For $YBa_2Cu_3O_{7-\delta}$, the $\xi_c \sim 0.3$ nm compared with $\xi \sim$ 10-1000 nm for a typical conventional superconductor. By Eq. 1.2, shorter coherent length means bigger H_{c2} which implies a potential advantage for applications. For $YBa_2Cu_3O_{7-\delta}$, an estimation using Eq. 1.2 results in $H_{c2}(0)$ = 440 T assuming ξ_{ab} = 1.5 nm. Shorter coherent length also means the superconductive properties are more sensitive to small scale structural and chemical imperfections. For example, a vortex in the mixed state has a radius of coherent length ξ. If it is comparable with lattice constants, point defects and dislocations become more effective to pin the vortex. The high energy proton radiation induced defects are mostly point defects, as will be discussed in the chapter 4 of this dissertation. In this experiment, the effective enhancement of pinning at low proton fluence is related to the fact that the coherent length of $YBa_2Cu_3O_{7-\delta}$ is short.

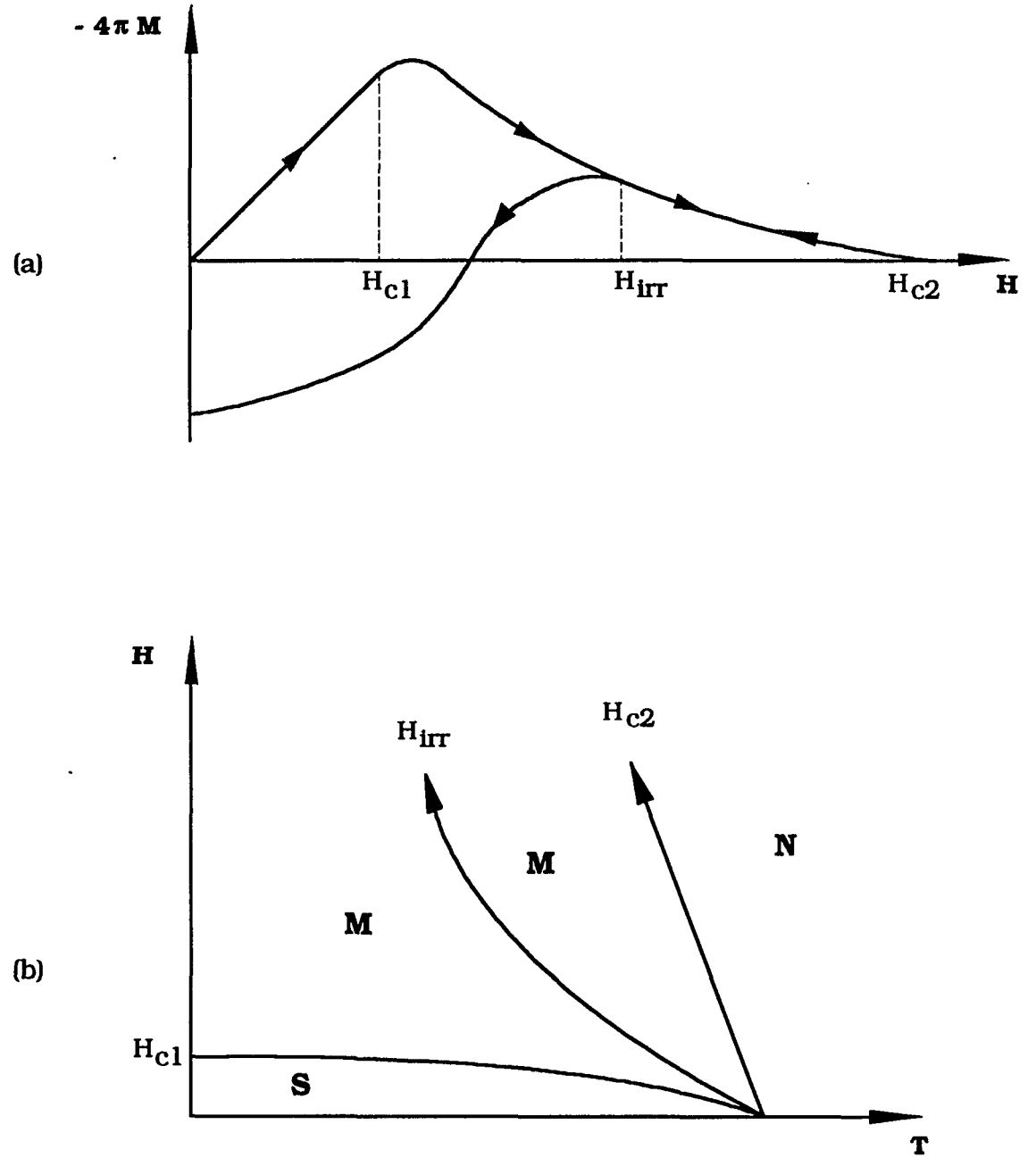

Fig. 1.5 (a), The magnetization behavior of high T_c superconductor, and (b) the phase diagram of high T_c superconductor.

In summary, the high T_C superconductors have very high transition temperature T_C, very strong spatial anisotropy and short coherent length. They are extreme type II superconductors with a reversible region in the high field region of the mixed state.

CHAPTER 2. THEORETICAL REVIEW

2.1 Critical Current Density J_c

The critical current density of a superconductor is defined as the highest current density it can carry without resistance. When a supercurrent passes through a superconductor, it generates a magnetic field. The magnetic field suppresses superconductivity. Therefore, the critical current density is determined by the critical field H_c it generates at the surface when passing through the superconductor. This is the so called Silsbee rule and is observed to apply for type I superconductors. For example, consider a type I superconductor wire of radius r. The magnetic field generated by the current I at the surface is H=2I/cr from Ampere's law, where c is the speed of light. As shown in Fig. 2.1, if the penetration depth of the field is λ and the supercurrents are assumed uniformly confined within the skin depth λ, then $I = 2\pi r\lambda J$, where J is the supercurrent density. If H increases to H_c as the result of current increase, the surface of the wire becomes normal and the corresponding current density is the critical current density J_c. Thus

$$J_c = \frac{cH_c}{4\pi\lambda} \qquad (2.1)$$

where $c = 3 \times 10^{10}$ cm/s, H_c is in 'oersteds', λ is in 'centimeters', and J_c thus calculated is in 'statamperes/cm^2', i.e., they are in CGS units. To convert J_c from 'statamperes/cm^2' to 'amperes/cm^2', divide the J_c by 3×10^9. Although this is a

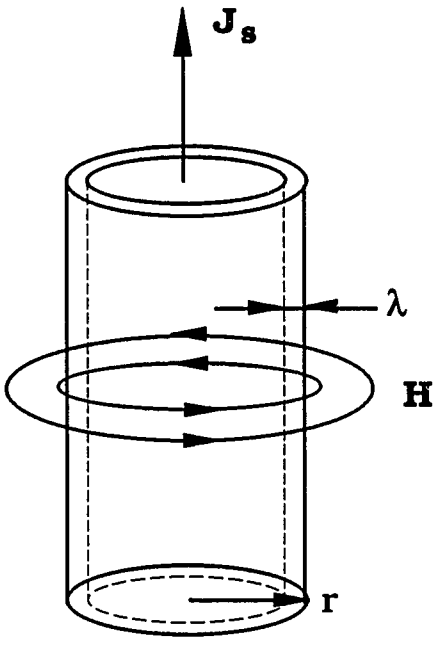

$$2\pi r\, H = \frac{4\pi}{c} J\, 2\pi\, r\lambda \longrightarrow J_c = \frac{cH_c}{4\pi\lambda}$$

Fig. 2.1 The critical current density for a superconducting wire given by the Silsbee rule.

result of very rough estimation, it is very similar to that given by the GL theory.

The GL theory explains the phenomena of superconductivity in a simple form. The GL theory is based on the fact that the normal to superconducting transition is a second order phase transition for type I superconductors in absence of magnetic field and for type II superconductors in either absence or presence of magnetic field. In the second order phase transition, a new parameter appears,

called order parameter. For example in the paramagnetic to ferromagnetic phase transition, the order parameter is the magnetic moment $\vec{M}$. In normal to superconducting phase transition, the order parameter is a complex variable ψ which has the meaning of electron wave function of the superconducting state. The free energy density of the system near the phase transition point T_C can be expand in terms of ψ and its derivatives because ψ is small near T_C. That is

$$f = f_{no} + \alpha|\psi|^2 + \beta|\psi|^4 + \frac{1}{2m^*}\left|\left(\frac{\hbar}{i}\vec{\nabla} - \frac{e^*\vec{A}}{c}\right)\psi\right|^2 + \frac{h^2}{8\pi} \qquad (2.2)$$

By minimizing this free energy, the GL equations are derived.

$$\alpha\psi + \beta|\psi|^2\psi + \frac{1}{2m^*}\left(\frac{\hbar}{i}\vec{\nabla} - \frac{e^*}{c}\vec{A}\right)^2\psi = 0 \qquad (2.3)$$

and
$$\vec{J} = \frac{c}{4\pi}\vec{\nabla}\times\vec{h} = \frac{e^*\hbar}{2m^*i}\left(\psi^*\vec{\nabla}\psi - \psi\vec{\nabla}\psi^*\right) - \frac{e^{*2}}{m^*c}|\psi|^2\vec{A} \qquad (2.4)$$

or
$$\vec{J} = \frac{e^*}{m^*}|\psi|^2\left(\hbar\vec{\nabla}\varphi - \frac{e^*}{c}\vec{A}\right), \quad \text{if } \psi(\vec{r}) = |\psi(\vec{r})|e^{i\varphi(\vec{r})} \qquad (2.5)$$

If a uniform current density is assumed for a wire, the critical current density is found when the kinetic energy of the supercurrent equals 2/3 of the condensation energy of the superconducting state [J. Bardeen, 1962]. That is

when
$$\frac{1}{2}n_s^*m^*v_s^2 = \frac{2}{3}\frac{H_c^2}{8\pi} \qquad (2.6)$$

$$J_c = \frac{cH_c(t)}{3\sqrt{6}\,\pi\lambda(t)} \propto (1-t)^{3/2} \qquad (2.7)$$

where v_S is the velocity of superconducting charge carrier and t is the reduced temperature T/T_C. This result is essentially the same as Eq. 2.1 derived from Silsbee rule except a factor $4/(3\sqrt{6})=0.54$.

In BCS theory, the Cooper pairs are broken when they move collectively with a speed larger than v_s given by

$$v_s = \frac{\Delta}{\hbar k_F} \tag{2.8}$$

[M. Tinkham, 1975]. By the relation of Δ to the condensation energy of superconducting state,

$$\frac{H_c^2}{8\pi} = \frac{1}{2}\frac{3n}{2E_F}\Delta^2 \tag{2.9}$$

the Eq 2.8 could be changed into Eq 2.6 except the factor of 2. That means the condition of Eq. 2.6 is really that for breaking the Cooper pairs. Therefore the critical current density J_C by Eq 2.7 is a depairing critical current density microscopically.

However, Eq. 2.7 for the depairing critical current density is not what is measured experimentally for type II superconductors. Rather, in type II superconductors, flux motion causes resistivity before the transition to the normal state. For YBa_2CuO_{7-d}, the typical depairing critical current density by Eq. 2.7 gives $J_C = 6 \times 10^8$ A/cm^2 at 4.2 K for H_C = 1 T and λ = 140 nm. This value is much higher than the experimental result which is about 10^5-10^6 A/cm^2. Flux motion arises because the vortices are pushed by supercurrents in the vortex state, as shown in Fig. 2.2. The force per unit length on a single vortex is expressed as

$$\vec{f} = \vec{J}_s \times \frac{\vec{\Phi}_0}{c} \tag{2.10}$$

If the vortices are moved or depinned as the result of the push, an electric field $\vec{E}$ is generated along the direction of the supercurrents by Faraday's law. Therefore, a voltage drop appears and power is dissipated as $\vec{J} \bullet \vec{E} > 0$. The depinning critical

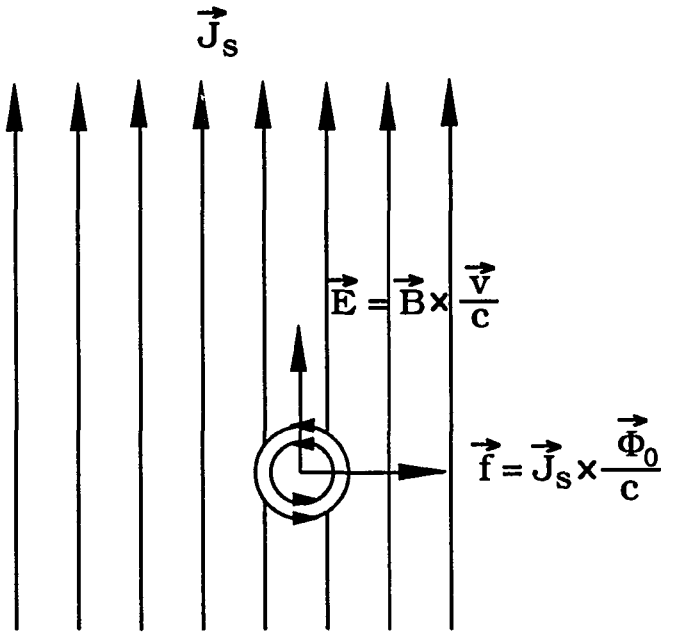

Fig. 2.2 A vortex being pushed by a supercurrent and an electric field being generated by the vortex motion.

critical current density is the quantity measured experimentally and it is very sensitive to the microstructure of the sample. Vortices are quite often pinned by microscopic defects such as voids, dislocations, impurities and so on. Thus an effective way to enhance critical current density is to create defects artificially in the sample. Since the discovery of high T_c superconductors, many researches have been directed to enhancement of the critical current density by generating defects such proton irradiation, neutron irradiation, addition of impurities, producing secondary phases and so on.

2.2 Vortex Pinning

Vortex pinning is caused by local fluctuation in the properties of a material which results in the free energy of the sample depending in detail on the positions of the vortices. The inhomogenieties like vacancies, interstitials, dislocations, twin boundaries, secondary phases and surfaces of superconductor all contribute to the fluctuation of the local free energy density. The total free energy of the superconductor will change as the vortices move on or off these positions.

2.2.1 Pinning by a normal region

As shown in Fig 1.3, the order parameter of the superconductor is suppressed to zero in a vortex core. That increases the free energy density at vortex core by $H_c^2/8\pi$. If the superconductor is uniform without any defects, the vortex can move around in it without increasing the total free energy of the superconductor. However, if there is a normal region of volume V in the superconductor, the situation is different. As shown in Fig. 2.3a, if the vortex sits on the normal region, the total volume of normal materials in the superconductor is only that in the vortex core. Now, if the vortex moves to an another place which is perfectly superconducting without any normal regions, there is an additional amount of normal material of volume V appears in the superconductor. The vortex motion thus increases the total free energy of the superconductor by $(H_c^2/8\pi)V$ [Fig. 2.3b]. Therefore, there is a force pushing the vortex back to the position of the normal region and it appears that the vortex is pinned by the normal region. The pinning force p_m can be estimated using the radius of the vortex, i.e., the coherent length ξ

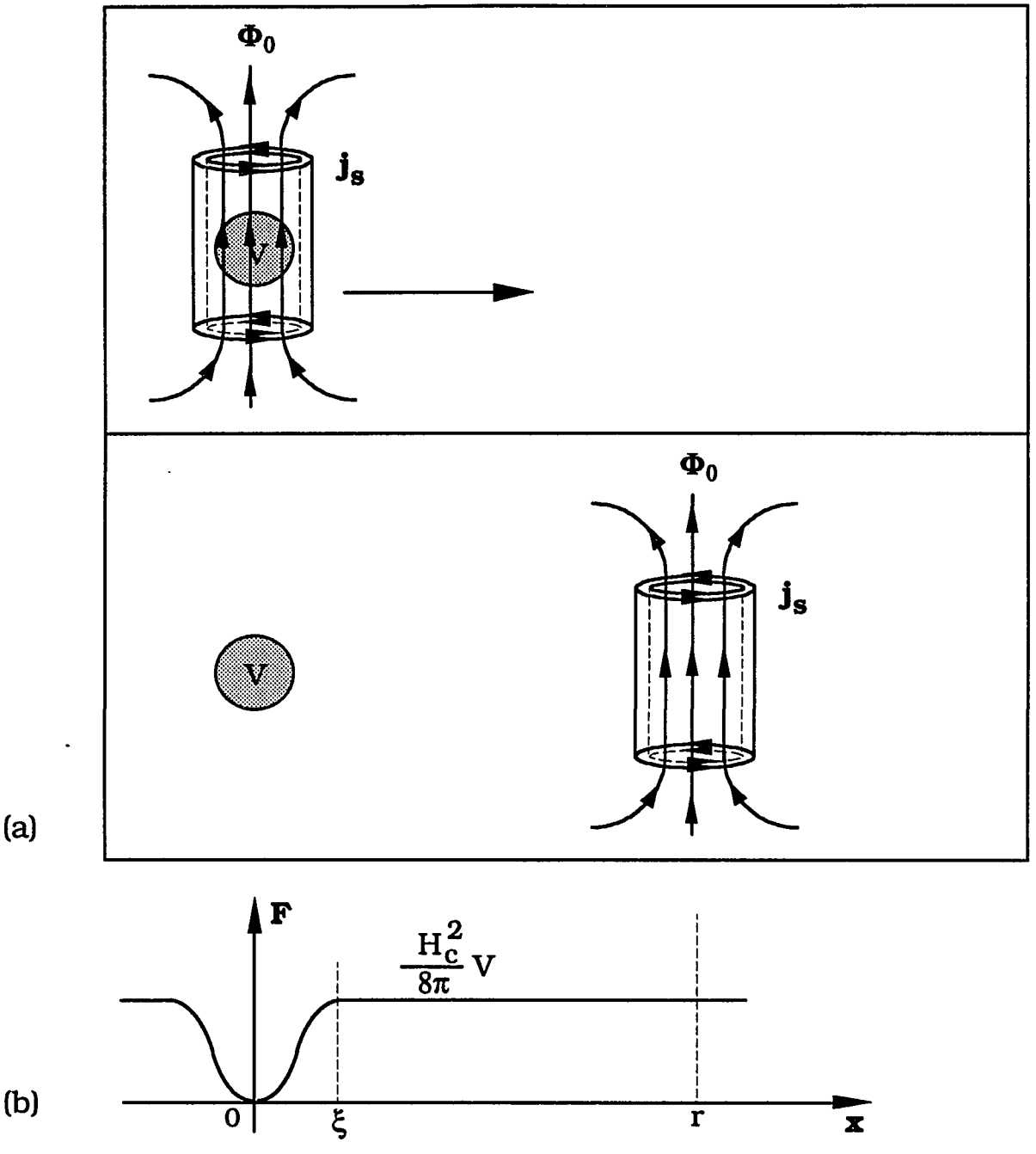

Fig. 2.3 Vortex pinning by a normal region: (a) motion of a vortex away from the normal region; (b) the increase of total free energy as result of the motion.

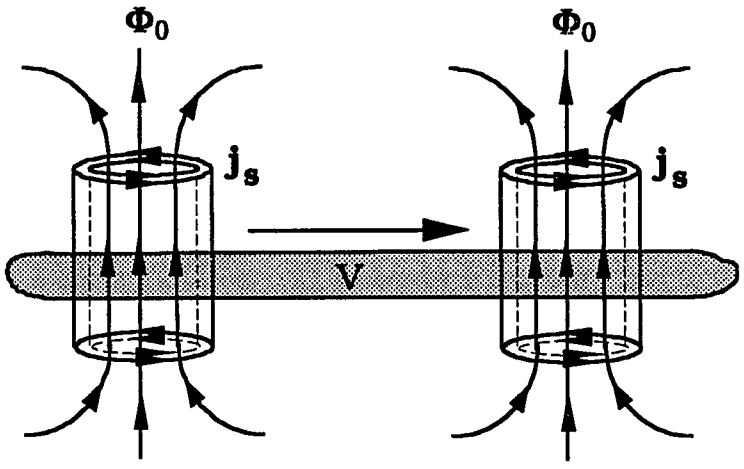

Fig. 2.4 A vortex can move when pinned by a large normal region

$$p_m = \frac{H_c^2}{8\pi\xi} V = \frac{H_{c2}^{5/2}}{8\sqrt{2\pi\Phi_0}\,\kappa^2} V \qquad (2.11)$$

where V is the volume of the normal region and $\kappa = \lambda/\xi$ is the GL parameter. Combined with Eq. 2.10, the depinning critical current density is

$$J_c = \frac{c p_m}{\Phi_0 l} = \frac{c H_c^2}{8\pi\xi\Phi_0}\frac{V}{l} = \frac{c H_{c2}^{5/2}}{8\sqrt{2\pi}\,\kappa^2\Phi_0^{3/2}}\frac{V}{l} \qquad (2.12)$$

where l is the length of the vortex. Eq 2.12 can be used to estimate the depinning critical current density J_C. Assuming the normal regions as pinning centers are voids and interstitials which have dimensions about 0.1 nm and they are about 100 nm apart on average, and $\xi \approx 1$ nm, $H_C = 1$ T, the depinning J_C thus estimated from Eq 2.12 is about 10^6 A/cm^2, close to experimental values.

From the above discussion, it is very easy to understand that the most effective pinning happens when the dimension of the normal region is comparable with the radius of the vortex ξ. If the normal region is too large, the vortex is not tightly pinned and has some room to move around, as shown in Fig. 2.4.

2.2.2 The GL theory for pinning

The Eq. 2.2 for GL free energy density provides a good starting point to study the pinning phenomenon. The total GL free energy of a superconductor F(ψ ,h) is simply

$$F(\psi, h) = \int (f_s - f_n) dV \qquad (2.13)$$

where f is the GL free energy density, ψ is the order parameter and h is the local magnetic field. If the ψ_0 and h_0 are the equilibrium value of ψ and h in the unperturbed system then the derivatives $(\partial F / \partial \psi)_{\psi=\psi_0}$ and $(\partial F / \partial h)_{h=h_0}$ are both zero. When there is a small perturbation in the superconductor, the total GL free energy is changed to

$$\begin{aligned}(F + \delta F)(\psi, h) &= F(\psi_0 + \delta\psi, h_0 + \delta h) + \delta F(\psi_0, h_0) \\ &= F(\psi_0, h_0) + \frac{\partial F}{\partial \psi}_{\psi=\psi_0} \delta\psi + \frac{\partial F}{\partial h}_{h=h_0} \delta h + \delta F(\psi_0, h_0) \\ &= F(\psi_0, h_0) + \delta F(\psi_0, h_0)\end{aligned}$$

Therefore the change of total free energy due to the perturbation is

$$dF = \delta F(\psi_0, h_0) = \int (\delta\alpha |\psi_0|^2 + \frac{\delta\beta}{2} |\psi_0|^4) dV \qquad (2.14)$$

If ψ_0 is replaced with relative order parameter $\phi = \psi_0 / \psi_\infty$, where $|\psi_\infty|^2 = (mc / 4\pi e\hbar\kappa^2) H_{c2}$ is the order parameter far away from the vortex, and the relations $\alpha = -(e\hbar / 2mc) H_{c2}$, $\beta = 2\pi (e\hbar / mc)^2 \kappa^2$ and $H_{c2} = \sqrt{2}\,\kappa H_c$ are used, the Eq. 2.14 is changed to

$$dF = 2 \int \frac{H_c^2}{8\pi} (-\frac{\delta H_{c2}}{H_{c2}} |\phi|^2 + \frac{\delta\kappa^2}{2\kappa^2} |\phi|^4)\, dV \qquad (2.15)$$

At high field the $|\phi|<<1$, therefore $|\phi|^2>>|\phi|^4$, the dominant contribution to dF is from δH_{c2}. While at low field $|\phi|^2 \approx |\phi|^4$, the Eq. 2.15 becomes

$$dF = -2\int \frac{H_c^2}{8\pi}\frac{H_{c2}}{\kappa}\delta(\frac{H_{c2}}{\kappa})|\phi|^2\, dV = -\int \frac{\delta H_c^4}{4\pi}|\phi|^2\, dV \qquad (2.16)$$

That means the dominant contribution to dF is from δH_c when field is low.

Consider again the pinning by a small normal sphere of radius $r<<\xi$. If the sphere is at center of a vortex core, $|\phi| \approx 0$, and dF=0. However, if the vortex moves away from the sphere, $|\phi| \approx 1$, and $dF=-(H_c^2/8\pi)V$ for $\delta H_{c2}=H_{c2}$ and $\delta\kappa^2=\kappa^2$. That directly leads to Eq. 2.11 for pinning force of a small normal region. In the high field region, many vortices penetrate the superconductor instead of an isolated single vortex. They form a periodical hexagonal vortex array. The order parameter $|\phi|^2$ varies sinusoidally from minimum 0 to maximum $(3/2)(1-b) << 1$, where $b=B/B_{c2}$. From Eq. 2.15, the total free energy change

$$dF \approx -2\int \frac{H_c^2}{8\pi}\frac{\delta H_{c2}}{H_{c2}}|\phi|^2\, dV \approx -\frac{H_c^2}{4\pi}\frac{\delta H_{c2}}{H_{c2}}V|\phi|^2 \qquad (2.17)$$

Assuming a sinusoidal function $\sin^2(\pi x/a_0)$ for $|\phi|^2$, the maximum derivative of $|\phi|^2$ is $(3/2)(1-b)(\pi/a_0)$, where a_0 is the vortex spacing, the maximum pinning force p_m is

$$p_m = \frac{3H_c^2}{8a_0}V(1-b)\frac{\delta H_{c2}}{H_{c2}} \qquad (2.18)$$

That means even if the defects are superconducting they could pin vortices if they have different H_{c2}. One of the interesting features in the magnetization behavior of high T_c superconductors is the large fish tail on M vs. H curves. That is pinning increases with the fields before reaching a maximum. One of the theories is that there are regions of different H_{c2} in the superconductor such as oxygen deficiency

regions [M. Daeumling et at, 1990]. As the field increases to the H_{c2} of these defects, they become normal and increase the pinning as indicated by Eq. 2.18. However, this is a very controversial issue with many theories claiming self correctness.

2.2.3 Pinning by surfaces of superconductors

When a vortex moves close to a surface from inside of a superconductor, the screening supercurrents try to push it back, but the image of the vortex through the boundary tries to pull it over to the surface. The competition of these two forces results in vortex being held or pinned near the surface.

In the high field region, screening supercurrent density can be derived from the equilibrium or reversible magnetization M_e of the superconductor. As shown in Fig. 2.5a, from the London equation

$$\nabla^2\bar{B} - \frac{1}{\lambda^2}\bar{B} = 0 \qquad (2.19)$$

and the boundary conditions $B_{x=0} = H_0$ and $B_{x=\infty} = H_0 + 4\pi M_e$, the B field is

$$B = -4\pi M_e e^{-\frac{x}{\lambda}} + H_0 + 4\pi M_e \qquad (2.20)$$

Therefore the screening supercurrent density is

$$J_s = \frac{c}{4\pi}\frac{\partial B}{\partial x} = \frac{cM_e}{\lambda}e^{-\frac{x}{\lambda}} \qquad (2.21)$$

Finally, the force by the supercurrent pushing the vortex back to the inside of superconductor is

$$f_s = J_s \times \frac{\Phi_0}{c} = \frac{\Phi_0 M_e}{\lambda}e^{-\frac{x}{\lambda}} \qquad (2.22)$$

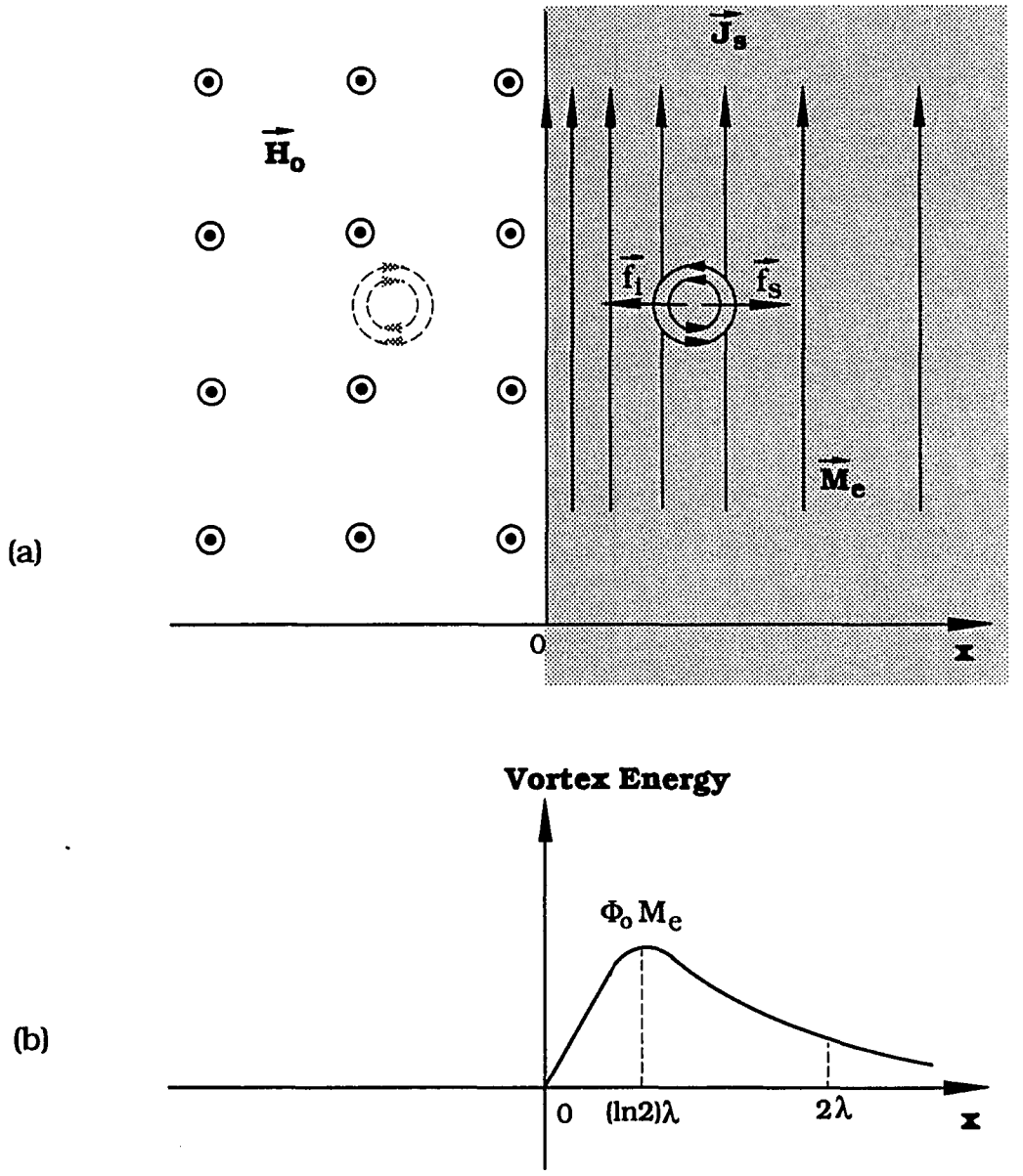

Fig. 2.5 Pinning of a vortex at surface of a superconductor: (a) the interaction between the vortex and the supercurrents, and that between the vortex and its image; (b) the energy of the vortex as it moving from the surface to the inside of the superconductor.

Because the local magnetic field of a vortex varies exponentially as $e^{-x/\lambda}$ when $x >> \lambda$, the force by the image of the vortex through the surface of superconductor can be assumed as

$$f_i = -Ce^{-2x/\lambda} \tag{2.23}$$

where C is a constant. In thermal equilibrium, the energy of the vortex at the boundary of the superconductor and that infinitely deep inside of the superconductor should be the same, otherwise the magnetic flux either all in or all out the superconductor, as shown in Fig. 2.5b. That means the total work done by the pushing from supercurrent and the pulling from the image must be zero when the vortex moves across the boundary to infinitely depth inside of the superconductor. That gives $C = 2(\Phi_0 M_e) / \lambda$. Therefore, the total force per unit length on the vortex when it is near the surface of the superconductor is

$$p = \frac{\Phi_0 M_e}{\lambda}(e^{-\frac{x}{\lambda}} - 2e^{-\frac{2x}{\lambda}}) \tag{2.24}$$

The maximum of that force happens at the surface x=0.

$$p_m = -\frac{\Phi_0 M_e}{\lambda} \tag{2.25}$$

Because the surface pinning results from the images of vortices, a rough surface could distort the images and reduce the pinning force. In the magnetic hysteresis measurement, for a superconductor with only surface pinning, the decreasing field magnetization is very close to zero and the hysteresis is of the same order as the reversible magnetization. Pinning by the surface of the superconductor is significant for field just beyond H_{c1} when many vortices nucleate at the surfaces waiting to be pushed into the sample.

2.2.4 Pinning by elastic stress field

Dislocations create elastic stress field and pin vortices through the elastic energy. There are two major mechanisms that contribute to the vortex pinning by the stress fields. First, the volume of the normal core in the vortex decreases a very small amount with respect to the surrounding superconducting region. The resulting strain field interacts with the stress field of a defect such as a dislocation. The interaction energy is linear in the defect stress . This is the so called the " Volume Effect " or the 'first order effect'. Second, the elastic constant of the normal core increases a very small amount with respect to the surrounding superconducting region. That modifies the elastic energy of the stress field of the defect. The interaction is quadratic in the defect stress. This is so called the 'second order effect' [A. M. Campbell et al., 1972]

2.2.5 Summary

There are many mechanisms for vortex pinning. For a superconductor, the particular pinning mechanism depends on the microscopic defect structure. The quantity that could be measured experimentally is the critical current density J_C . From Eq. 2.10, the pinning force density P_V could be derived as $P_v = (J_c B)/c$. The previous discussion about pinning mechanism indicates in high field region the pinning force density could assumed in the form

$$P_v = S\frac{B_{c2}{}^n}{\kappa^p} b^m (1-b)^l \qquad (2.26)$$

where S is a constant, κ is GL parameter, $b=B/B_{C2}$ and n, m, l, p are constants [A. M. Campbell et al., 1972]. A great deal of qualitative information could be drive

from P_V vs. b graph. On the graph, P_V has a maximum. For many materials containing second phases, or plane boundaries, the maximum occurs at about b=1/3, for those containing dislocations, the maximum varies between b = 0.25 and b = 0.85.

2.3 Critical State Model

The magnetization of a non-ideal type II superconductors shows hysteresis as result of microscopic defects. The critical state model was proposed to explain this phenomenon [C. P. Bean, 1962]. The essential idea is that the magnetic flux in form of vortices is pushed in by the screening supercurrents until defects provide balancing force limiting this motion. The vortices stay in their places because of the pinning until the field increases and more vortices are pushed in. Then they move on to the other positions. As more and more vortices come in, all the available vortex positions are full, then the vortices stop the penetration and the vortex distribution remains constant to further increase of the field. This is so called critical state and the corresponding magnetic field is called the full penetration field H^*. At this full penetration field H^*, the flux front reaches the center of the sample. Apparently, in the critical state, screening supercurrent is the maximum current the superconductor could carry, otherwise the supercurrent could increase to push in more vortices. This maximum screening supercurrent density in the critical state is called the Bean critical state current density of the superconductor. The Maxwell equation thus becomes

$$\nabla \times \vec{B} = \frac{4\pi}{c} \vec{J}_c \qquad (2.27)$$

From this equation, the magnetic hysteresis could be determined and the critical current density J_C could be related to the magnetization M. There are many solutions to Eq. 2.27 which leads to various versions of critical state model depending on how the J_C is chosen as a function of local magnetic field $\vec{B}$ and the boundary conditions.

2.3.1 Bean model

This most simple critical state model is the Bean model in which the sample is assumed as a slab of a of thickness d and the critical current density J_C is assumed independent of local magnetic field B

$$J_c(T, B(x)) = J_c(T) \tag{2.28}$$

As shown in Fig. 2.6, with boundary conditions $B_{x=0,d} = H$ and the flux pinning assumption as previously discussed, the local magnetic field B is determined. For increasing field, the B field by Eq. 2.27 is

$$B = H - \frac{4\pi}{c} J_c x; \qquad 0 \le x \le \frac{d}{2} \tag{2.29}$$

$$B = H + \frac{4\pi}{c} J_c (x - d); \qquad \frac{d}{2} \le x \le d \tag{2.30}$$

The average magnetic induction <B> is

$$< B >= \frac{2}{d} \int_0^{d/2} B(x) dx \tag{2.31}$$

By - 4πM = H - <B> , the increasing field magnetization $M^{\uparrow}$ is

$$-4\pi M^{\uparrow} = H - \frac{H^2}{2H^*} \qquad H \le H^* \tag{2.32}$$

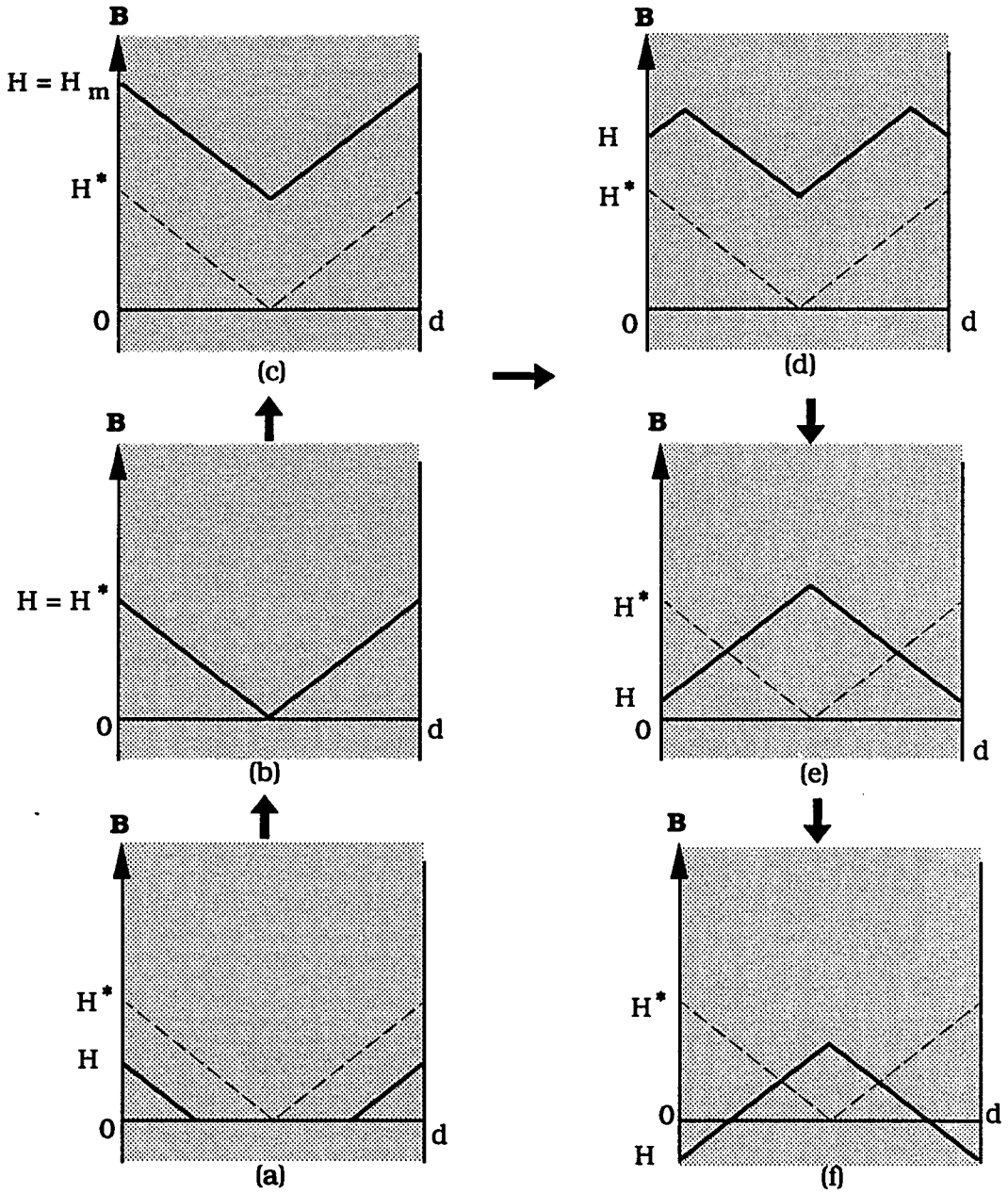

Fig. 2.6 The local magnetic field distributions during the magnetization of the superconductor slab of thickness d in critical state model: (a) H begins to increase; (b) $H = H^*$; (c) $H = H_m$; (d) H begins to decrease; (e) and (f) further decreasing

$$-4\pi M^{\uparrow} = \frac{H^*}{2} \qquad H^* \le H \le H_m \tag{2.33}$$

By the same method, the decreasing field magnetization $M^{\downarrow}$could be found

$$-4\pi M^{\downarrow} = H - H_m + \frac{H^*}{2} - \frac{(H - H_m)^2}{4H^*} \qquad H_m - 2H^* \le H \le H_m \tag{2.34}$$

$$-4\pi M^{\downarrow} = -\frac{H^*}{2} \qquad -H_m \le H \le H_m - 2H^* \tag{2.35}$$

where the $H^* = 2\pi J_c\, d / c$ is the full penetration field. As shown in Fig. 2.7, these equations describe a magnetic hysteresis loop. From Eq. 2.31 and Eq. 2.33, after the magnetic field fully penetrating the slab, the width of the magnetic hysteresis loop is simply proportional to the critical current density.

$$J_c = \frac{2c\,\Delta M}{d} \tag{2.36}$$

This relation implies that the critical current density J_C can be measured inductively through measuring the magnetic hysteresis loop and large hysteresis loop corresponding the high critical current density J_C. Inductive measurement of J_C is widely used for both conventional and high T_C superconductors. In most experiments, the ΔM is not constant of the field contrary to the Bean model. That implies the J_C is a function of the field. This problem can be avoided in two ways. First, use a field dependent J_C such as

$$J_c(T, B(x)) = J_c(T)\, e^{-|B(x)|/H_0} \tag{2.37}$$

where H_0 is a material parameter which can be determined experimentally. Eq. 2.27, the critical state equation, is then solved to get the magnetization M as the function of the applied field H. By fitting experimental data to this function, the field and temperature dependence of J_C is obtained. For Nb-25% Zr wire, this inductive J_C agreed within 6% of the experimental transport critical current density

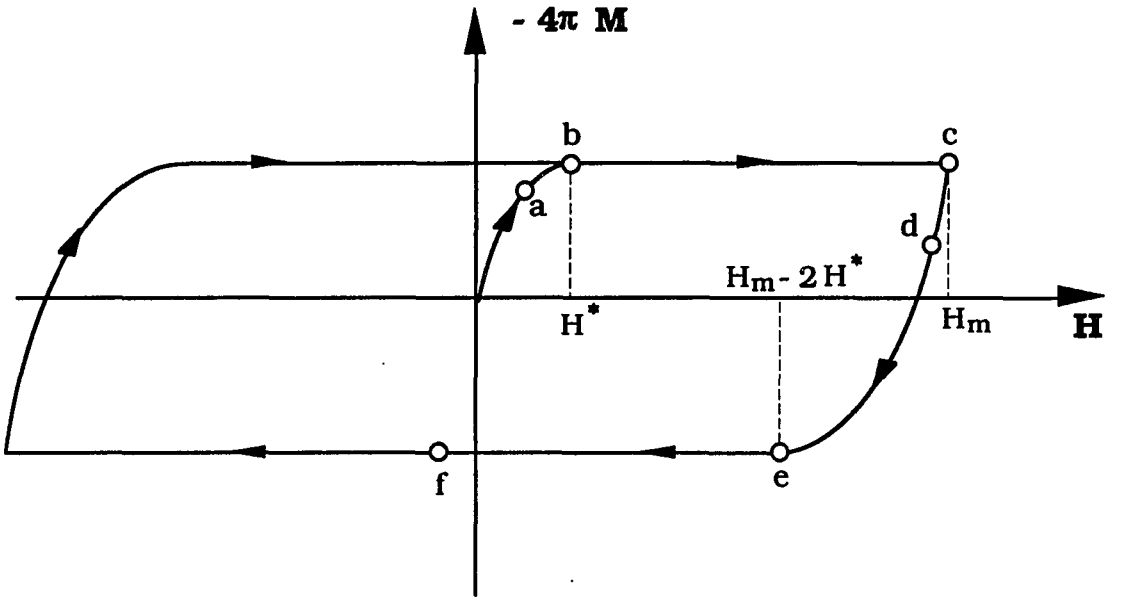

Fig. 2.7 The magnetic hysteresis loop by the Bean model. The a, b, c, d, e and f here are corresponding the those magnetization states shown in Fig. 2.6.

J_C up to 4 T field [W. A. Feitz et al., 1964]. Recently, this exponential J_C relation to applied field was applied to high T_C superconductors and produced quite reasonable agreement between the inductive critical current density and the experimental transport critical current density [D. X. Chen et al., 1989]. Second, apply the Bean model directly to the magnetic hysteresis loop to get J_C as a function of the field. In Pb-Bi eutectic specimen, the critical current density given by Eq. 2.35 has less than 4% error compared with the result of transport measurement at full penetration field $H^* = (1/3)H_{C2}$. Then the error dropped rapidly to 0.5% in high field region from $(1/2)H_{C2}$ to H_{C2} = 1.3 T [R. I. Coote et al., 1972]. If the ΔM is used instead of M as in Eq. 2.35 and the flux complete

penetrates the sample, the result of Eq. 2.35 agrees well with that of the transport measurement.

The good agreement between J_c from Eq. 2.35 and J_c from transport measurement suggests that J_c given by Eq. 2.35 is actually the depinning critical current density of the superconductor and this depinning critical current density can be enhanced by increasing the number of pinning sites or defects in the sample through various methods such as proton irradiation.

2.3.2 Anisotropic critical state model

When the superconductor has a different shape instead of a infinite slab and the critical current density has strong anisotropy, the Bean model has to be modified. For a $YBa_2Cu_3O_{7-d}$ single crystal, the sample shape is quite often a small rectangle and the critical current density flowing along the c axis J_c^c is much smaller than that flowing in the a-b plane J_c^{ab}. For a rectangle with anisotropy of J_c along the two sides, an anisotropic critical state model has to be used [E. M. Gyorgy et at, 1989].

As shown in Fig. 2.8, for a rectangle, the full penetration field is determined by the competition of the factors J_c^a/a and J_c^b/b along the two sides. If J_c is assumed independent local magnetic field B as in Eq. 2.28, the B field could be obtained by solving Eq. 2.27.

If $J_c^a/a < J_c^b/b$, the full penetration field $H^* = (2\pi\, a/c)\, J_c^a$ and the width of magnetic hysteresis loop is

$$\Delta M = \frac{J_c^a a}{2c}\left(1 - \frac{J_c^a b}{3\, J_c^b a}\right) \qquad (2.38)$$

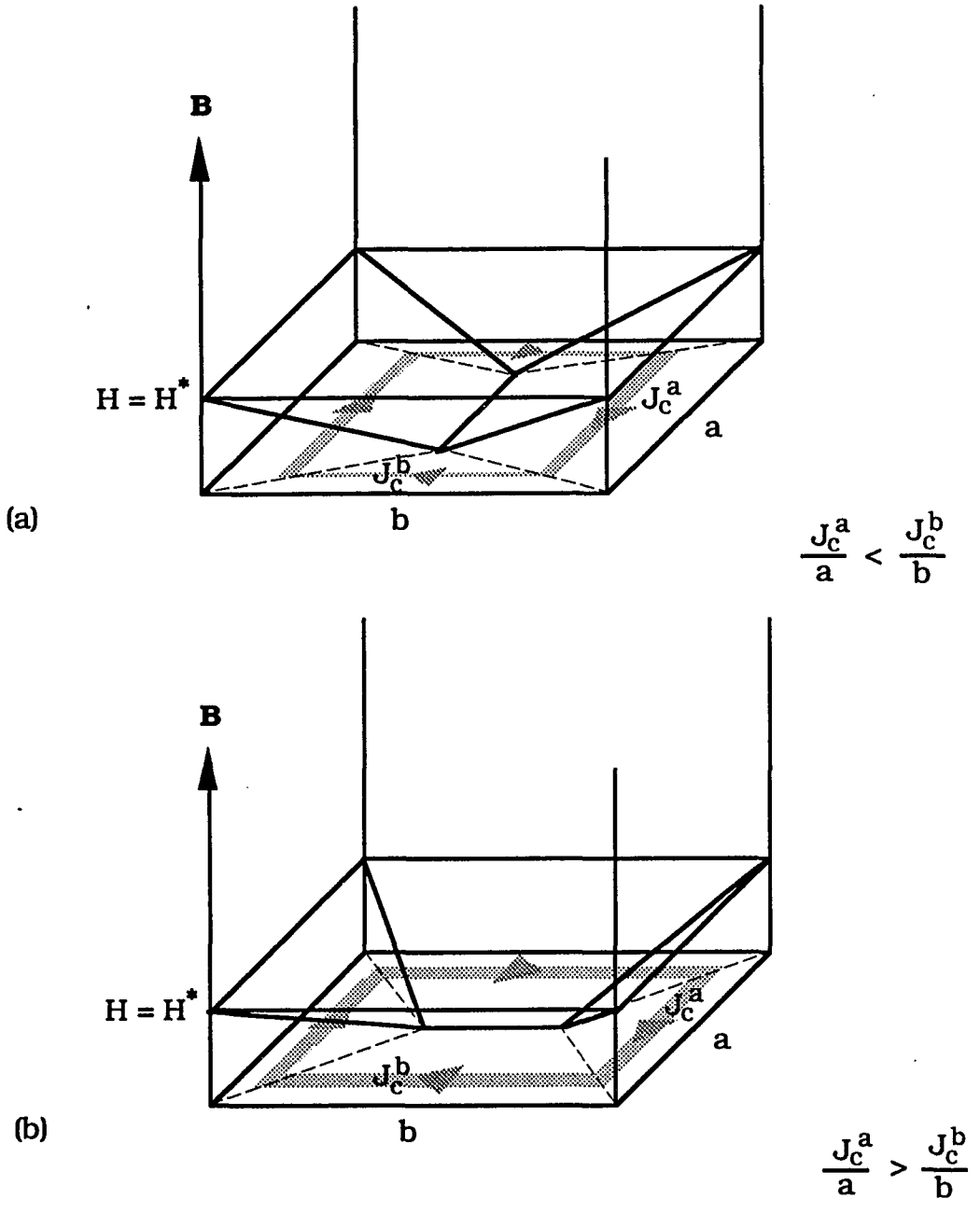

Fig. 2.8 The local magnetic field distributions at full penetration field H^* in the critical state model during the magnetization of the superconductor rectangle of size a × b : (a) $J_c^a/a < J_c^b/b$; (b) $J_c^a/a > J_c^b/b$

If $J_c^a/a > J_c^b/b$, the full penetration field $H^* = (2\pi\, b/c)\, J_c^b$. and the width of magnetic hysteresis loop is

$$\Delta M = \frac{J_c^b a}{2c}\left(1 - \frac{J_c^b a}{3 J_c^a b}\right) \qquad (2.39)$$

For a $YBa_2Cu_3O_{7-d}$ single crystal, if the magnetic field H is parallel to the c axis, the critical current density in the a-b plane is uniform, i.e., $J_c^a = J_c^b = J_c^{ab}$. Then the width of magnetic hysteresis loop is

$$\Delta M = \frac{J_c^{ab} a}{2c}\left(1 - \frac{a}{3b}\right), \qquad \text{if } a < b \qquad (2.40)$$

The critical current density J_c^{ab} could easily solved from Eq. 2.40. However, if the magnetic field is parallel to the a-b plane, finding critical current density from either Eq. 2.38 or Eq. 2.39 becomes difficult. Because there are two unknown variables J_c^c and J_c^{ab} involved in one equation, a ΔM from one measurement of magnetic hysteresis could not decouple these two. One way to solve this difficulty is to use two crystals of different sizes but similar microscopic defect structures such as two crystals from the same batch of crystal growth, assume the J_c^c and J_c^{ab} are the same for both crystals and measure their magnetic hysteresis loops separately. Then the two variables J_c^c and J_c^{ab} could be solved from two equations derived from Eq. 2.38 or Eq. 2.39 [E. M. Gyorgy et at, 1989]. The other way to solve this difficulty is to use a thick crystal. As shown in Fig. 2.9, in a $YBa_2Cu_3O_{7-\delta}$ single crystal, J_c^c is much smaller than J_c^{ab} ($J_c^{ab}/ J_c^c \approx 30 - 100$). If the crystal is thick ($a^* \sim c^*$), then there is a relation $J_c^{ab}/a^* >> J_c^c/c^*$. That means the flux front reach the middle of the crystal from the a-b direction instead of the c direction and Eq. 2.38 becomes

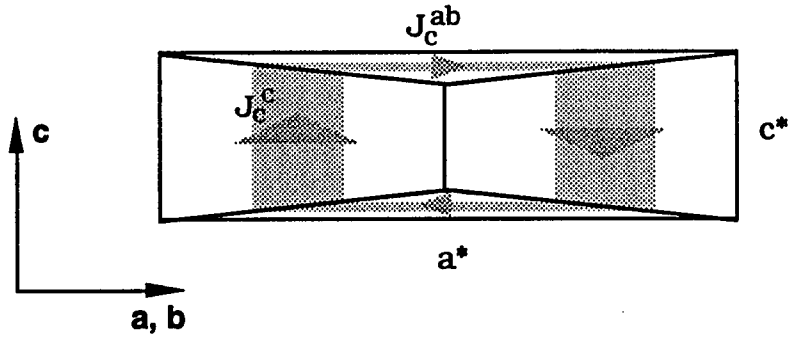

Fig. 2.9 In a thick $YBa_2Cu_3O_{7-\delta}$ single crystal, magnetic flux front reaching the middle of the crystal from the a-b direction instead of the c direction

$$\Delta M = \frac{J_c^c a^*}{2c}\left(1 - \frac{J_c^c a^*}{3 J_c^{ab} c^*}\right) \approx \frac{J_c^c a^*}{2c} \qquad (2.41)$$

Therefore, when the field direction is parallel to the a-b plane, the J_c^c could be derived from the width of magnetic hysteresis loop by Eq. 2.41. Eq. 2.40 and Eq. 2.41 are the two equations used in this experiment to derived the critical current densities from the width of magnetic hysteresis loops.

2.3.3 Length scale of a high T_c superconductor

A recently developed critical state model could reveal whether a superconductor is fully connected or is granular in nature [M. A. Angadi et al., 1991]. For $YBa_2Cu_3O_{7-\delta}$ single crystal, there is a speculation of granularity [M. S. Osofsky et al., 1992]. If this is true, the physical dimensions of the crystal could no longer be used in Eq. 2.40 and Eq. 2.41 to derive critical current density from the width of the magnetic hysteresis loop, instead the average size of the grain in the crystal should used. Therefore, the length scale of the crystal is an important issue in determination of the critical current density from the Bean model.

If a thin uniform disc of superconductor has radius R and thickness t, the length scale of this disc is simply R. As shown in Fig. 2.10, if the field decreases by a small amount δH during the decreasing magnetization after reaching the maximum field H_m, the direction of the critical current density on the edge of the disc reverses its direction to maintain the total flux. Assume the critical current density is independent of local magnetic field as in Eq. 2.28. Thus

$$\delta\Phi + cL(r)\delta I = \pi r^2 \delta H + cL(r)(2J_c t\delta r) = 0 \qquad (2.42)$$

where L(r) is the self-inductance of a ring of radius r, width δr and thickness t. The formula for L(r) is

$$L(r) = \frac{4\pi r}{c^2}\left(\ln\left(\frac{8r}{t}\right) - \frac{1}{2}\right) \qquad (2.43)$$

From Eq. 2.42, the rate of changing r as decreasing the field is

$$\frac{dr}{dH} = -\frac{cr}{8J_c t\Theta(r)} \qquad (2.44)$$

where

$$\Theta(r) = \ln\left(\frac{8r}{t}\right) - \frac{1}{2} \qquad (2.45)$$

The magnetic moment m is

$$\begin{aligned} m &= -\frac{1}{2c}\int_{0<r'<r} r' J_c dV' + \frac{1}{2c}\int_{r<r'<R} r' J_c dV' \\ &= \frac{\pi J_c t}{3c}(2r^3 - R^3) \end{aligned} \qquad (2.46)$$

Therefore the initial slope of the 'reverse leg' of the magnetization is

$$\begin{aligned} \frac{dm}{dH} &= \frac{dm}{dr}_{r=R} \times \frac{dr}{dH_{r=R}} = -\frac{2\pi J_c t}{c} R^2 \times \frac{cR}{8J_c t\Theta(R)} \\ &= -\frac{\pi R^3}{4\Theta(R)} \end{aligned} \qquad (2.47)$$

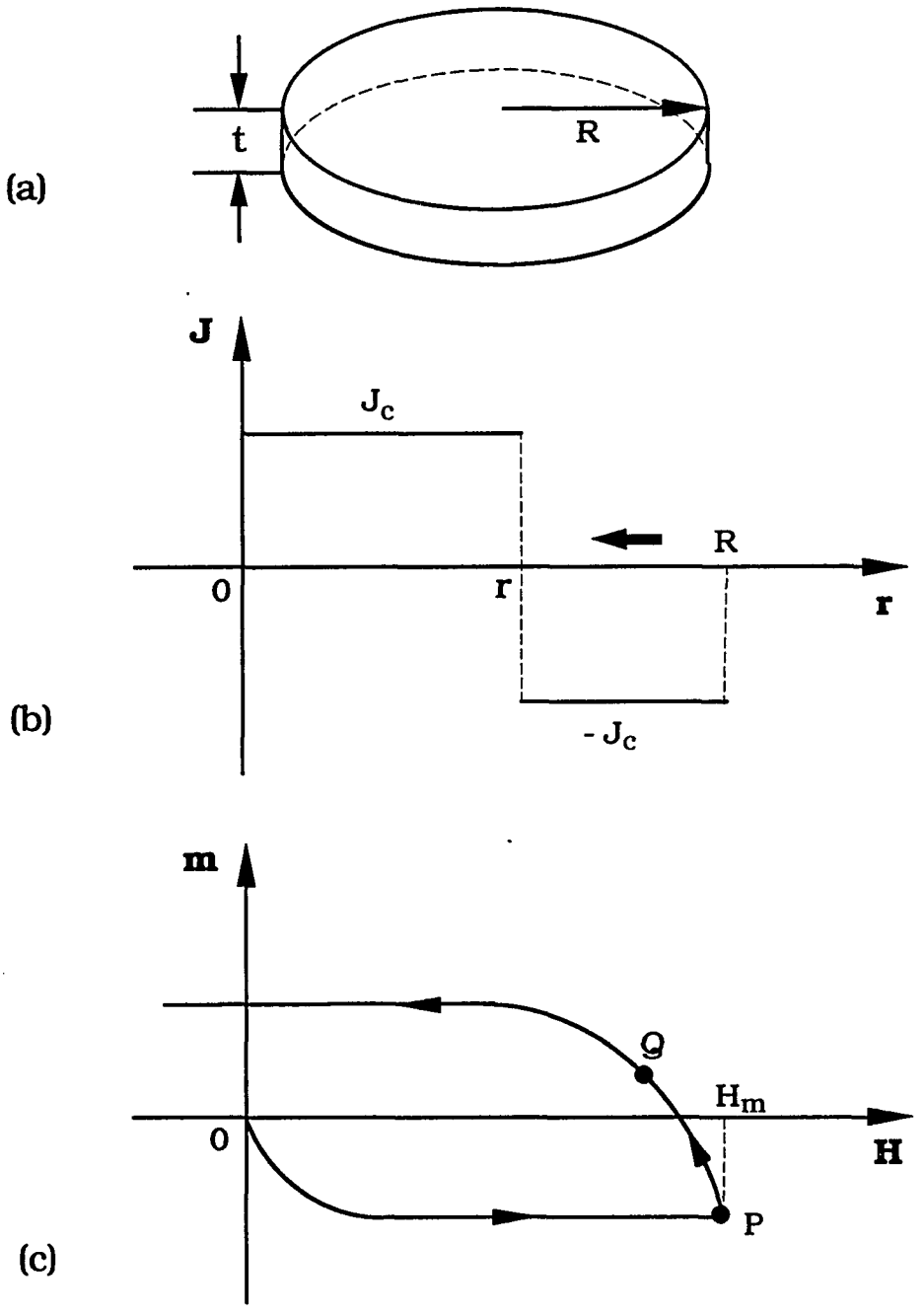

Fig. 2.10 (a), The disc of radius R and thickness t; (b) and (c), The front of negative critical current density expanding from R to r as the 'reverse leg' magnetization going from P to Q.

This means the slop of the initial 'reverse leg' of the magnetization is only dependent on the length scale of the sample and independent of the field and the critical current density. A useful scale of field decrement in measuring dm/dH is the field at which the screening current change direction completely. From Eq. 2.44 , the field range with in which the dm/dH should be measured is

$$\Delta H = \frac{\Delta r}{cr}(8J_c t\Theta(r)) \xrightarrow[\Delta r \approx r, \Theta(r) \approx 1]{} \frac{8}{c} J_c t \qquad (2.48)$$

For a typical crystal of $J_C = 7 \times 10^5$ A/cm^2 at 10 K and zero field and thickness of t = 0.3 mm, $\Delta H \sim 1$ Tesla.

If the thin disc of the superconductor contains many high critical current density regions connected by weak links, the slope of the 'reverse leg' magnetization is different than Eq. 2.47. As shown in Fig. 2.11, assume the high critical current density regions have an average radius Λ and there are total N such regions. Thus, the slope is

$$\frac{dm}{dH} = -N\frac{\pi\Lambda^3}{4\Theta(\Lambda)} = -R^2\frac{\pi f\Lambda}{4\Theta(\Lambda)} \qquad (2.49)$$

where $f = N(\Lambda^2 / R^2)$ is the filling fraction of total such regions in the disc. Usually f should be very close to 1 because the inter-granular volume is much less than the volume of the total grains. As implied by Eq. 2.45, the $\Theta(\Lambda)$ is a slow function of Λ. Thus $\Theta(\Lambda) \approx \Theta(f\Lambda)$, for $f \approx 1$ and $\Lambda >> t$. The Eq. 2.49 becomes

$$\frac{dm}{dH} = -\frac{A f\Lambda}{4\Theta(f\Lambda)} \qquad (2.50)$$

where $A = \pi R^2$ is the area of the disc. If the slope of 'reverse leg' of the magnetization is measured, $f\Lambda$ could be solved from Eq. 2.50 iteratively and the length scale Λ of the disc could be very well estimated by the approximation $f \approx 1$.

The units for the variables in Eq. 2.47 and Eq. 2.50 are 'emu' for m, 'oersted' for H and 'centimeters' for R and Λ.

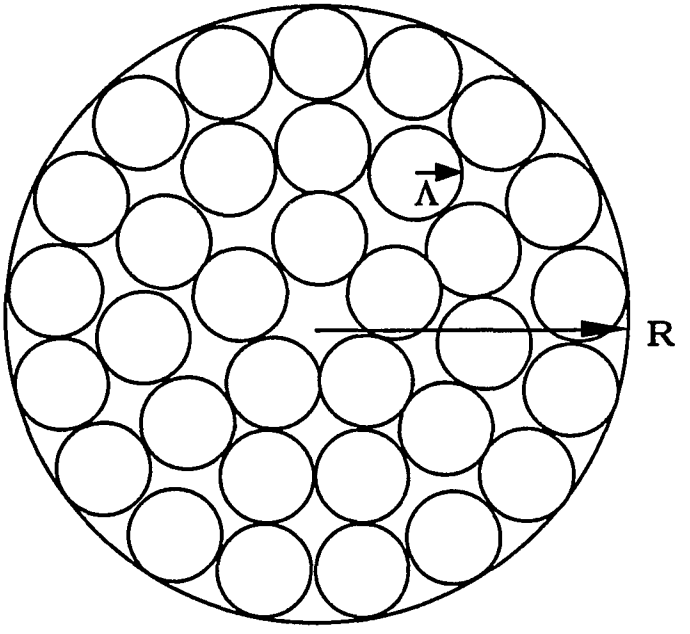

Fig. 2.11 A thin disc of radius R and thickness t containing total N high critical current density regions of average radius Λ.

CHAPTER 3. EXPERIMENT

3.1 Crystal Growth

A flux growth method was chosen for the preparation of $YBa_2Cu_3O_{7-\delta}$ single crystal using high purity Y_2O_3 (99.999%), $BaCO_3$(99.99%) and CuO (99.99%) as starting materials [M. A. Damento et al., 1987]. As shown in Table 3.1, the melting points of these materials are very high relative to the decomposition temperature of $YBa_2Cu_3O_{7-\delta}$ of about 1020 °C [D. L. Kaiser et al., 1987]. It is very important to find a proper solvent which melts at relatively low temperature in order to employ flux growth method. Fortunately, the BaO-CuO system has a low eutectic point, at 870 °C a mole composition of 28% BaO and 72% CuO mixture begins to melt [G. Balestrino et al., 1987]. This is a very good solvent because it doesn't introduce other kinds of impurity materials. If the molar ratio of Y_2O_3, $BaCO_3$ and CuO mixture is in the shaded region of the phase diagram [Fig 3.1], no additional flux is needed. Many possible compositions in that area have been tested and the most successful choice in this experiment is listed in Table 3.2.

Powders of Y_2O_3, $BaCuO_3$ and CuO were carefully weighed and thoroughly mixed together with a pestle and a mortar. If the mixture total was more than 10 grams, it was helpful to add some methanol into the mixture during the grinding to prevent the powder from spilling out of the mortar and changing the correct mole composition thereafter. The mixture was put into gold crucibles which in turn were placed on an alumina tray, the crucibles were loosely filled to 2/3 full. Then the

Table 3.1 Physical Properties of Y, Ba and Cu Compound

	Y_2O_3	$BaCO_3$	BaO	CuO	$YBa_2Cu_3O_{7-\delta}$
Molar Weight	225.81(g)	197.35(g)	153.33(g)	79.54(g)	666.22(g)
Melting Point	2410 °C		1923 °C	1326 °C	1020 °C

Table 3.2 The Composition of the Mixture for Crystal Growth

	$YO_{1.5}$	$BaCO_3$	CuO
Mole %	4	26	70
Weight %	4.05	46.03	49.84

crucible tops were loosely covered by a platinum foil to prevent dust particles from falling into the crucibles and the whole tray was slid into an inconel tube furnace [Fig 3.2]. The entire crystal growth process was performed in a flowing oxygen environment.

A good temperature controller was essential to crystal growth. It must be able to control the temperature fluctuation inside the furnace within 1 °C of the set point and cool the furnace by about 1 °C/hour. Based on these requirement, temperature controller Omega 2042K-DC1-DC2 was chosen in this experiment. After fine tuning, the controller could stabilize the temperature inside furnace with 1 °C fluctuation at 1000 °C.

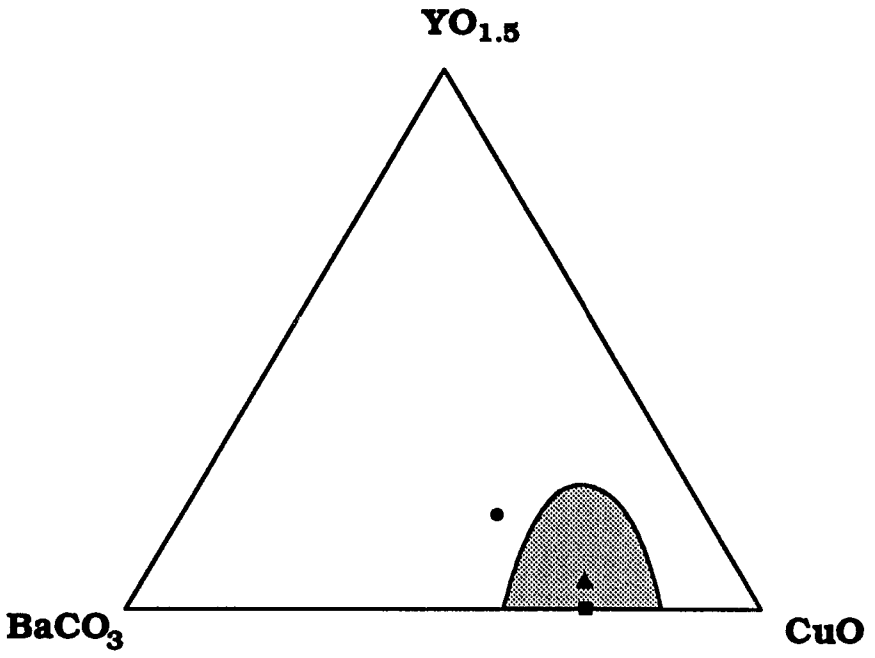

- • $YBa_2Cu_3O_7$
- ▲ The composition in Table 3.2
- ■ The eutectic point, 28 mole% $BaCO_3$ and 72 mole% CuO

Fig. 3.1 The phase diagram of $YO_{1.5}$, $BaCO_3$ and CuO system

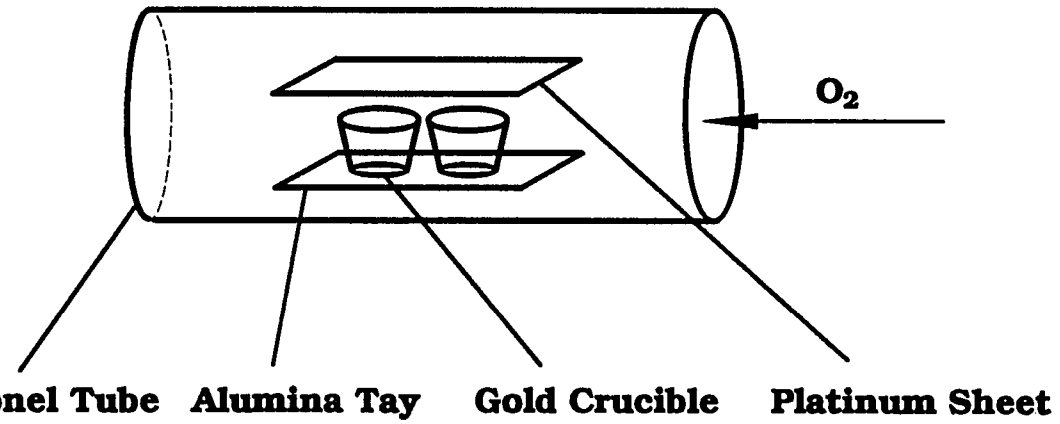

Fig 3.2 The inconel tube furnace for crystal growth

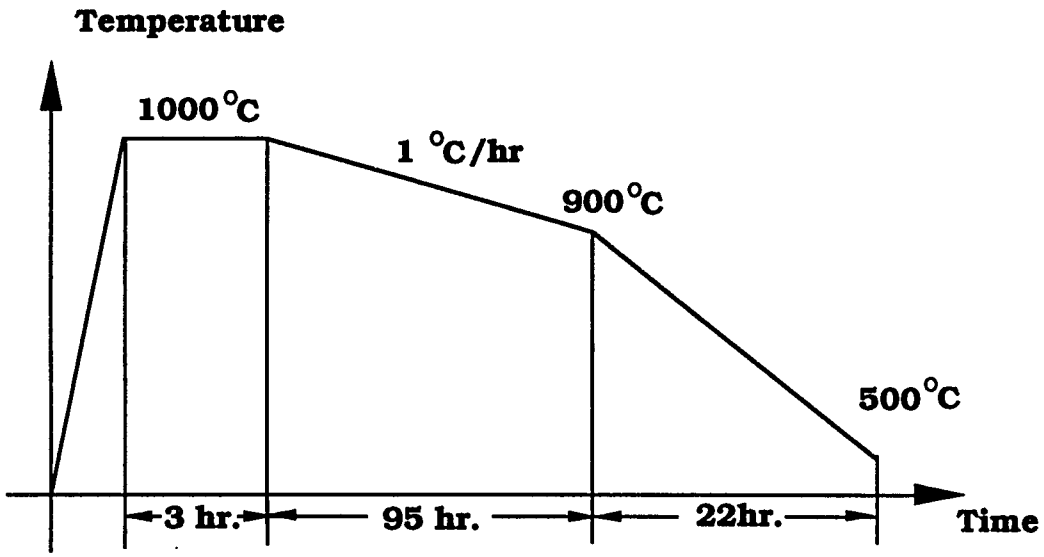

Fig 3.3 The temperature profile for the crystal growth

Temperature range for slow cooling was a vital part for flux growth method. It was reported that the most favorable temperature for $YBa_2Cu_3O_{7-\delta}$ single crystal growth was around 970 °C [D. L. Kaiser et al., 1987]. In our own test, the mixture solidified around 900 °C at which crystals stopped growing. Therefore, slow cooling range for crystal growth was set from 1000 °C to 900 °C. After a few trials, one of the successful temperature profile was found to be the following: heat the mixture up to 1000 °C as fast as the furnace can, hold at 1000 °C for 3 hours, cool down to 900 °C in 95 hours (~ 1 °C/hr), cool down to 500 °C in 22 hours (~ 18 °C/hr.), then the furnace is shut off [Fig. 3.3].

After 5 days of growth, numerous crystals were found in the cracks of flux and the bottoms of the crucibles. A typical size of the crystal was 0.87x0.75x0.29 mm^3 and the weight was 1.23 mg. The as-grown crystals had onset transition

about 92 K and transition width about 10 K for 90% completion of superconducting transition.

Subsequent annealing was needed to narrow the transition width and increase T_c. A typical annealing procedure was the following: heat the crystals to 800 °C, hold at this temperature for 100 hr, slowly cool to 300 °C in 100 hr (5 ° C/hr) and shut down the furnace. Then the magnetization of the crystals was measured to determine the T_c and transition width. The whole process may be repeated 2 or 3 times. After annealing the transition width was reduced to about 1.5 K, and T_c was slightly increased by about 0.5 K to 92.5 K.

Fig. 3.4 is a picture of a well annealed and polished crystal. Under a polarized light the twin structure is clearly revealed. The cracks in the picture are the consequence of mechanical polishing. Fig 3.5 is the magnetization data of a well annealed crystal, showing the transition temperature and width.

3.2 Magnetization Measurements

The magnetization data of the crystals were taken by a commercial SQUID magnetometer, model MPMS made by Quantum Design. The superconducting magnet in the SQUID could generate magnetic fields up to 5.5 T with precision of 0.1 G for fields less 5000 G or 1 G for fields higher than 5000 G. The temperature controlling unit in the SQUID maintained the desired sample temperature from 2 to 400 K with accuracy of 0.5% of set point. The SQUID had dipole pick up coils about 3.5 cm apart and could detect a signal as small as 10^{-6} emu, which was enough for measuring a 0.1 mg $YBa_2Cu_3O_{7-\delta}$ single crystal. The whole system was interfaced with an HP computer for the integrated control at

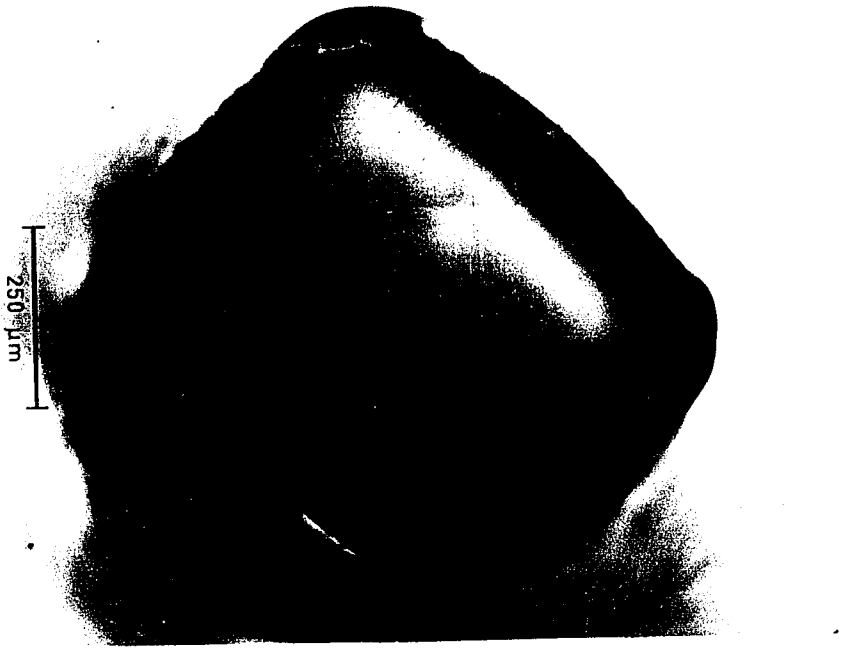

Fig. 3.4 A crystal under polarized light

software level. This equipment provided means for very sensitive measurements of magnetic moments.

Magnetic field homogeneity was of crucial importance in this experiment because hysteretic properties were studied. It was pointed out that the field gradient could produce erroneous results for magnetic moment measurements if hysteretic effects were present [Y. Xu et al., 1989; Lichtenberger, 1991]. Good field homogeneity could be achieved by choosing short scan length. It shouldn't be too short because the separation of the pick up coils in the MPMS was about 3.5 cm. Table 3.3 shows the variation of the field with respect to the scan length, specified in the Quantum Design MPMS manual. From these consideration, a scan length of 4 cm, which corresponds to 0.19% field inhomogeneity, was chosen for all magnetic moment measurements in this research.

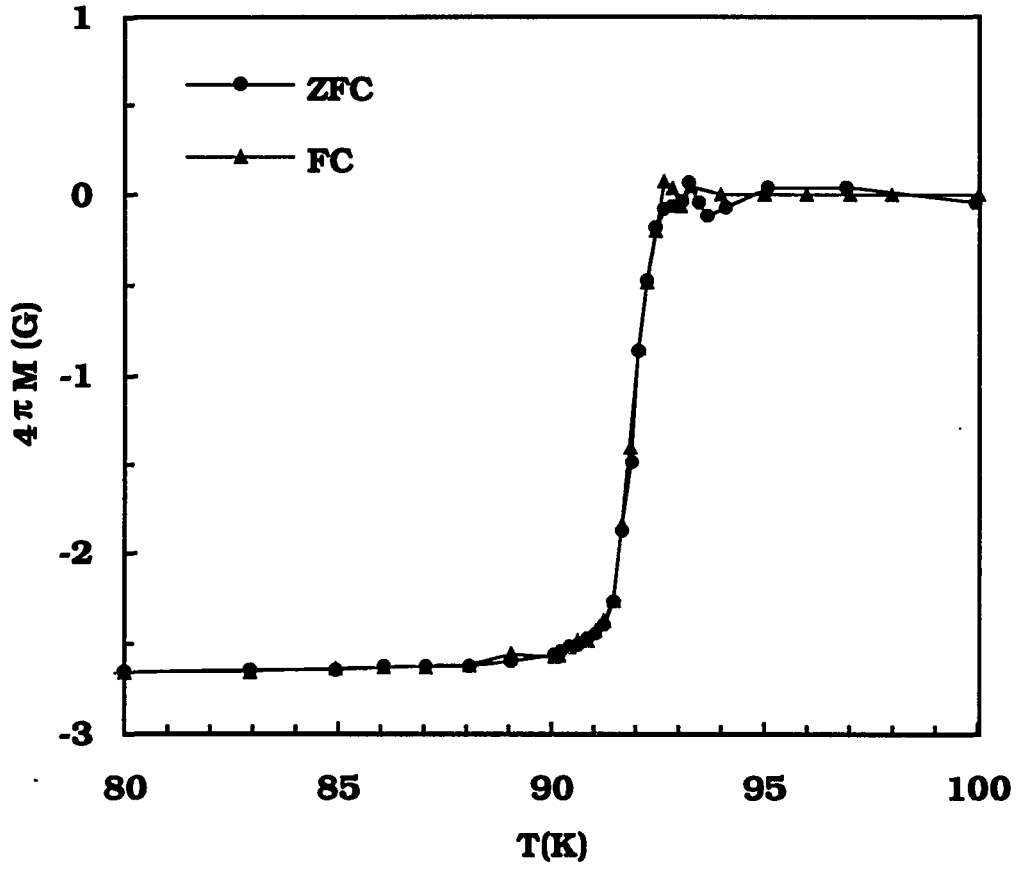

Fig. 3.5 Magnetization data of a well annealed crystal at H = 5 Oe and parallel to the c axis. The demagnetization factor was 0.65.

Magnetization vs. Temperature (M vs. T) and Magnetization vs. Applied field (M vs. H) were two major magnetization measurements in this experiment. The M vs. T data determined the transition temperatures and transition widths of the crystals, the M vs. H determined the hysteresis loop of the crystals. Using the anisotropic critical state model, the critical current density could be derived from the width of the hysteresis.

Table 3.3 Field variation vs. scan length for SQUID MPMS

Scan length (cm)	Field variation (%)
1.0	0.001
2.0	0.005
3.0	0.048
4.0	0.19
6.0	1.4
8.0	5.8

In low field magnetization measurement, the remnant magnetic field in the magnet could cause significant error to magnetization data unless care was taken to remove trapped flux in the magnet. For measuring fields of several hundred Oe, the remnant field could lead to errors in H field of several percent if care was not taken to 'de-gauss' the magnet. For measuring fields of several Oe, the remnant field could lead to absurd results. As shown in Fig. 3.6, in M vs. T measurement at 10 Oe, the Field Cool data had a positive jump while the Zero Field Cool data having a negative jump after cooling below the super-conducting transition temperature . This was because of the trapped flux in the magnet making a real field at the sample different from the field expected from the total current in the magnet windings. This phenomenon happened quite often to irradiated $YBa_2Cu_3O_{7-\delta}$ crystal samples when remnant fields were higher than 5 Oe.

The remnant fields were determined by M vs. H measurement. The $YBa_2Cu_3O_{7-\delta}$ crystal samples had a linear magnetization region, i.e., Meissner effect region, the M vs. H data fitted into a straight line, the cross point on the H axis when M was equal to zero was the value of the remnant field.

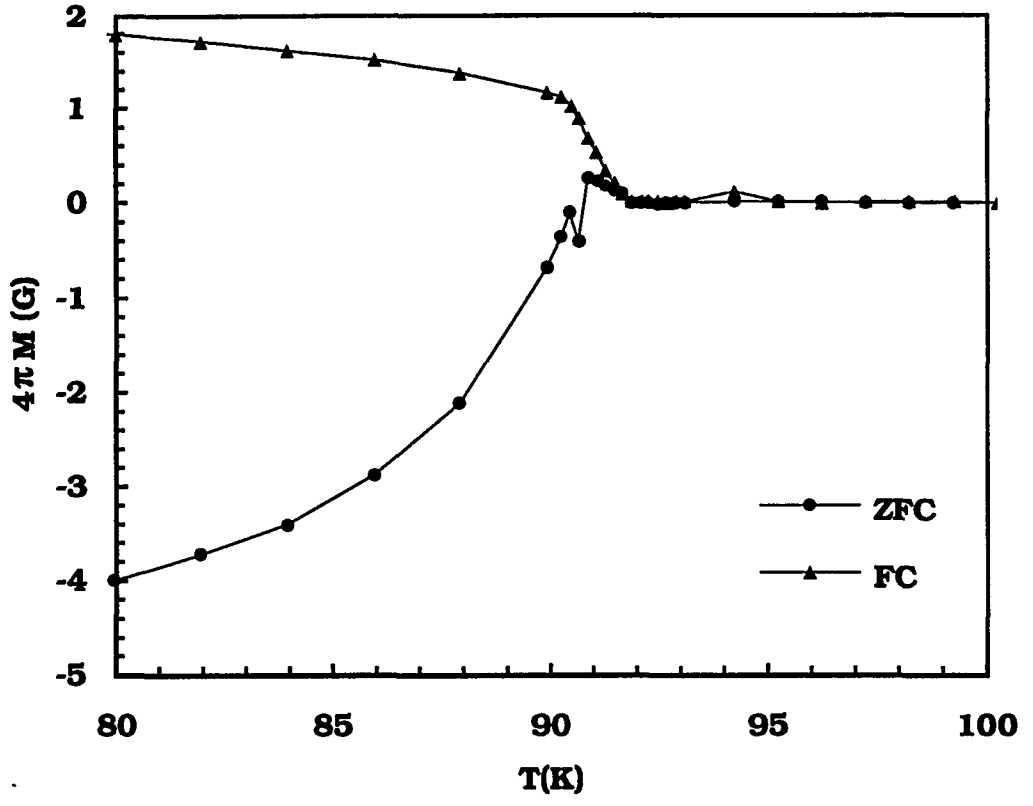

Fig. 3.6 The positive jump of Field Cool data in M vs. T measurement. The field applied was 10 Oe and the remnant field was 5.4 Oe.

To remove this remnant field, a 'de-guassing' sequence was performed before each magnetization measurement in this experiment. One of the best sequence of 'de-gaussing' was found to be the following: first, warm the sample chamber above the superconducting transition temperature (typically 130 K); second, put the field control in oscillatory mode; third, increase magnetic field to 5 T; fourth, discharge the magnet to 0 T. The remnant field after the 'de-gaussing' sequence was less than 1 Oe and it could be treated as a constant field superposed on the applied

field. Also, the positive jump in Field Cool data of M vs. T measurement disappeared after the 'de-gaussing' sequence.

Depending on the orientation of the sample relative to the magnetic field direction, several kinds of sample holder were use in this experiment [Fig. 3.7]. Holder "a" was a thin quartz tube with an indentation fused in the middle on which the sample rested. A teflon adapter on the top of the quartz tube permitted connection to motion apparatus of the SQUID. This holder was primarily used to measure crystals with magnetic field aligned along the c axis. Holder "b" was a thin quartz rod with a teflon adapter on top of a quartz rod and a teflon spacer at the bottom of the rod. The crystal sample was glued with GE 7301 varnish to the side of the rod. This holder was primarily used to measure crystal samples with magnetic field aligned along the a-b plane. Holder "c" had a phenolic rod as a main body and a short quartz rod glued onto the phenolic rod with GE 7301 varnish. The end of the rod was cut to a specific angle. The crystal sample was glued on the angle cut with the varnish. This holder was primarily used to study the change of magnetization with a big angle tilt such as 45°. Holder "d" was a thin quartz rod with a nylon adapter on the top and a nylon spacer at bottom of the rod and a very fine quartz rod glued on the adapter and the spacer with a small angle tilt. The crystal sample was glued onto the side of the very fine quartz rod with the varnish. This holder was primarily used to study the change of magnetization with a small angle tilt in the range of a few degrees.

The superconducting crystal samples had to be firmly attached to the sample holders because of the diamagnetism of the superconducting sample. The torque on the sample trying to align the magnetic moment with the field was strong enough to break a poor glue bond in high field such as 5 T.

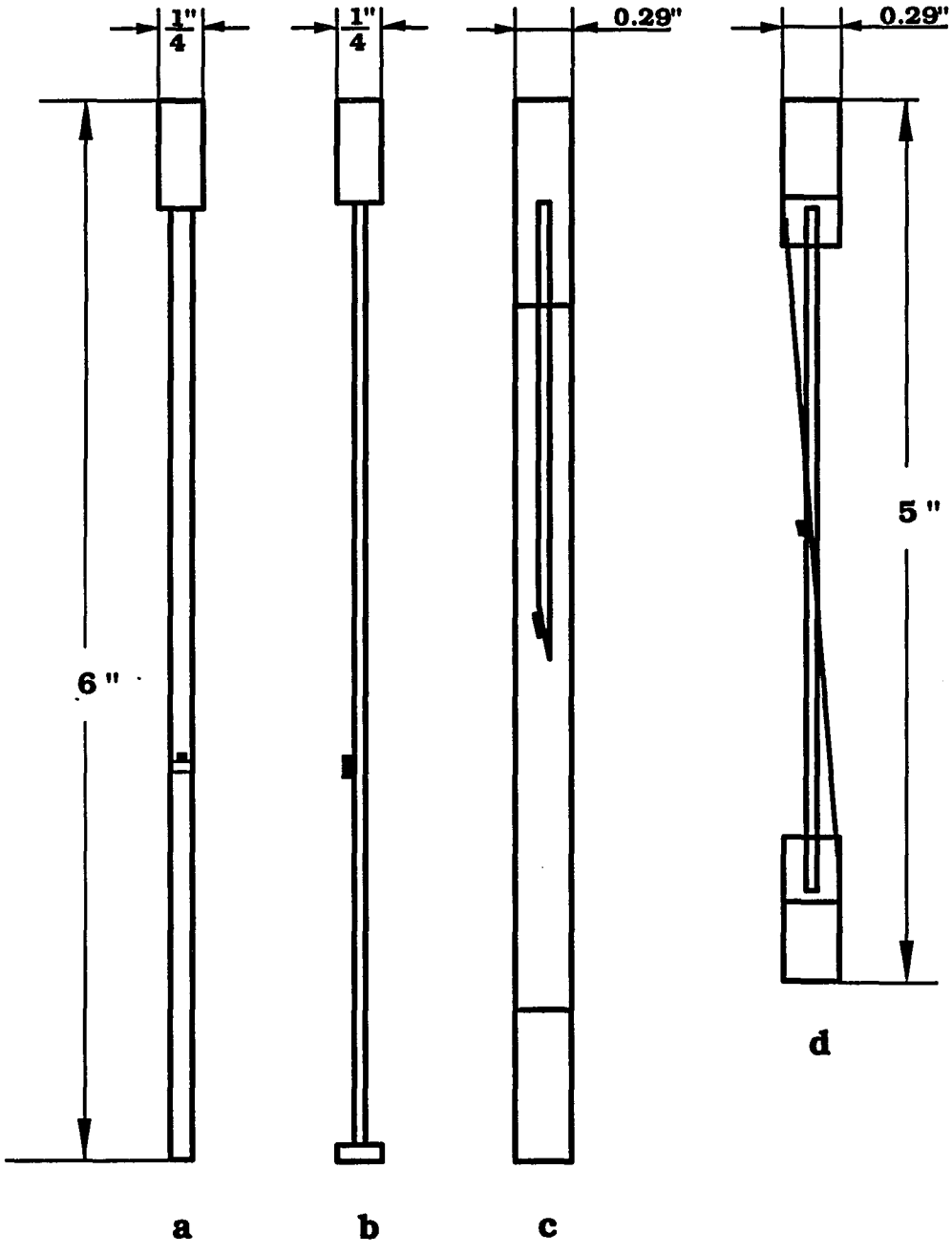

Fig. 3.7 4 different kind of holders used in this experiment

In order to firmly attach the crystal samples, when using holder "a", a small piece of teflon tape was cut and rolled into a small ball, then pushed into the quartz tube so that it pressed the top of sample firmly. When using holder "b" and "d", it was necessary to allow enough time (at least 4 hours) for the varnish to cure. When using holder "c", a piece of cigarette paper was affixed on the angle end first and the crystal sample was glued on the top of the paper. It was important to allow enough time for the varnish to cure thoroughly.

For holder "c", the accuracy of the angle cut of the quartz rod was ±1° of desired angle. For holder "d", the angle set by the fine quartz rod was measured with a traveling microscope to an accuracy of ±0.1°. When the holders were loaded into the SQUID, the holder alignment with the magnetic field of the SQUID was ± 0.1°. Therefore, the error in angle when using holder "c" was ± 1.1°, and the error in angle when using holder "d" was ± 0.2°.

. The back ground signal of these holders could be ignored when measuring critical current density in this experiment because most concern here was the width of hysteresis loop not the absolute value of the magnetization. The critical current density was derived from the width of the hysteresis loop through the Bean model. The magnetization of these holders were all linear in field and didn't have hysteresis. Therefore they didn't contribute to the width of the hysteresis loop of superconducting crystals. Fig 3.8 was the background signal of the holder "a" at 10 K and 77 K. At 10 K and 1 T, the magnetization signals from the crystal samples were 50 to 100 times larger than this background signal of the holder.

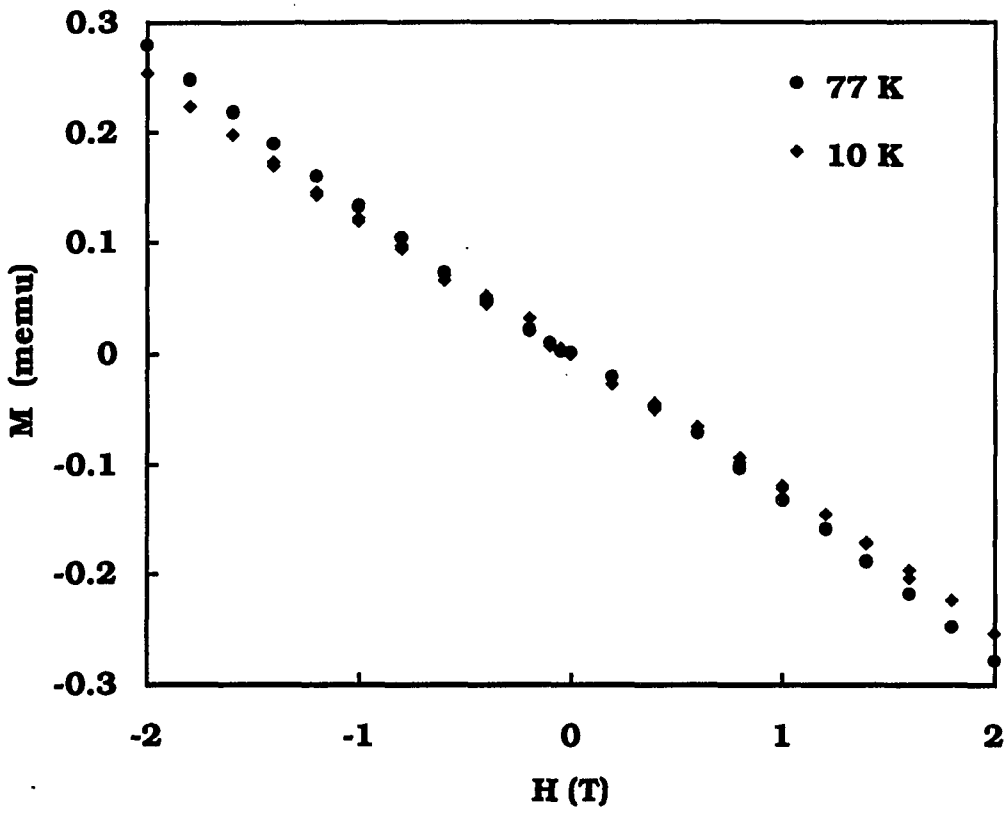

Fig. 3.8 The background signal of holder "a" at 10 K and 77 K

3.3 Irradiation Damage

After a thorough set of measurements of $YBa_2Cu_3O_{7-\delta}$ single crystals in MPMS for T_c and critical current density to characterize the unirradiated state, they were oriented and mounted on silica slides, put into aluminum boxes, sealed in dry N_2 and sent to Brookhaven National Laboratory for irradiation. The crystals were irradiated with 200 MeV protons either along the c axis or the a-b plane [Fig.

3.9]. During the irradiation, a fan was used for cooling of the crystals and the beam current was adjusted so that the temperature increase due to irradiation beam heating was less than 5 °C.

After the irradiation, the crystals were stored until the radiation levels were within safety standard before being sent back for thorough measurements again. When the irradiation fluence was at 10^{15} proton/cm^2 or below, the crystals were measured within a week of the irradiation. When the fluence was at 10^{16} protons/cm^2, for the radiation safety during shipping and handling, the crystals had to stay at Brookhaven National Laboratory for 3 months for radiation levels of the crystals to come within safety standard. After the crystals were received, they were removed from the aluminum boxes and silica slides right away. It was found that most of the radiation came from the silica slides and the aluminum boxes, the radiation from crystals was minimum, almost undetectable.

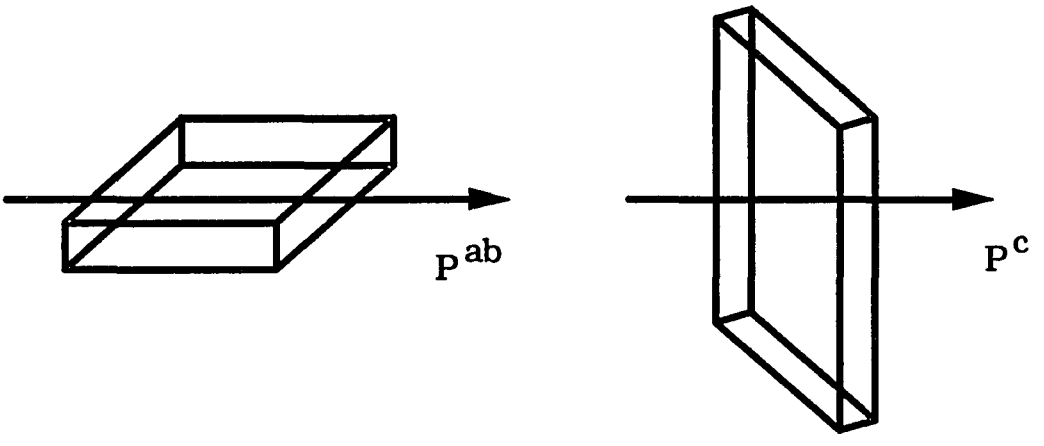

Fig. 3.9 Two different orientations for irradiation damage

CHAPTER 4 RESULTS AND DISCUSSIONS

4.1 The Nature Of The Irradiation Damage

The damage profile of high energy protons in $YBa_2Cu_3O_{7-\delta}$ material could be simulated with a computer program called TRIM (TRansport of Ions in Matter) [J. P. Biesack et al., 1980]. This was a Monte Carlo approach in which target atoms were assumed randomly located, the collisions between the incident ions and target atoms were assumed to happen after traveling a given mean free path $\lambda = N^{-1/3}$ (N was the atomic density of the target), the impact parameter P was randomly chosen between zero and $P_{max} = \pi^{-1/2} N^{-1/3}$ and the impact azimuth angle Φ was also randomly chosen between zero and 2π. The trajectory of the incident ions and the cascades of the target atoms were followed in detail and the redistribution of these target atoms was determined. The average accuracy of TRIM for stopping powers and range distributions was better than 10% compared with the experimental results [J. F. Ziegler et al., 1985].

TRIM calculations showed that 200 MeV protons had about 60 mm penetration depth in $YBa_2Cu_3O_{7-\delta}$ material [Fig. 4.1]. This was very long compared with the dimensions of the crystals (~ 1 mm). Therefore, the protons left rather uniform tracks of damage even when they traversed the crystals along the a-b plane. Fig. 4.2 was the distribution of displaced atoms by TRIM, averaging 30000 protons and assuming 20 eV for target atom displacement threshold and 2 eV for target atom lattice binding energy. These data showed that on average a 200

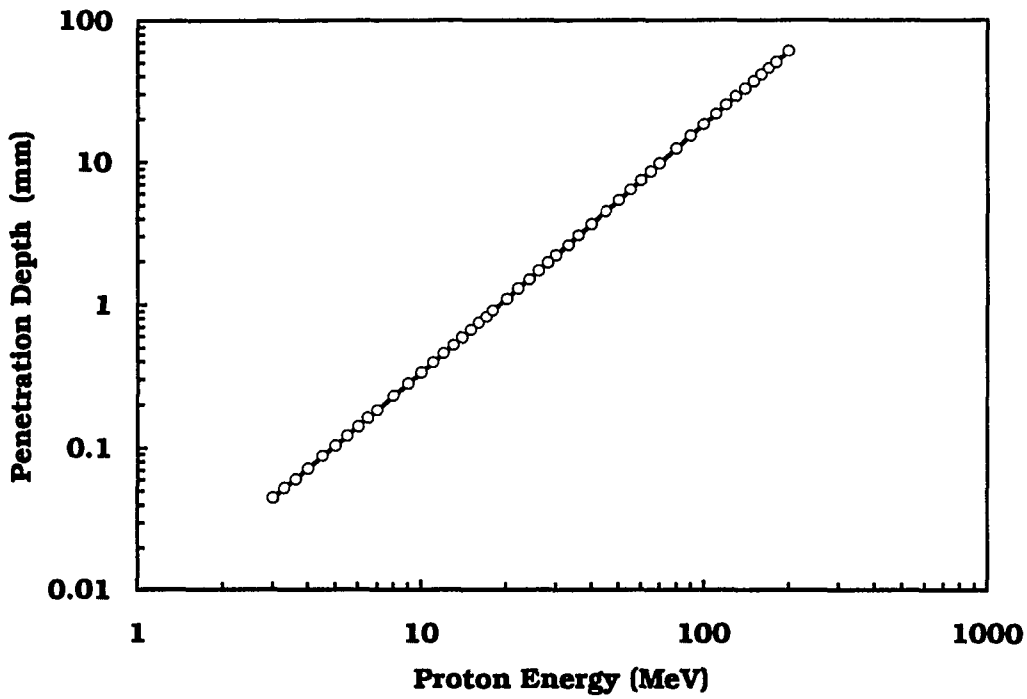

Fig. 4.1 Proton penetration depth in $YBa_2Cu_3O_{7-\delta}$

MeV proton left a quite uniform atomic displacement track through the thickness of the sample (1 mm) without cascading effects and created only 4.84 atomic displacements. Among these displacement, 38.2% were O, 29.3% were Cu, 21.5% were Ba and 11.0% were Y . Therefore, the damage by 200 MeV protons were rather light and uniform through the sample and the dominant interstitial along the damage tracks were O and Cu (68% of the total).

The transmission electron microscope (TEM) study of a pre-thinned $YBa_2Cu_3O_{7-\delta}$ crystal found only point defects and no amorphous regions right after irradiation [M. J. Kramer, Qiang Qian and D. K. Finnemore]. However, after a period of time, typically 3 months, some of those point defects clustered together

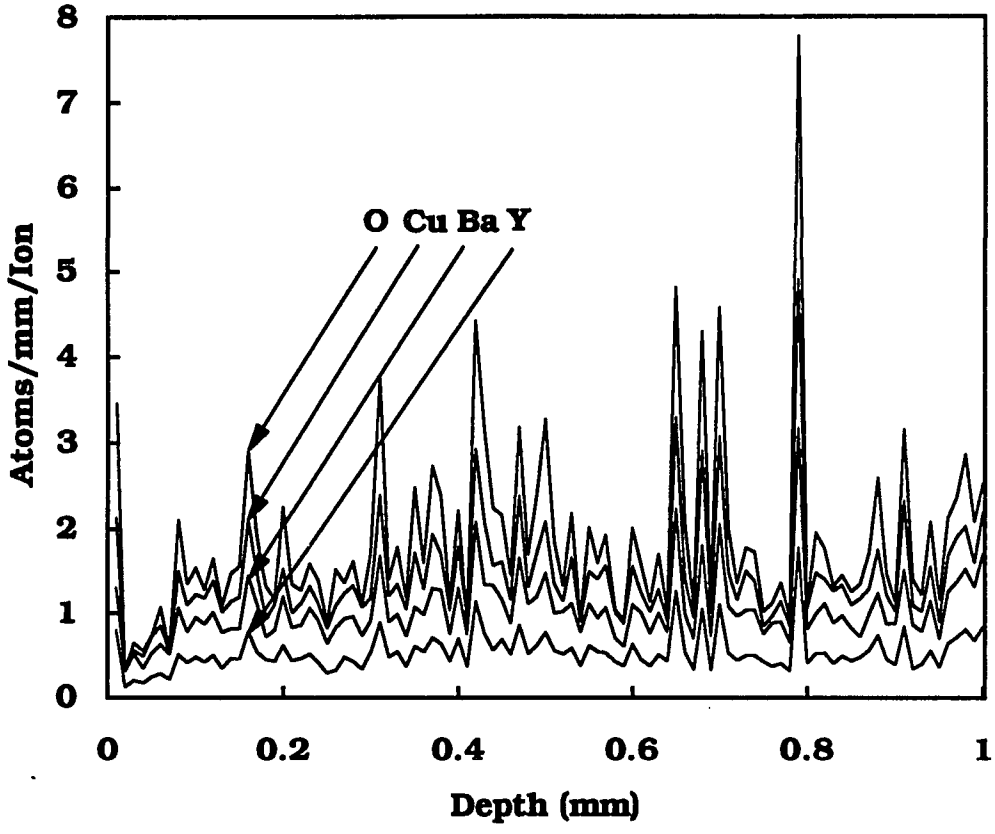

Fig. 4.2 The displaced atom distributions by 200 MeV proton by TRIM calculation averaging 30000 protons and assuming 20 eV for target atom displacement energy and 2 eV for target atom lattice binding energy.

forming single rows of defects along the a and b axis in the a-b plane. High resolution TEM lattice imaging showed these cluster defects were platelets 2 to 7 nm in length and 0.2 nm thick and concentrated in the {100} planes and along the <100> directions. From these lattice images, point defect density was approximately 10^{13} /cm^2 and cluster defect density were approximately

$10^{12}/cm^2$ for fluence of 10^{16} protons/cm^2 . The majority of these defects were O and Cu based on the result of TRIM calculation. Point defects and cluster defects were pinning centers created by the proton irradiation. It would be assumed in this discussion that these pinning centers changed the magnetization behavior and critical current density in the crystal samples.

4.2 Irradiation Parallel To The a-b Plane

4.2.1 The angle dependence of the magnetization data

There always were some difficulties aligning the magnetic field of the SQUID with the a-b plane of the crystal sample. Therefore, it was of some interest to know how sensitive the hysteresis loop widths were to rotation out of the a-b plane toward the c-axis. Holder "c" was employed to study the change of magnetization between 5° and 90°, and holder "d" was employed to study this effect between -5° and 5°. As shown by Fig. 4.3, the width of hysteresis loop was approximately symmetric about $\theta = 0°$ and rose by 0.5% of the difference between 0° and 90° values in the first degree of rotation. If the curves were carefully examined, the exact symmetry axis of these curve were slightly off the $\theta = 0°$ position by approximately 0.5°. Because holder "d" itself contributed only 0.2° error to the alignment, this 0.5° misalignment had to occurr during the process of mounting the crystal sample with the GE varnish. Therefore, when using holder "b" to align the a-b plane of the crystal sample with the magnetic field in the SQUID, the a-b plane of the crystal sample would have less than 1° misalignment after the crystal sample was affixed to the quartz rod. At 10 K and 1 T, the change of hysteresis

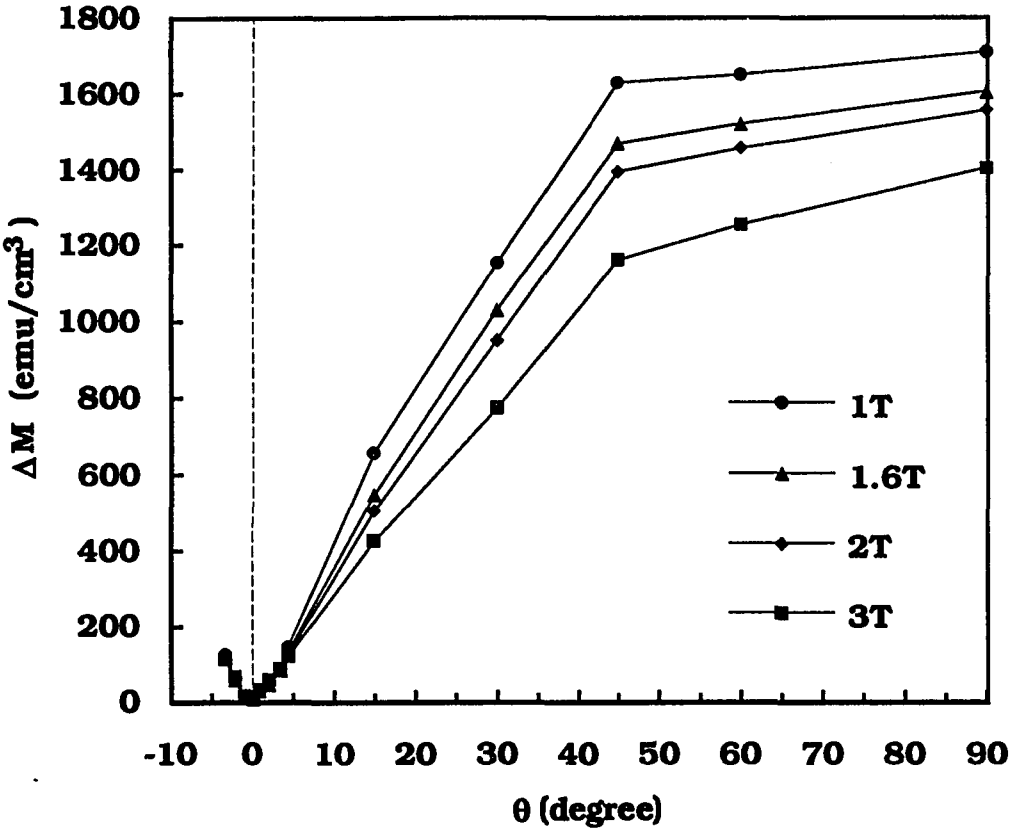

Fig. 4.3 Change in hysteresis loop width at 10 K as the field direction was rotated out the a-b plane ($\theta = 0°$) toward the c axis ($\theta = 90°$)

loop width by 1° tilt out of the a-b plane was 9 times smaller than the change by the 200 MeV proton irradiation at 10^{12} protons/cm^2 [Fig. 4.4].

When the crystal was oriented close to the c axis, that is $70° < \theta < 90°$, the hysteresis loop width became insensitive to small angle tilt. As shown in Fig. 4.3, when θ change from 90° to 70°, the width of the hysteresis loop changed only 6% at 1 T and 10 K. When the crystal was oriented close to the a-b plane, that is $10° < \theta$

< 60°, the hysteresis loop width changed linearly with the angle at about 1.5% per degree of misorientation.

4.2.2 Low fluence J_c enhancement

For low fluence (10^{12} to 10^{14} protons/cm^2) proton irradiation parallel to the a-b plane, there was a rapid enhancement of J_c^c when the fields were parallel to the damage tracks. The data shown from Fig. 4.4 to Fig. 4.7 were taken from crystal 'A'. As shown in Fig. 4.4, J_c^c at 10 K and 1 T field, increased from 2000 at zero to 50,000 at 10^{12} , to 70,000 at 10^{13} , to 170,000 A/cm^2 at 10^{14} protons/cm^2. For zero field and 10 K, the enhancement at 10^{14} protons/cm^2 was only a factor of 4, but at 1 T it was a factor of 85. Thus these defects on a percentage basis were more helpful to J_c^c in high field than that in low field. At high temperature 77 K and 1 T field, J_c^c remained at zero at 10^{12} protons/cm^2, increased to 100 A/cm^2 at 10^{13} protons/cm^2 and jumped to 2000 A/cm^2 at 10^{14} protons/cm^2 [Fig. 4.5].

If the magnetic field was rotated in the a-b plane so that the fields were perpendicular to the damage tracks, there was also enhancement to J_c^c by the irradiation. At 1 T field and 10 K, the critical current density J_c^c increased from 1,800 A/cm^2 at zero fluence to 10,000 A/cm^2 at 10^{14} protons/cm^2 , a factor of 5 [Fig. 4.6]. This meant that at 10^{14} protons/cm^2 the rotation of the field in the a-b plane by 90° reduced J_c^c at 10 K and 1 T by a factor of 17. It made a big difference whether the field was parallel or perpendicular to the damage tacks.

If the magnetic field was rotated to parallel to the c axis, there was only a few percent change of J_c^{ab} by the irradiation along the a-b plane for these low

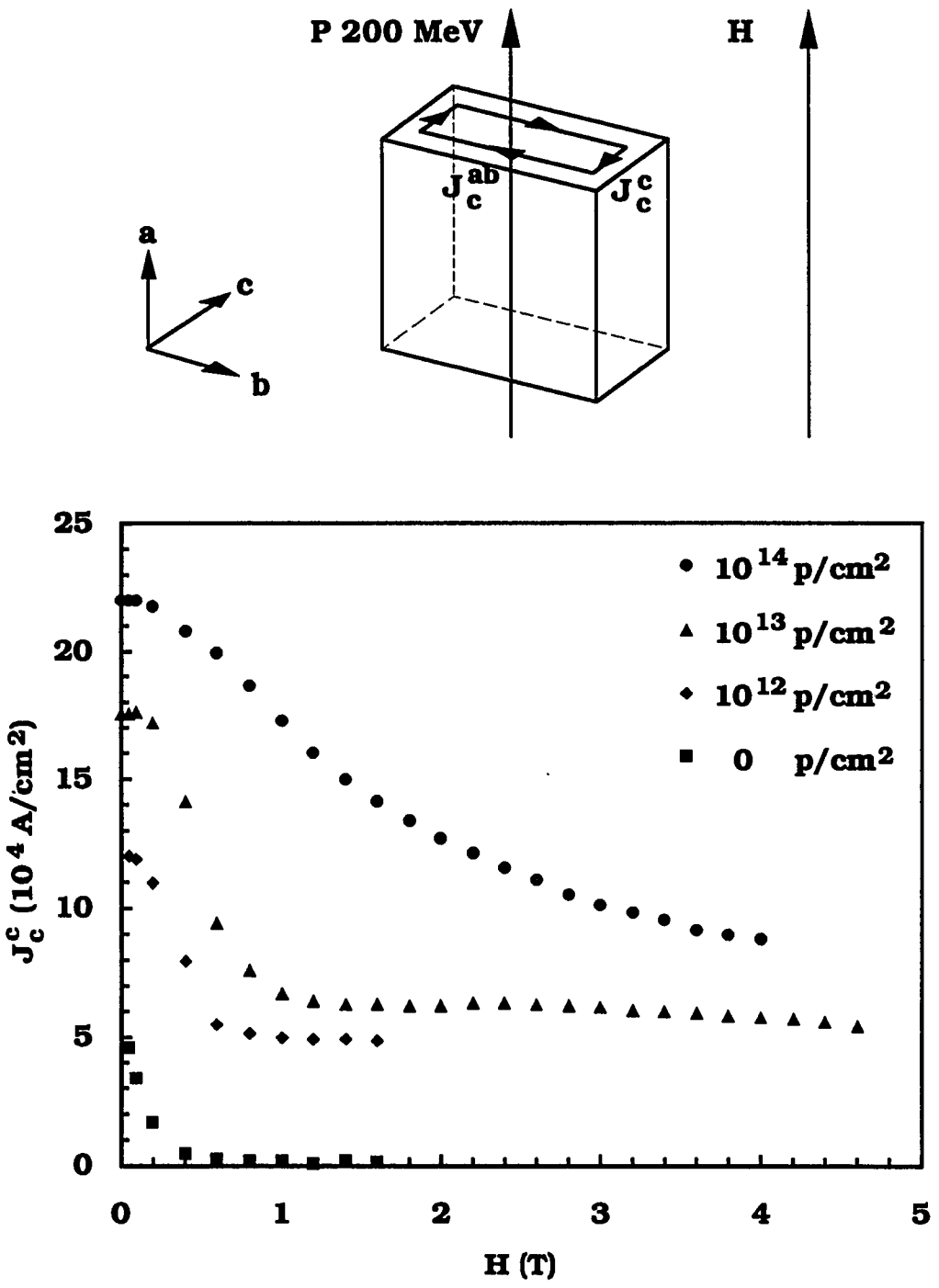

Fig. 4.4 $J_C{}^C$ enhancement at 10 K with modest fluence for radiation parallel to the a-b plane and field parallel to the radiation direction.

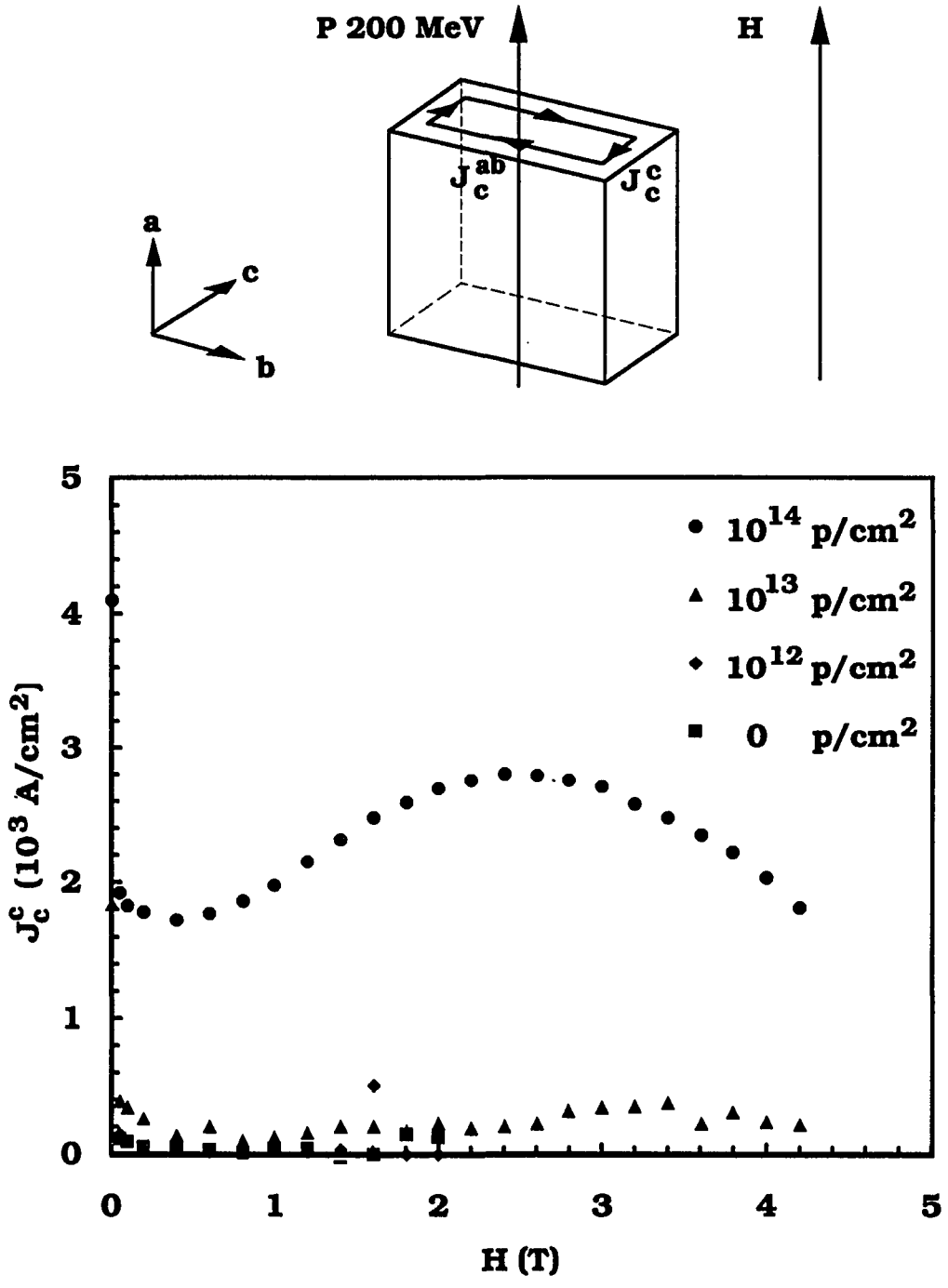

Fig. 4.5 J_C^C enhancement at 77 K with modest fluence for radiation parallel to the a-b plane and fields parallel to the radiation direction.

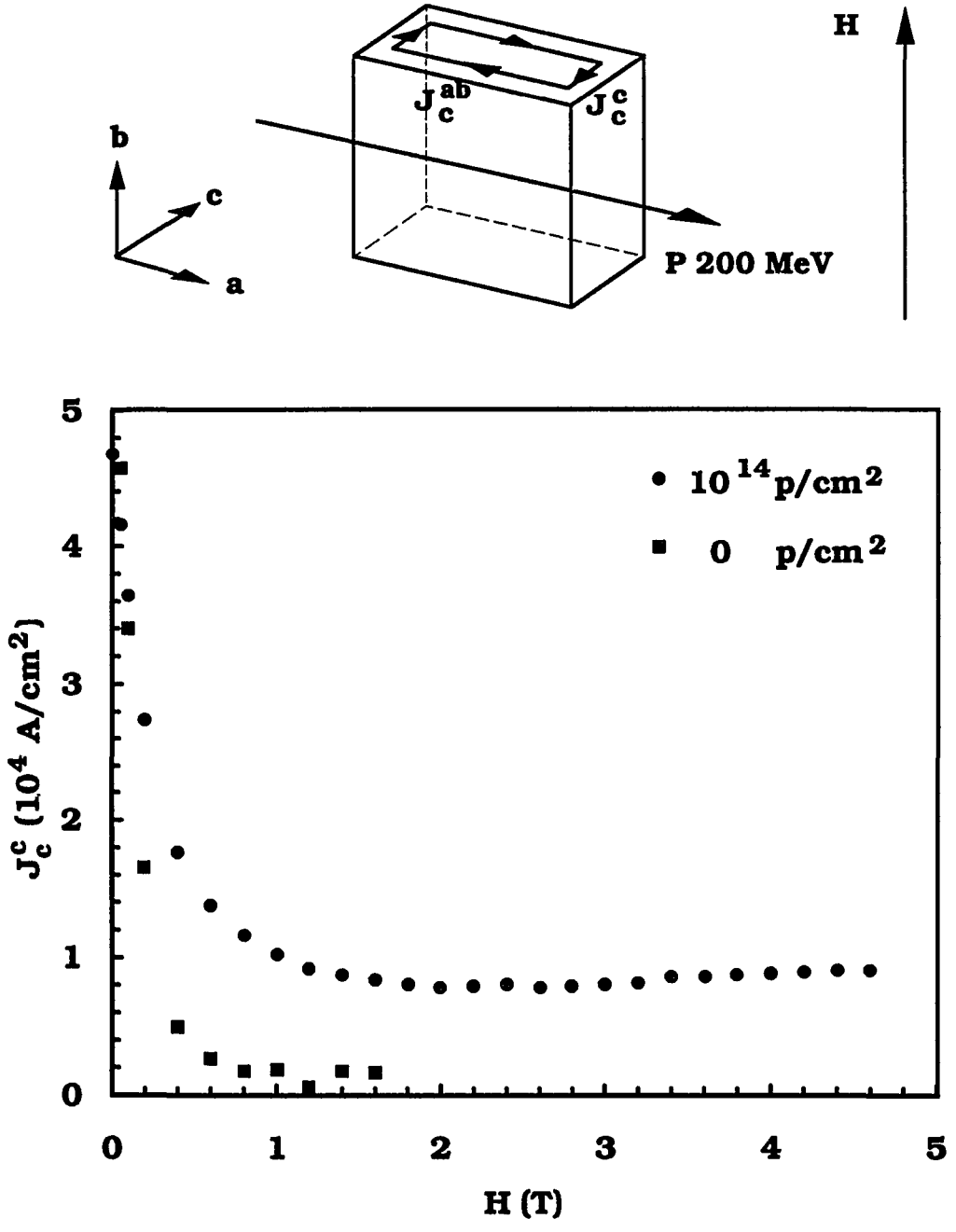

Fig 4.6 J_c^C enhancement at 10 K with modest fluence for radiation parallel to the a-b plane and fields in the a-b plane and also perpendicular to the radiation direction.

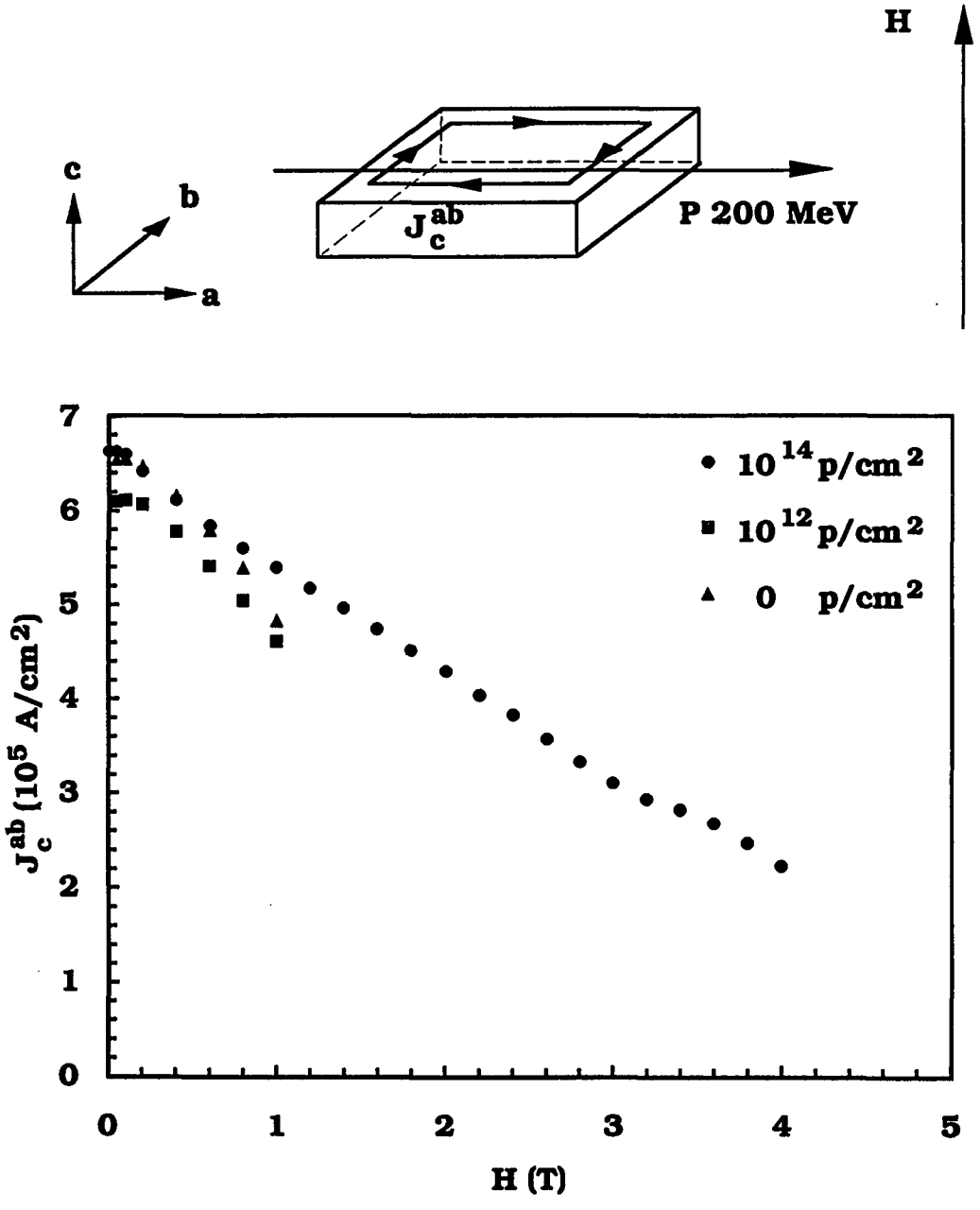

Fig. 4.7 J_c^{ab} remained unchanged at 10 K with modest fluence of radiation along the a-b plane and fields parallel to the c axis.

fluences. At 10 K, for fluence from 10^{12} to 10^{14} protons/cm^2 , J_c^{ab} remained virtually the same [Fig. 4.7].

The rapid enhancement of J_c^c at low fluence was to be contrasted with the change of a few percent in J_c^{ab} at these low fluences. The dominant effect of the irradiation to J_c^c indicated an enhanced interplanary coupling.

At this low fluence 10^{12} to 10^{14} protons/cm^2, the transition temperature T_c of the crystal samples remained constant at 92.5 K. The mechanism of superconductivity of the samples was not affected by the irradiation.

In summary, for fluence 10^{12} to 10^{14} protons/cm^2, 200 MeV proton irradiation parallel to the a-b plane enhanced J_c^c very significantly for fields parallel to the damage tracks at 10 K and 77 K. The irradiated sample show both high J_c's and a wide range of fields where J_c was high. The enhancement of J_c^c was much smaller for fields aligned perpendicular to the damage tracks and also in the a-b plane. At these radiation levels, the enhancement of J_c^{ab} for fields parallel to the c axis was only a few percent. There was no measurable change of T_c for fluence below 10^{14} protons/cm^2.

4.2.3 High fluence J_c enhancement

At high fluence, there was a small suppression of T_c as well as a major increase in both J_c^c and J_c^{ab}. As shown in Fig. 4.8, at 10^{16} protons/cm^2, the transition temperature of $YBa_2Cu_3O_{7-\delta}$ crystal sample was suppressed by 1 K. This was not observed for fluence lower than 10^{14} protons/cm^2. At fluence of 10^{15} to 10^{16} protons/cm^2, the average damage track spacing of 0.3 to 0.1 nm was comparable to the size of $YBa_2Cu_3O_{7-\delta}$ unit cell, the effects of the irradiation induced defects entered a new regime in which the J_c^c rose more rapidly with

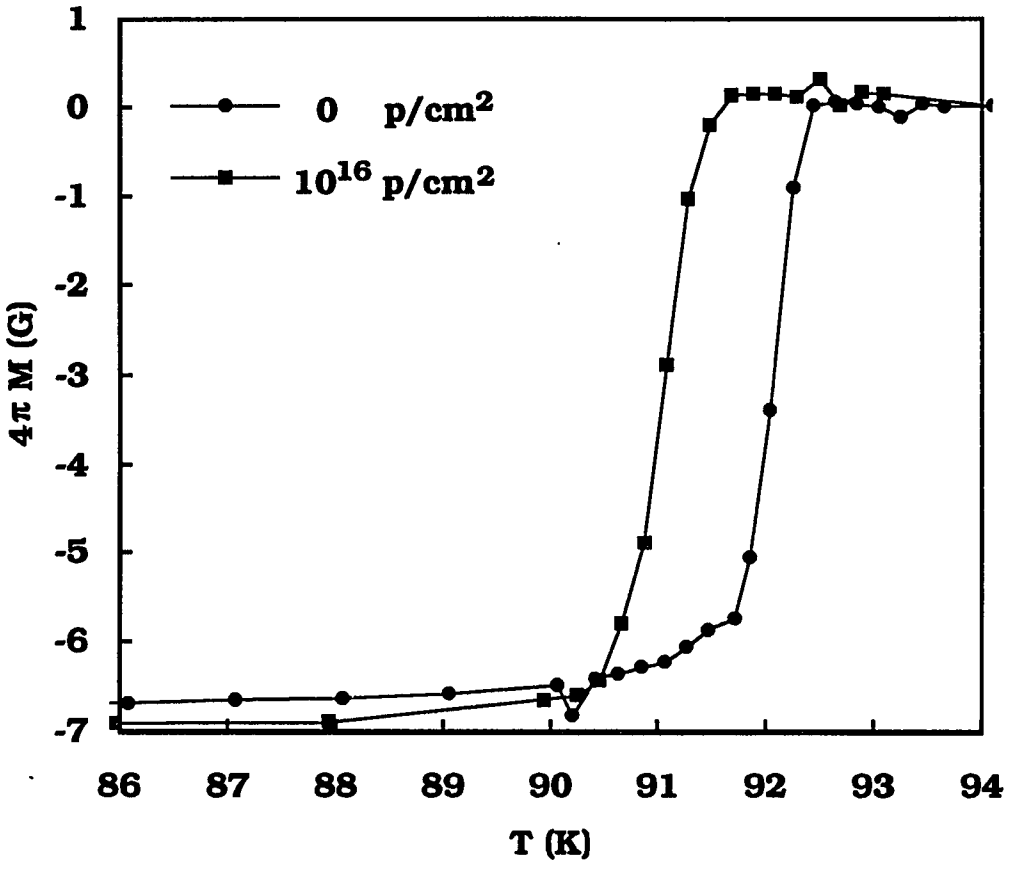

Fig. 4.8 The zero field cool data showing the transition temperature and transition width before and after 10^{16} proton/cm^2 irradiation along the a-b plane of the crystal. The magnetic field was 5 Oe and parallel to the damage tracks. The demagnetization factor was about 0.27.

fluences. The data shown from Fig. 4.8 to Fig. 4.14 were taken from crystal 'B' which came from the same crystal growth batch as the crystal 'A'. As shown in Fig. 4.9, J_c^c at 1 T and 10 K increased from about 23,000 A/cm^2 at 10^{15} protons/cm^2 to 850,000 A/cm^2 at 10^{16} protons/cm^2. For zero field and 10 K, the

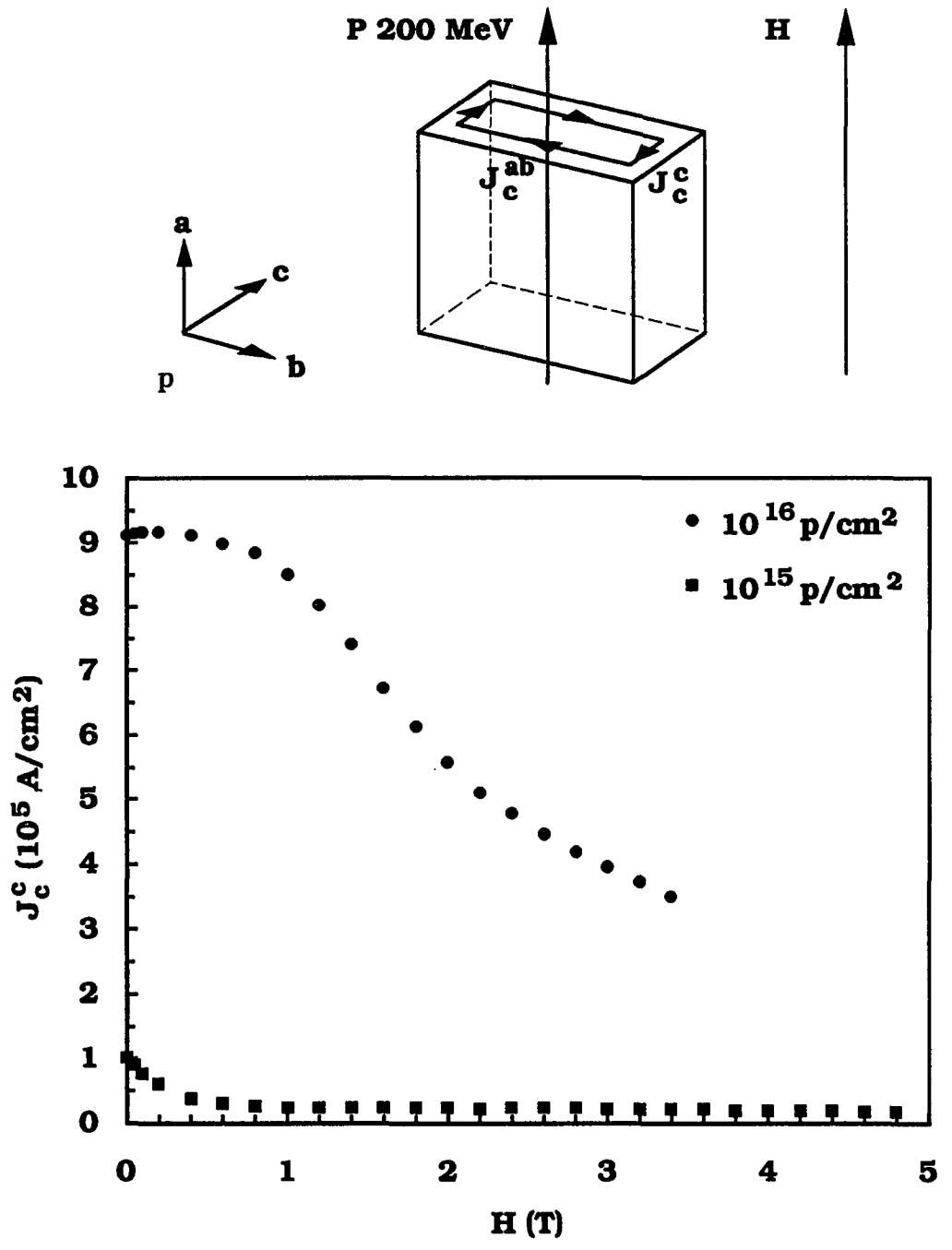

Fig. 4.9 J_c^C enhancement at 10 K with high fluence for radiation parallel to the a-b plane and field parallel to the radiation direction.

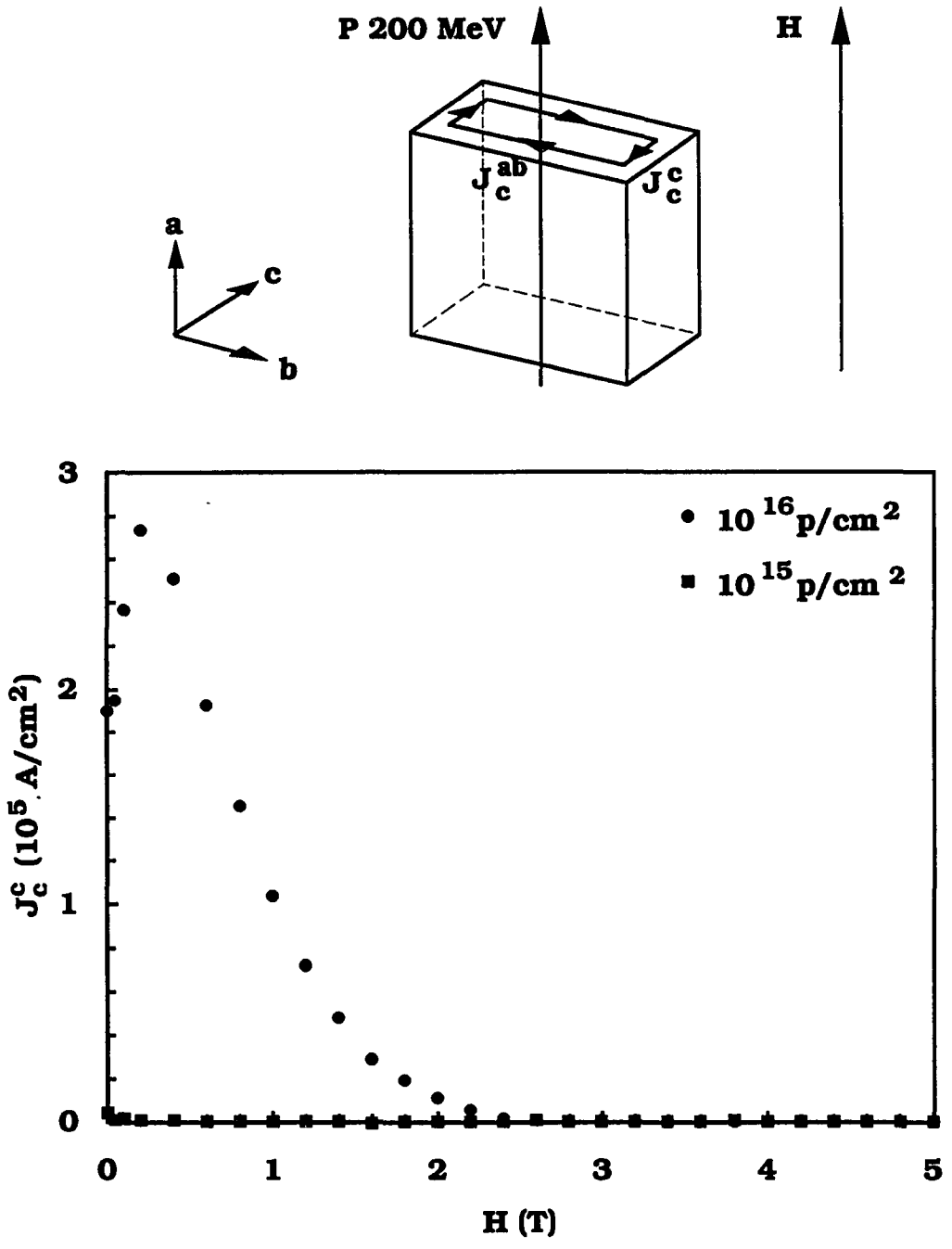

Fig. 4.10 J_c^C enhancement at 77 K with high fluence for radiation parallel to the a-b plane and field parallel to the radiation direction.

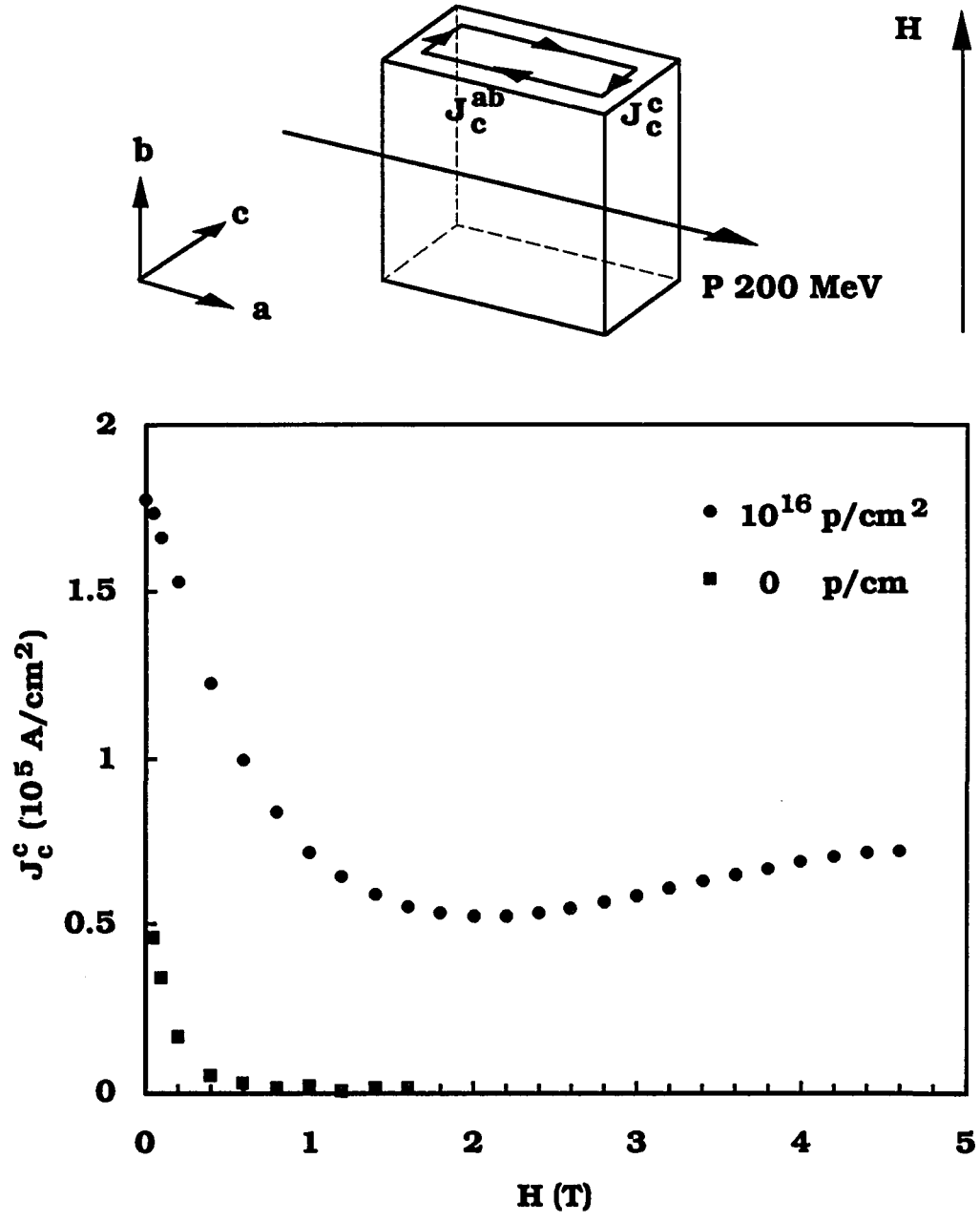

Fig. 4.11 J_C^C at 10 K with high fluence for radiation parallel to the a-b plane and field perpendicular to the damage tracks and also in the a-b plane. The pre-irradiation data (squares) were taken from a different crystal but grown in the same batch.

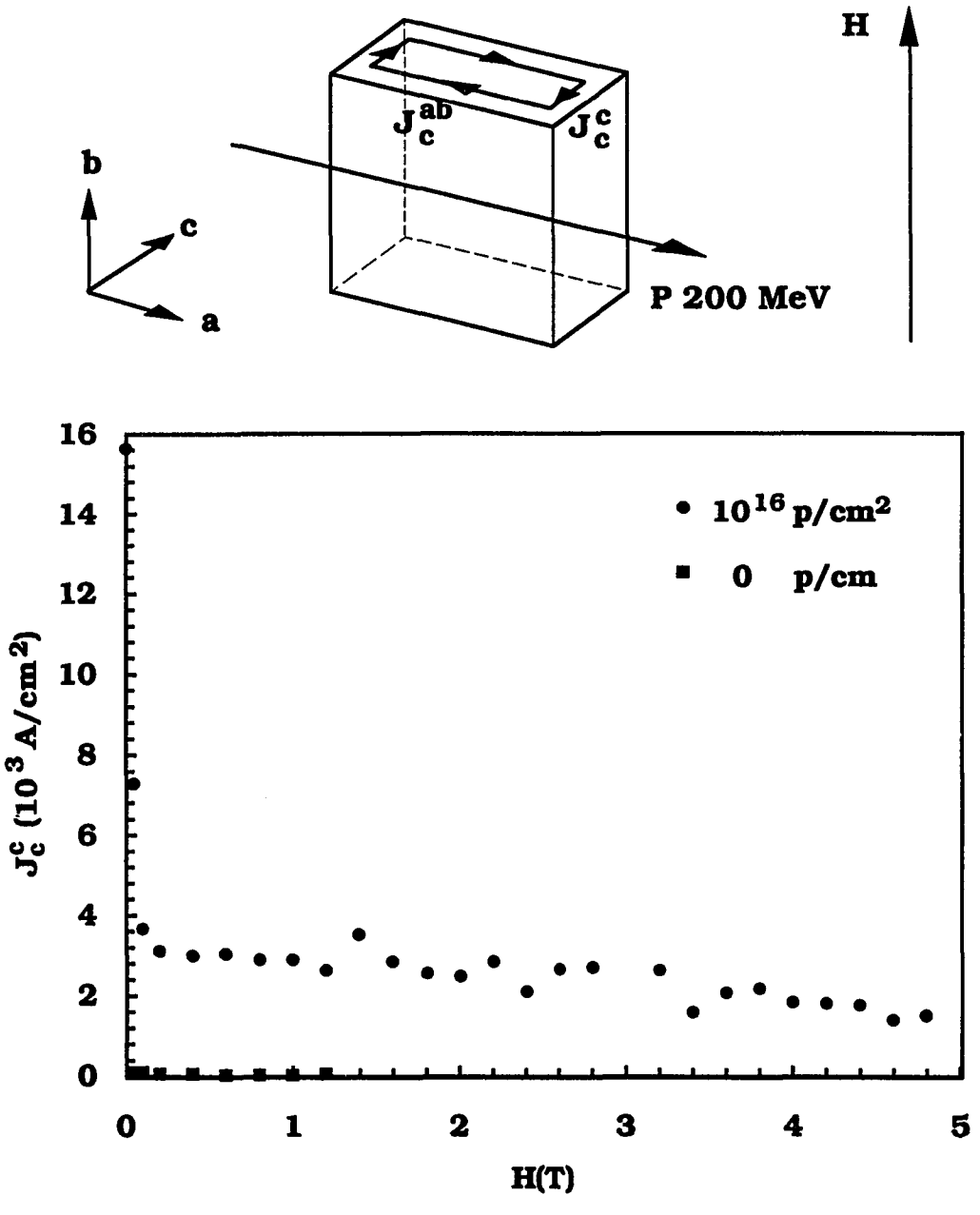

Fig. 4.12 J_C^C at 77 K with high fluence for radiation parallel to the a-b plane and field perpendicular to the damage tracks and also in the a-b plane. The pre-irradiation data (squares) were taken from a different crystal but grown in the same batch.

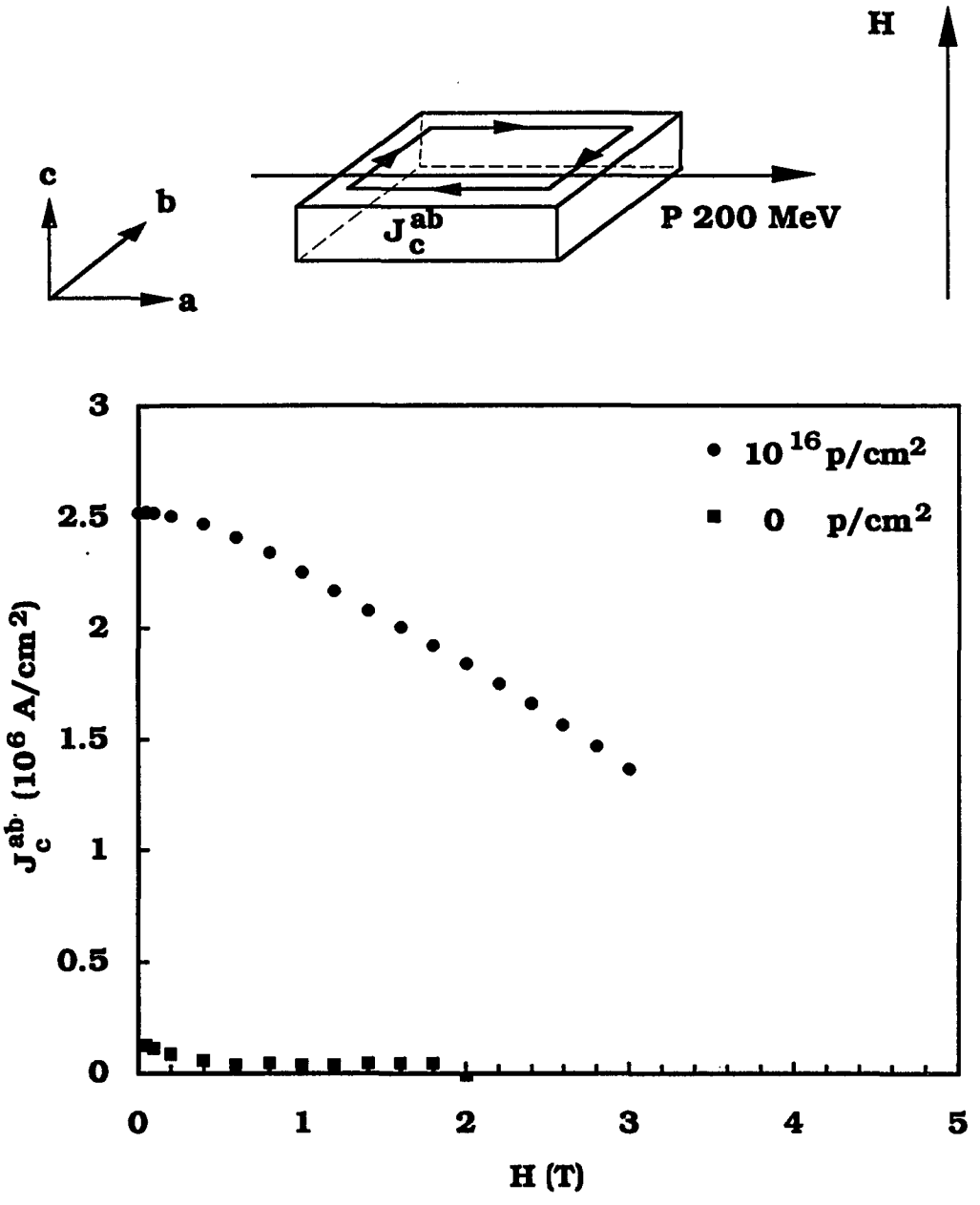

Fig. 4.13 J_c^{ab} enhancement at 10 K with high fluence for radiation parallel to the a-b plane and fields parallel to the c axis.

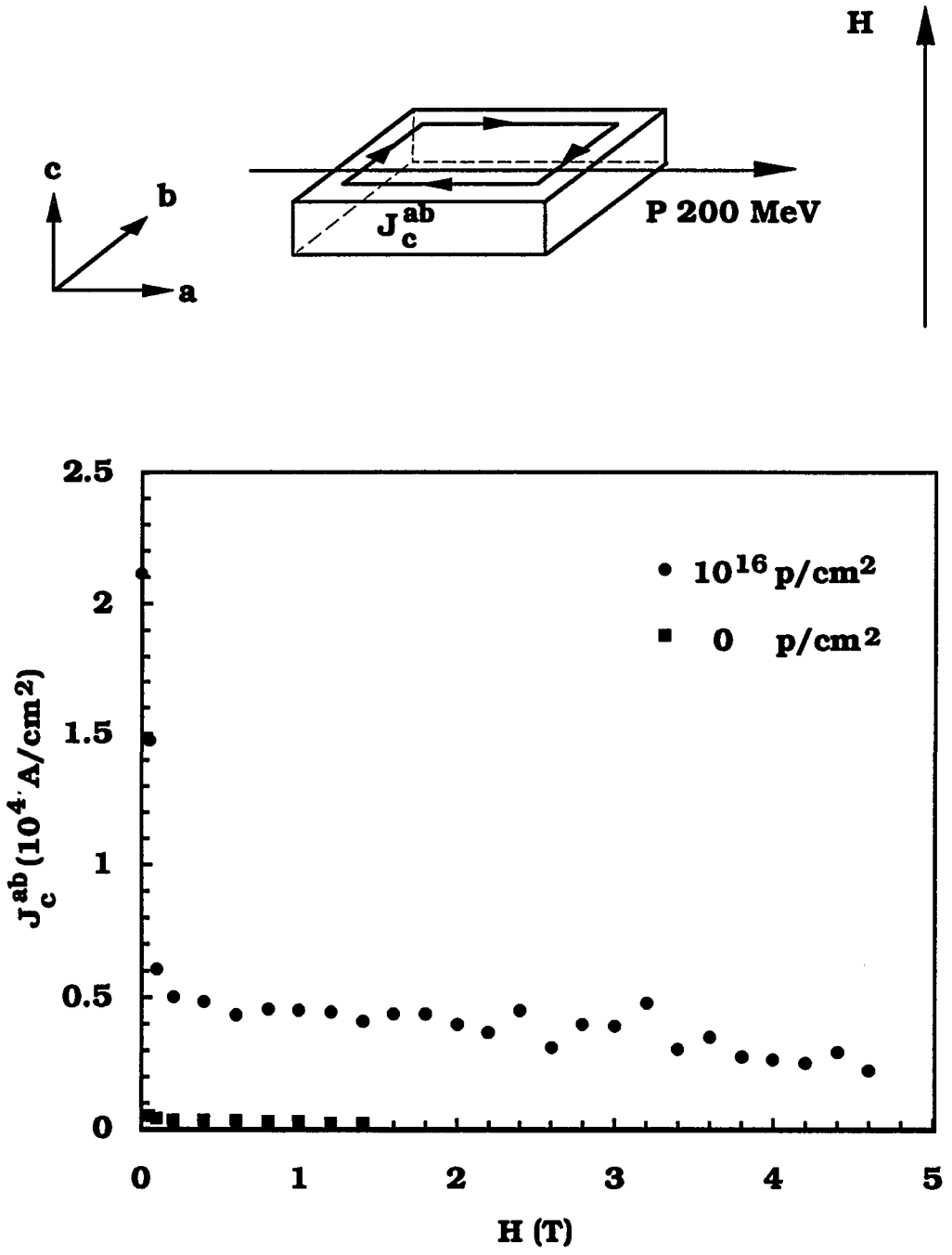

Fig. 4.14 J_c^{ab} enhancement at 77 K with high fluence for radiation parallel to the a-b plane and fields parallel to the c axis.

enhancement at 10^{16} protons/cm^2 was only a factor of 9, but at 1 T it was a factor of 37. Again, these defects were particularly helpful at high field. At high temperature 77 K and 1 T , J_c^c increased from 4000 A/cm^2 at 10^{15} protons/cm^2 to 100,000 A/cm^2 at 10^{16} protons/cm^2, a factor of 25, as shown in Fig. 4.10.

If the magnetic field was rotated in the a-b plane so that the fields were perpendicular to the damage tracks, there was also enhancement to J_c^c by the irradiation. Although the pre-irradiation data for this J_c^c of crystal 'B' were not available, compared with the crystal samples from the same batch, J_c^c at 10 K and 1 T increased from several thousand A/cm^2 at zero fluence to 72,000 A/cm^2 at 10^{16} protons/cm^2, a factor about 10, as shown in Fig. 4.11. At high temperature compared with crystal samples from the same batch, J_c^c at 77 K and 1 T increased from 0 at zero fluence to 2,900 A/cm^{2}at 10^{16} protons/cm^2, as shown in Fig. 4.12. At this high fluence 10^{16} protons/cm^2, the anisotropy in the a-b plane between the two directions parallel and perpendicular to the damage tracks was still quite large. At 1 T and 10 K, J_c^c for field parallel to the damage tracks was larger by a factor about 13 than J_c^c for fields perpendicular to the damage tracks and also in the a-b plane , similar to previous low fluence case in which the anisotropic ratio was 17.

If the magnetic field was directed parallel to the c axis, there was a huge enhancement to J_c^{ab}. As shown in Fig. 4.13, J_c^{ab} at 1 T and 10 K, increased from 37,000 A/cm^2 at zero fluence to 2,300,000 A/cm^2 at 10^{16} protons/cm^2 , a factor of 62. This was not observed in low fluence proton irradiation along the a-b plane. For fluence of 10^{16} protons/cm^2 the damage tracks were very dense. The average spacing of the damage tracks was only 0.1 nm, smaller than all three lattice constants of $YBa_2Cu_3O_{7-\delta}$. It could be that the point defects created along

the damage tracks were so dense in the samples that even when vortices aligned perpendicular to the damage tracks in the c axis still could be pinned by gathering enough point defects in the vortex cores.

In summary, at high fluence 10^{16} protons/cm^2, 200 MeV proton irradiation parallel to the a-b plane enhanced J_c^c very significantly for fields parallel to the damage tracks at 10 K and 77 K. The enhancement of J_c^c was relatively smaller for fields aligned perpendicular to the damage tracks and also in the a-b plane. The enhancement of J_c^{ab} was very significantly for fields parallel to the c axis. At this radiation level, T_c was suppressed by about 1 K.

4.3 Irradiation Parallel To The c Axis

For high fluence 10^{15} and 10^{16} protons/cm^2 proton irradiation parallel to the c axis, the critical current density J_c^{ab} was greatly enhanced when the fields were parallel to the damage tracks. The data shown from Fig. 4.15 to Fig. 4.19 were taken from crystal 'C'. As shown in Fig. 4.15, J_c^{ab} at 10 K and 1 T increased from 570,000 at zero to 1,200,000 at 10^{15}, to 2,100,000 A/cm^2 at 10^{16} protons/cm^2 . At zero field and 10 K, the J_c^{ab} increased by the similar fashion in that it increased by a factor about 2 at 10^{15} protons/cm^2 and by a factor about 3 at 10^{16} protons/cm^2. Thus irradiation parallel to the c axis increased J_c^{ab} quite evenly at both low and high fields. At 77 K and 1 T, J_c^{ab} increase from 0 at zero fluence to 26,000 A/cm^2 at 10^{15} protons/cm^2, to 44,000 A/cm^2 at 10^{16} protons/cm^2 [Fig. 4.16]. It was reported that J_c^{ab} at 77 K and 1 T was enhanced to 17,000 A/cm^2 at 10^{16} protons/cm^2 by 3 MeV proton irradiation parallel to the c axis [L. Civale et al., 1990]. That result was very similar to the result in this

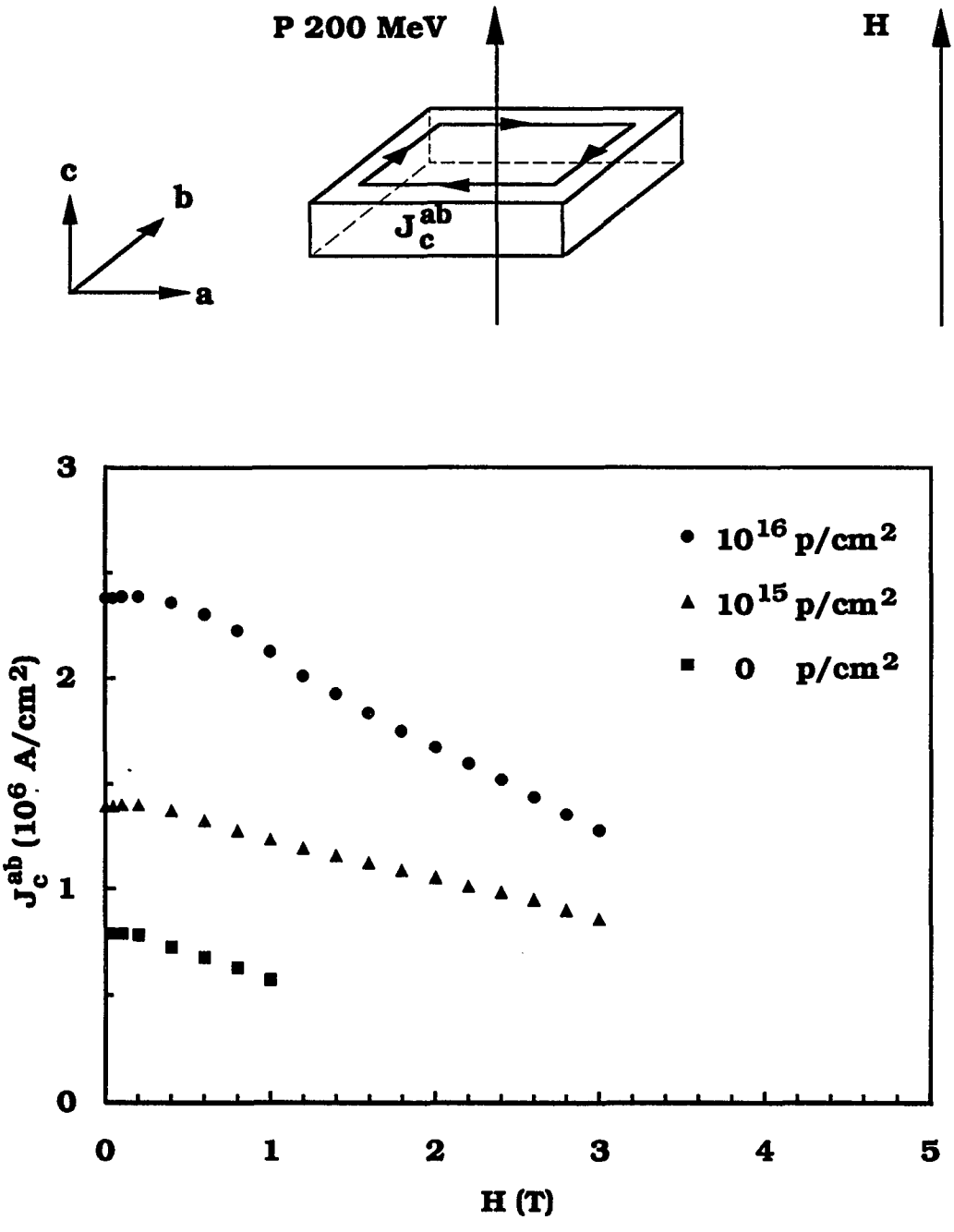

Fig. 4.15 J_c^{ab} enhancement at 10 K with high fluence for radiation parallel to the c axis and fields parallel to the c axis.

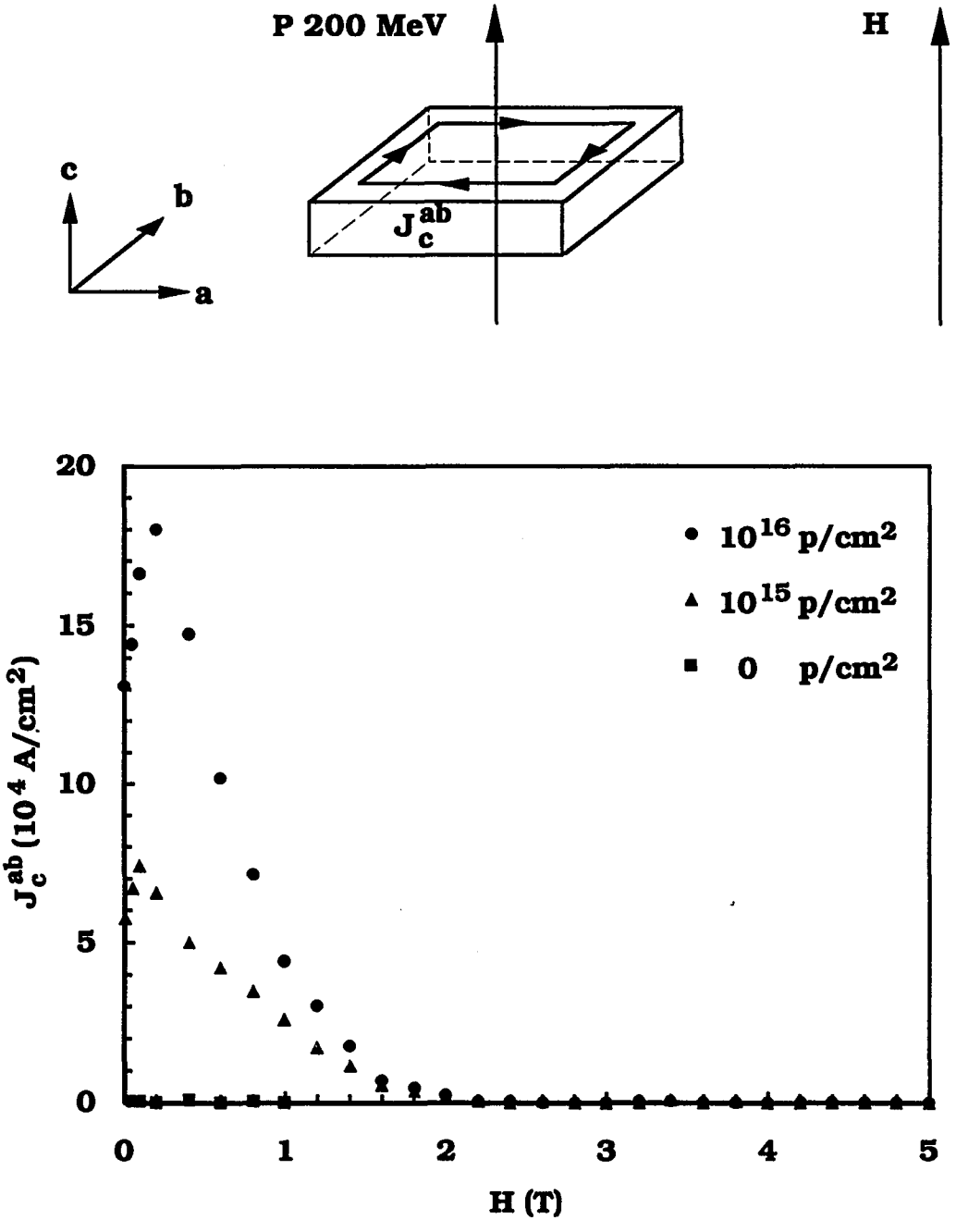

Fig. 4.16 J_c^{ab} enhancement at 77 K with high fluence for radiation parallel to the c axis and fields parallel to the c axis.

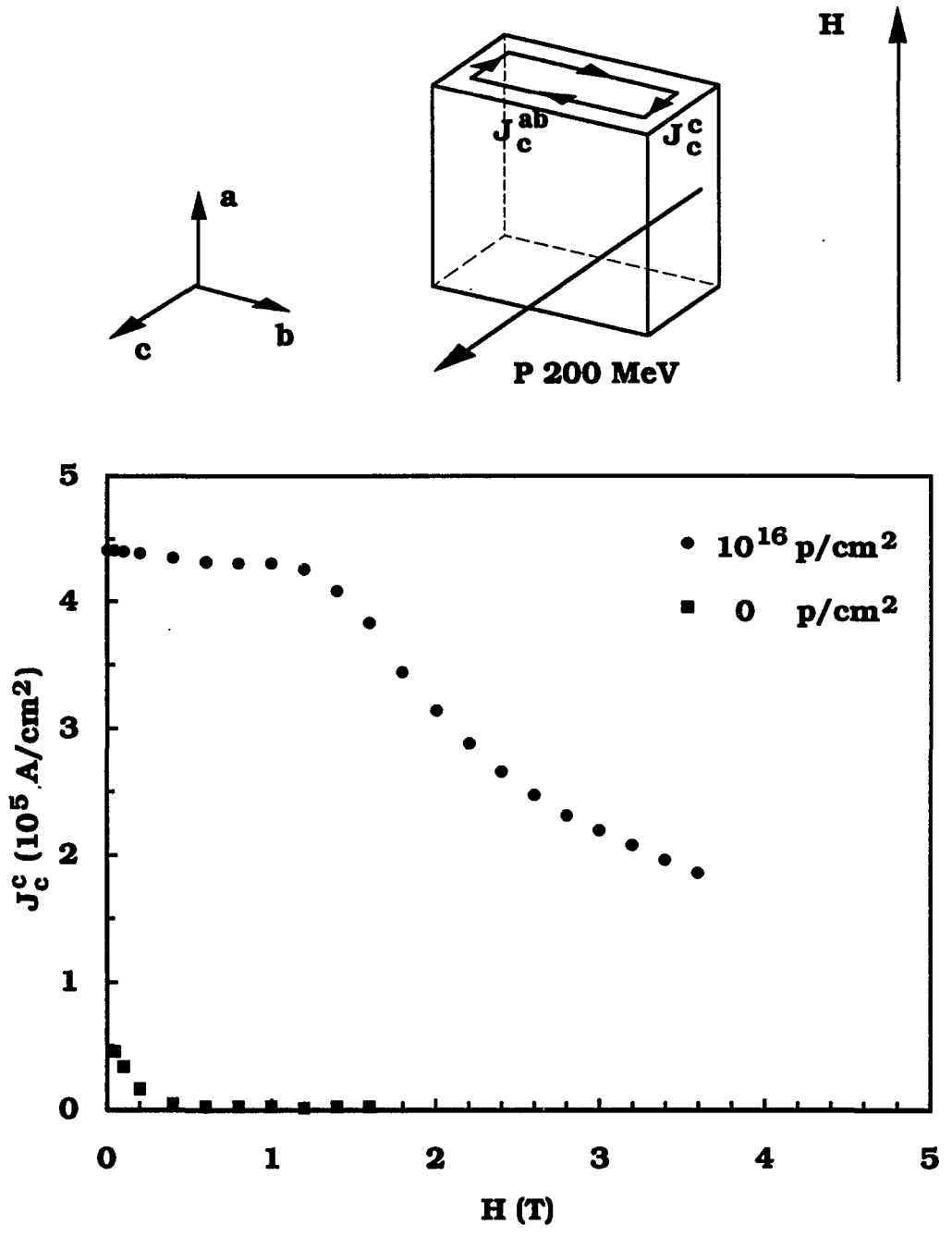

Fig. 4.17 J_C^C at 10 K with high fluence for radiation parallel to the c axis and fields parallel to the a-b plane. The pre-irradiation data (squares) were taken from a different crystal but grown in the same batch.

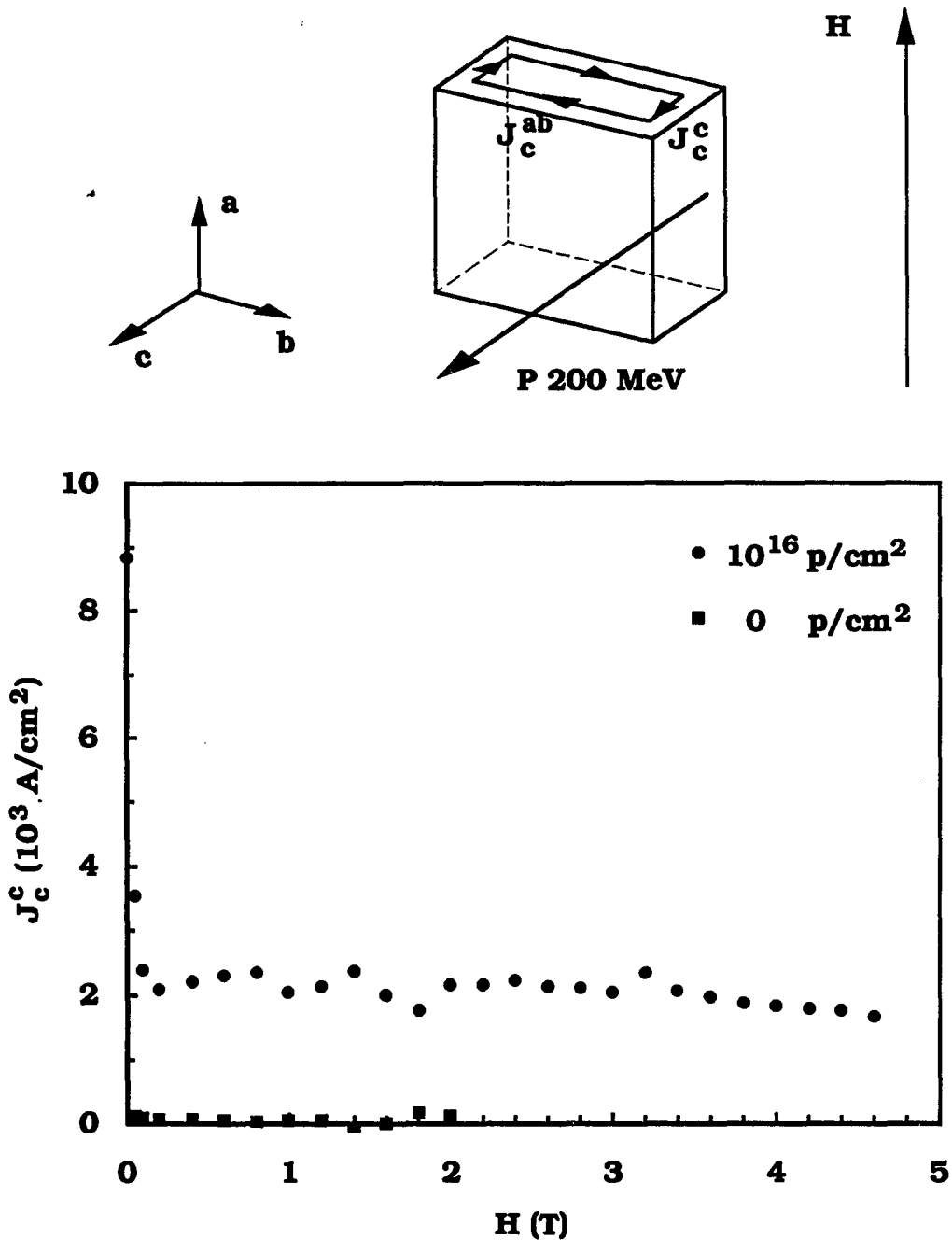

Fig. 4.18 J_c^C at 77 K with high fluence for radiation parallel to the c axis and fields parallel to the a-b plane. The pre-irradiation data (squares) were taken from a different crystal but grown in the same batch.

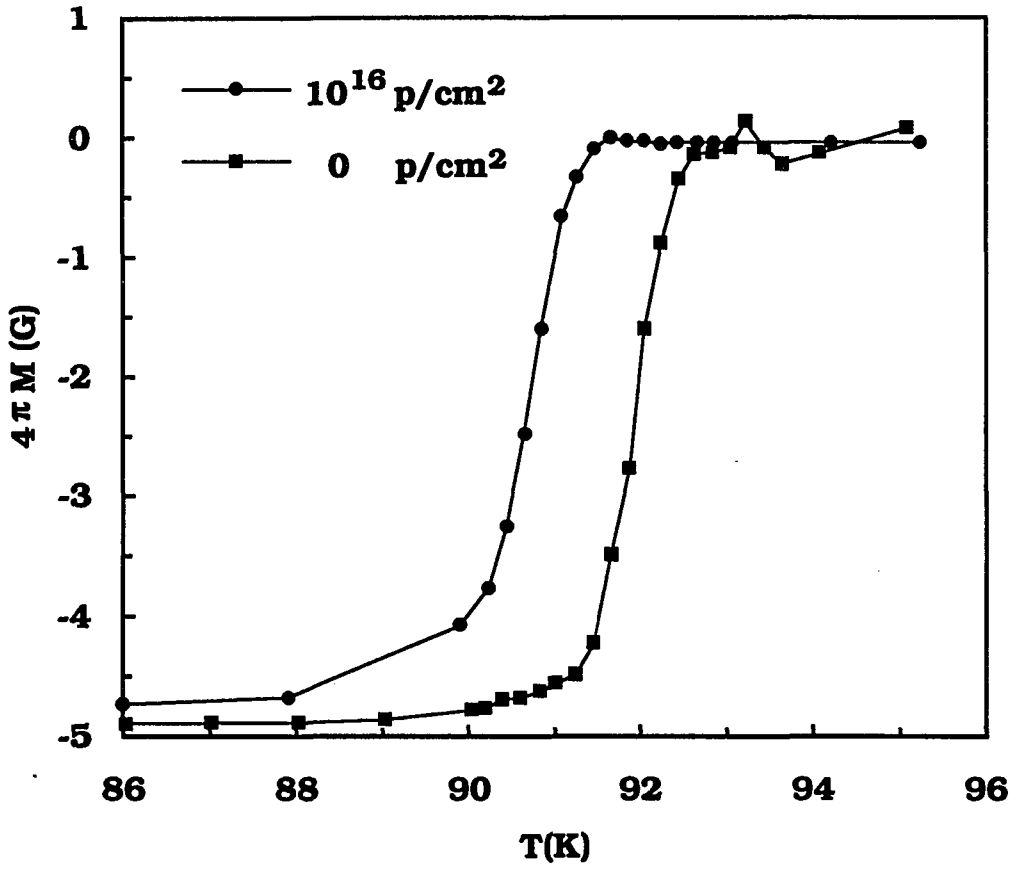

Fig. 4.19 The zero field cool data showing the transition temperature and transition width before and after 10^{16} proton/cm^2 irradiation parallel to the c axis. The magnetic field was 5 Oe and parallel to the c axis also.

experiment, i.e., 44,000 Am/cm^2, considering different crystal growth batches and different energy of proton radiation.

If the magnetic field was directed parallel to the a-b plane, J_c^c was also enhanced significantly by the irradiation. Although the pre-irradiation data was not available, compared with other crystals from the same batch, J_c^c at 10 K and

1 T was increased from several thousand A/cm^2 at zero fluence to 420,000 A/cm^2 at 10^{16} protons/cm^2, about a factor of 100, and J_c^c at 77 K and 1 T was increased for 0 at zero protons/cm^2 to 2000 A/cm^2 at 10^{16} protons/cm^2, as shown in Fig. 4.17 and Fig. 4.18. Comparing the results for fields parallel the c axis and the results for fields perpendicular to the c axis at 10^{16} protons/cm^2, J_c^{ab} at 10 K and 1 T was higher than J_c^c at 10 K and 1 T by a factor 5. The difference for fields parallel to the damage tracks and perpendicular to the damage tracks was quite big.

Also at 10^{16} protons/cm^2, the transition temperature T_c of the crystal sample was suppressed by about 1 K by the irradiation parallel to the c axis [Fig. 4.19]. For fluence lower than 10^{15} protons/cm^2, T_c was not suppressed by the irradiation parallel to the c axis. This result was very similar to the T_c suppression by the irradiation parallel to the a-b plane at 10^{16} protons/cm^2.

For fluence lower than 10^{14} protons/cm^2, the critical current density J_c^{ab} was not enhanced by the irradiation parallel to the c axis. This was very similar to the result of the irradiation parallel to the a-b plane.

In summary, for high fluence 10^{15} and 10^{16} protons/cm^2, 200 MeV proton irradiation parallel to the c axis increased J_c^{ab} significantly for fields parallel to the c axis. The enhancement for J_c^c was relatively modest for fields parallel to the a-b plane. At 10^{16} protons/cm^2 , T_c was suppressed by 1 K.

4.4 The Annealing Of Enhanced J_c In Room Temperature

If the irradiated samples were allowed to anneal at room temperature for several months, there were significant amount of change in both J_c^c and J_c^{ab}. As

discovered in the TEM study of pre-thinned sample, the point defects created by 200 MeV proton irradiation were very mobile in room temperature forming single rows of cluster defects after the irradiation. Some of the point defects by the irradiation could anneal themselves over a period of months because of the mobility.

4.4.1 Low fluence annealing

For low fluence 10^{14} protons/cm^2 irradiation parallel to the a-b plane, the annealing of J_c^c for fields parallel to the damage tracks was very rapid. As shown in Fig. 4.20, J_c^c at 10 K and 1 T decreased from 170,000 A/cm^2 to 16,000 A/cm^2 5 months after the enhancement by irradiation. Although it was still 8 times higher than the pre-irradiation value, the decrease was a factor about 10. As shown in Fig. 4.21, J_c^c at 77 K and 1 T decreased from 1,900 A/cm^2 to 200 A/cm^2 5 months after the enhancement by irradiation. Although it was still higher than the pre-irradiation value which was too small to measure, the decrease was at least a factor of 10. Thus the rate of J_c^c decrease for fields parallel to the damage tracks at 10 K and 77 K was about the same.

If the magnetic field was rotated in the a-b plane so that the field was perpendicular to the damage tracks, the critical current density J_c^c annealed only small amount. As shown in Fig. 4.22, J_c^c at 10 K and 1 T decreased from 12,000 A/cm^2 to 10,000 A/cm^2 5 months after the enhancement by the irradiation, only 17%. Compared this result with the second curve in Fig. 4.20, it was obvious that the rotation of the field in the a-b plane by 90° only change J_c^c at 10 K and 1 T by a factor of 1.6 five months after the irradiation at 10^{14} protons/cm^2. This

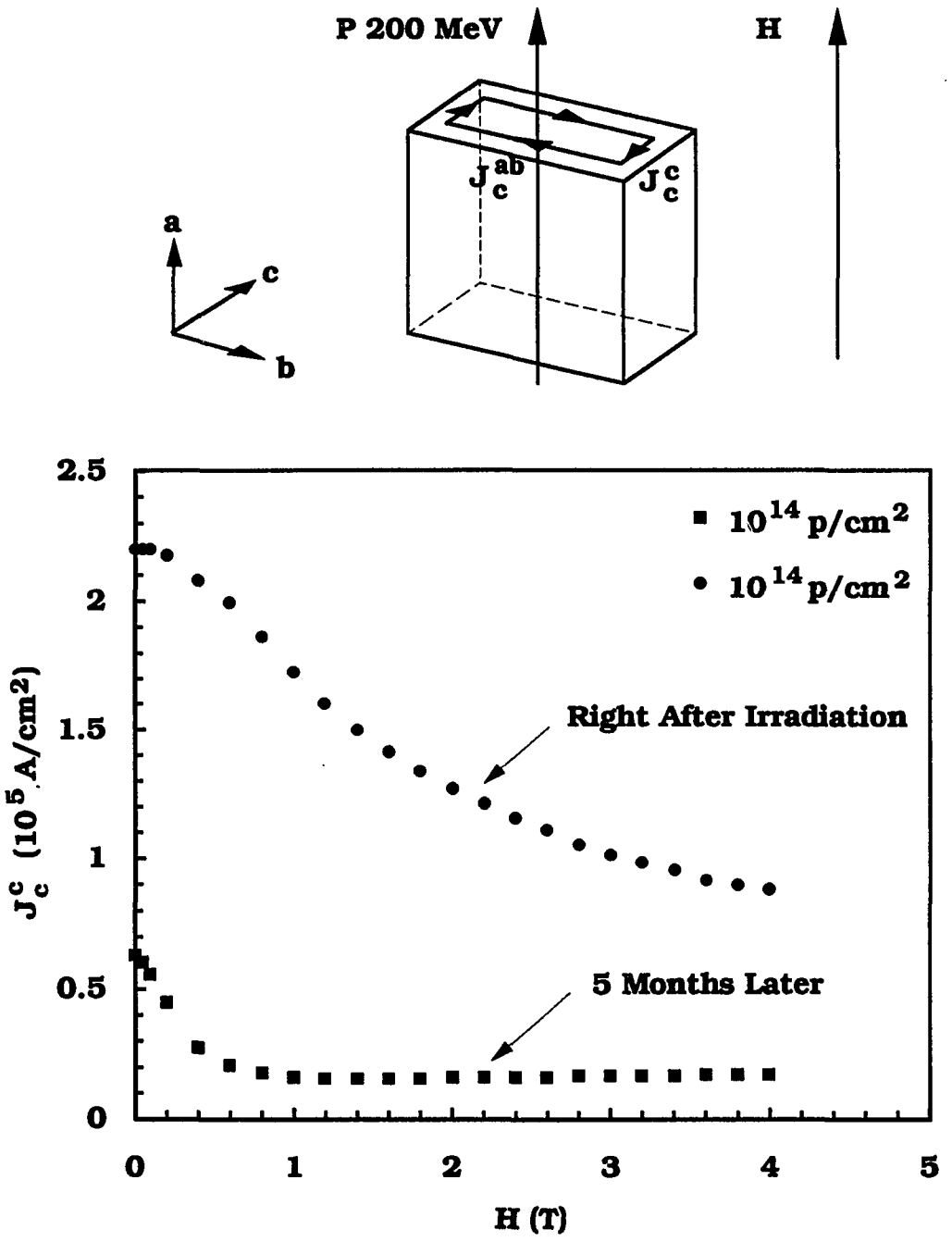

Fig. 4.20 J_c^C decrease at 10 K for fields parallel to the damage tracks after the enhancement by low fluence proton irradiation parallel to the a-b plane.

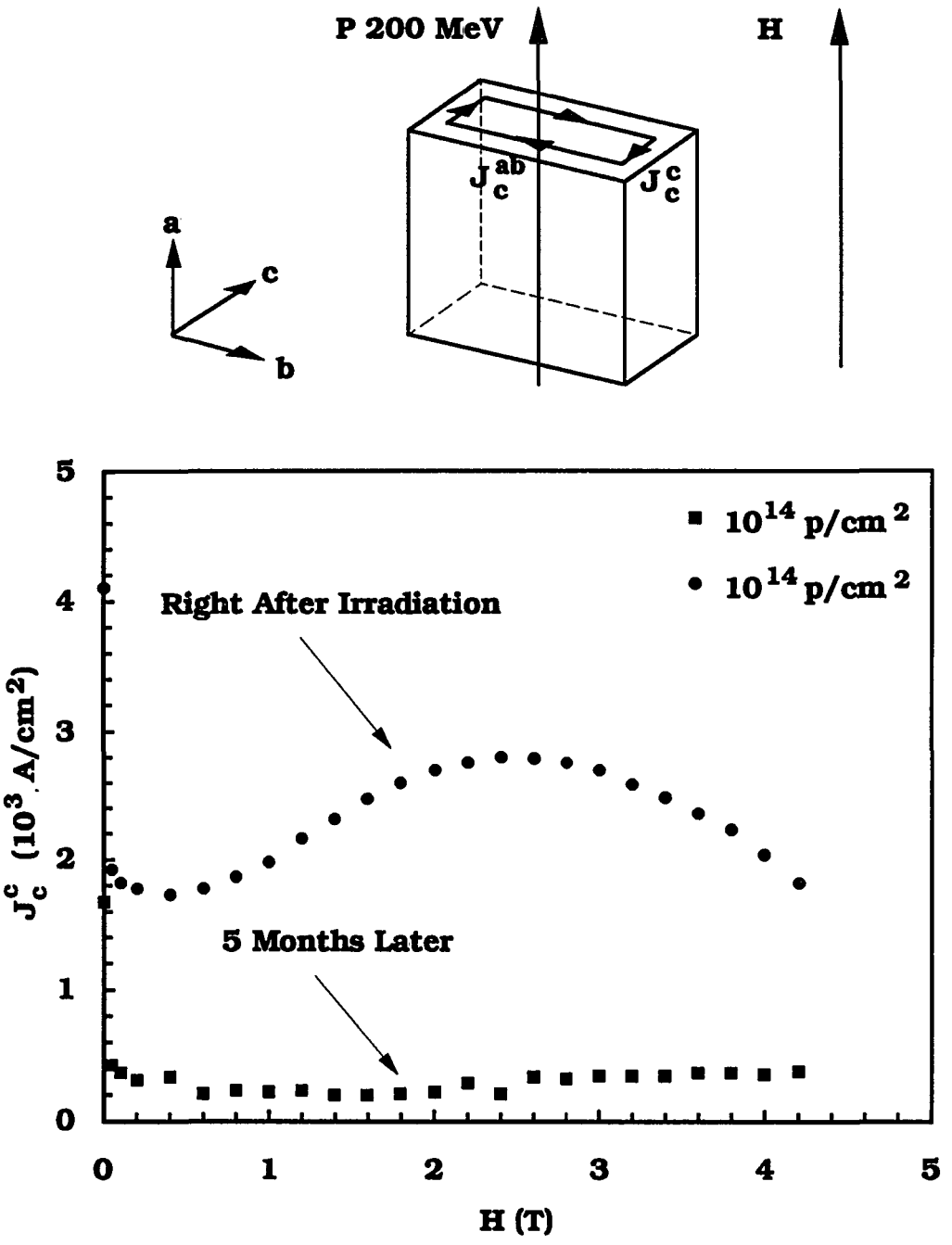

Fig. 4.21 J_C^C decrease at 77 K for fields parallel to the damage tracks after the enhancement by low fluence proton irradiation parallel to the a-b plane.

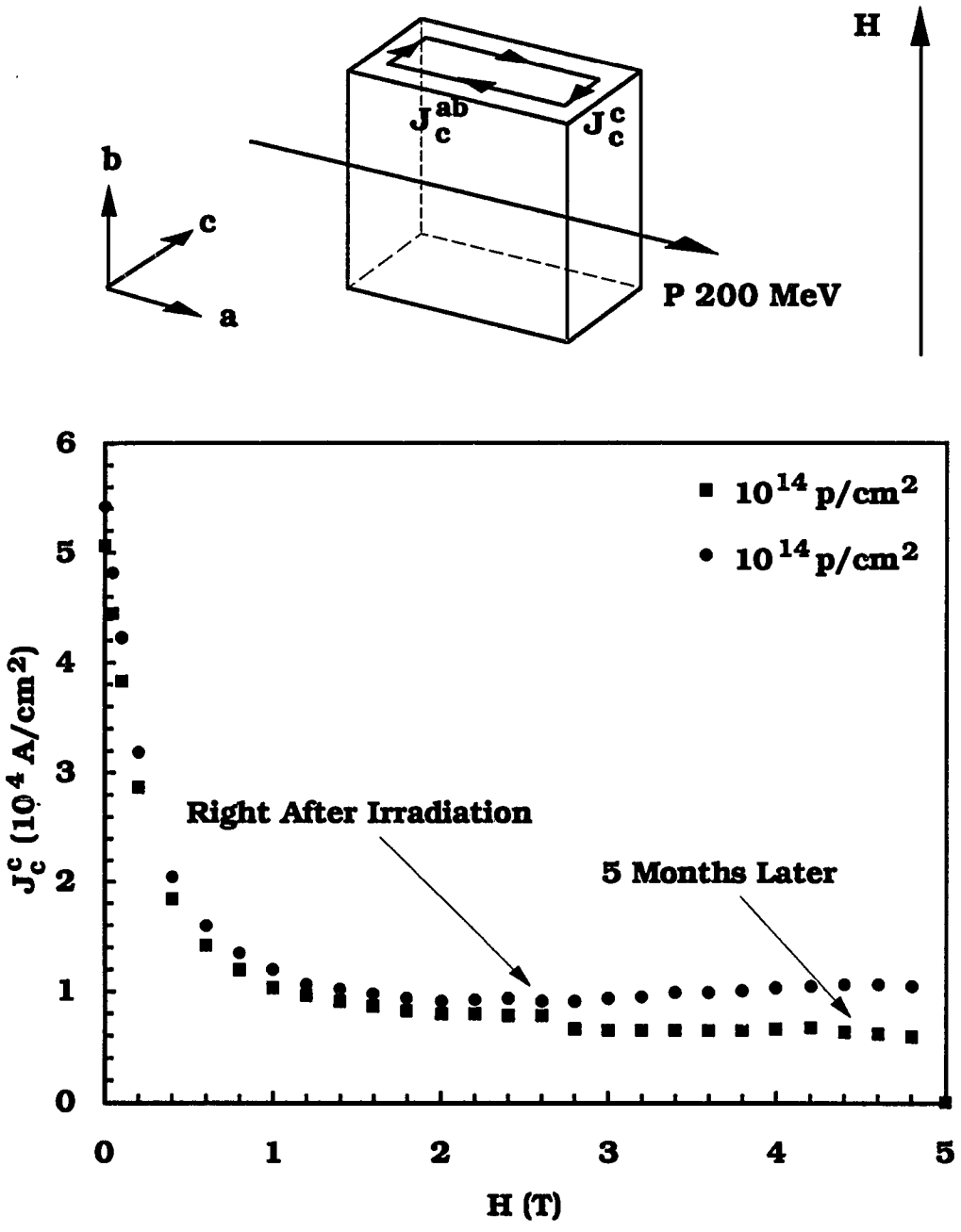

Fig. 4.22 J_C^C decrease at 10 K for fields parallel to the a-b plane and also perpendicular to the damage tracks after the enhancement by low fluence proton irradiation parallel to the a-b plane.

anisotropy ratio was much smaller than the result right after the irradiation which was 17.

In summary, at this low fluence 10^{14} protons/cm^2, the average track spacing was 1 nm much larger than the average atomic spacing which was 0.1 nm. Therefore, the track nature of the irradiation damage could be lost by the motion of the point defects perpendicular to the damage tracks. That was likely responsible to rapid decrease of J_c^c for fields parallel the damage tracks. The anisotropy in the a-b plane between the two directions parallel and perpendicular to the damage tracks thus became less pronounced and the point defects created by the irradiation distributed more uniformly 5 months after the irradiation damage.

4.4.2 High fluence annealing

For high fluence 10^{16} protons/cm^2 irradiation parallel to the a-b plane, the annealing of J_c^c for fields parallel to the damage tracks was modest. As shown in Fig. 4.23, J_c^c at 10 K and 1 T decreased from 850,000 A/cm^2 to 580,000 A/cm^2 5 months after the enhancement by irradiation, about 32%.

If the magnetic field was rotated in the a-b plane so that the field was perpendicular to the damage tracks, the critical current density J_c^c also annealed a modest amount. As shown in Fig. 4.24, J_c^c at 10 K and 1 T decreased from 72,000 A/cm^2 to 31,000 A/cm^2, about 57%. This meant that 5 months after the irradiation at 10^{16} protons/cm^2 the rotation of the field in the a-b plane by 90° change J_c^c at 10 K and 1 T by a factor of 19 , comparable with the result right after the irradiation which was 13.

At this high fluence 10^{16} protons/cm^2, the average track spacing was 0.1 nm approximately the same as the average atomic spacing which was about

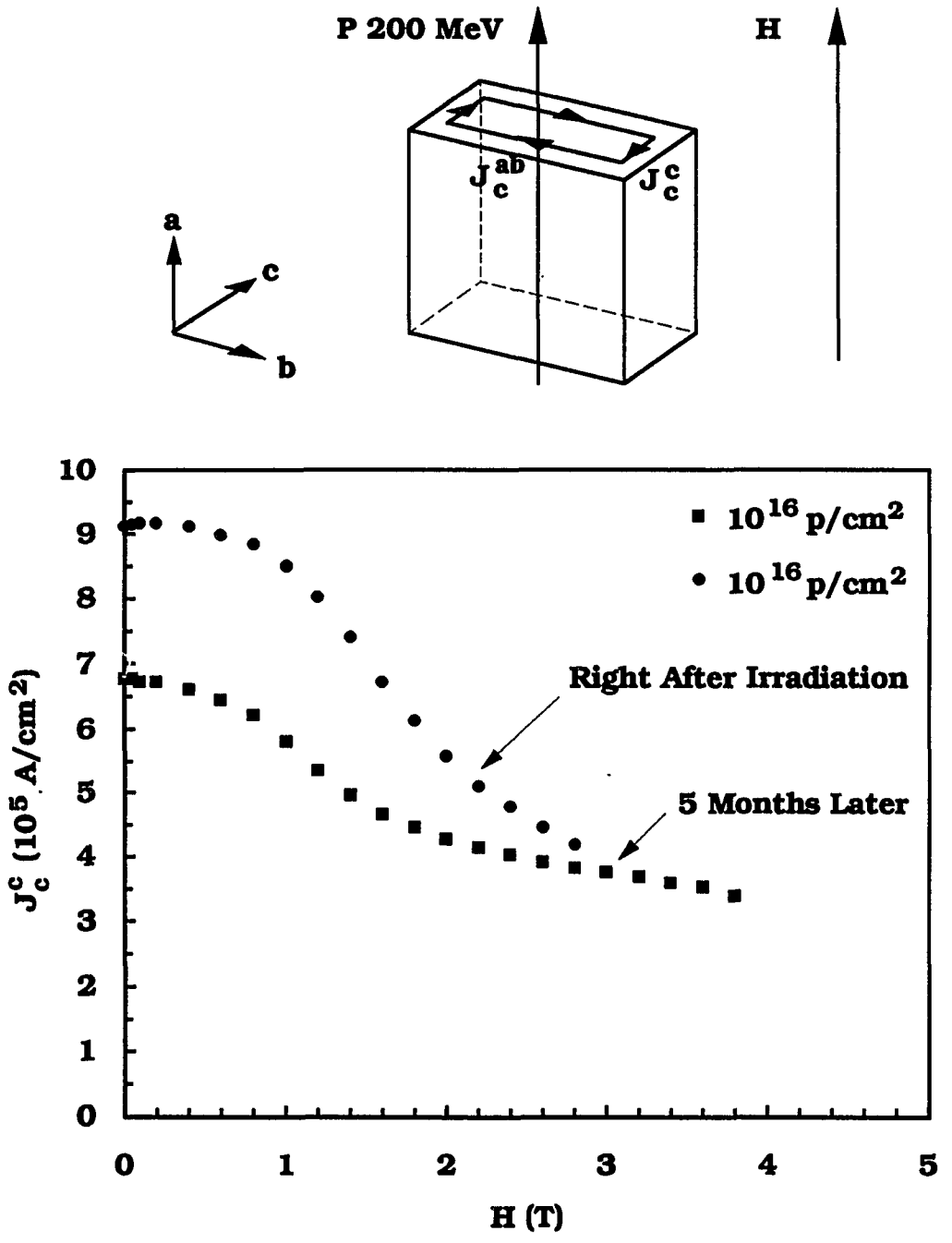

Fig. 4.23 J_c^C decrease at 10 K for fields parallel to the damage tracks after the enhancement by high fluence proton irradiation parallel to the a-b plane.

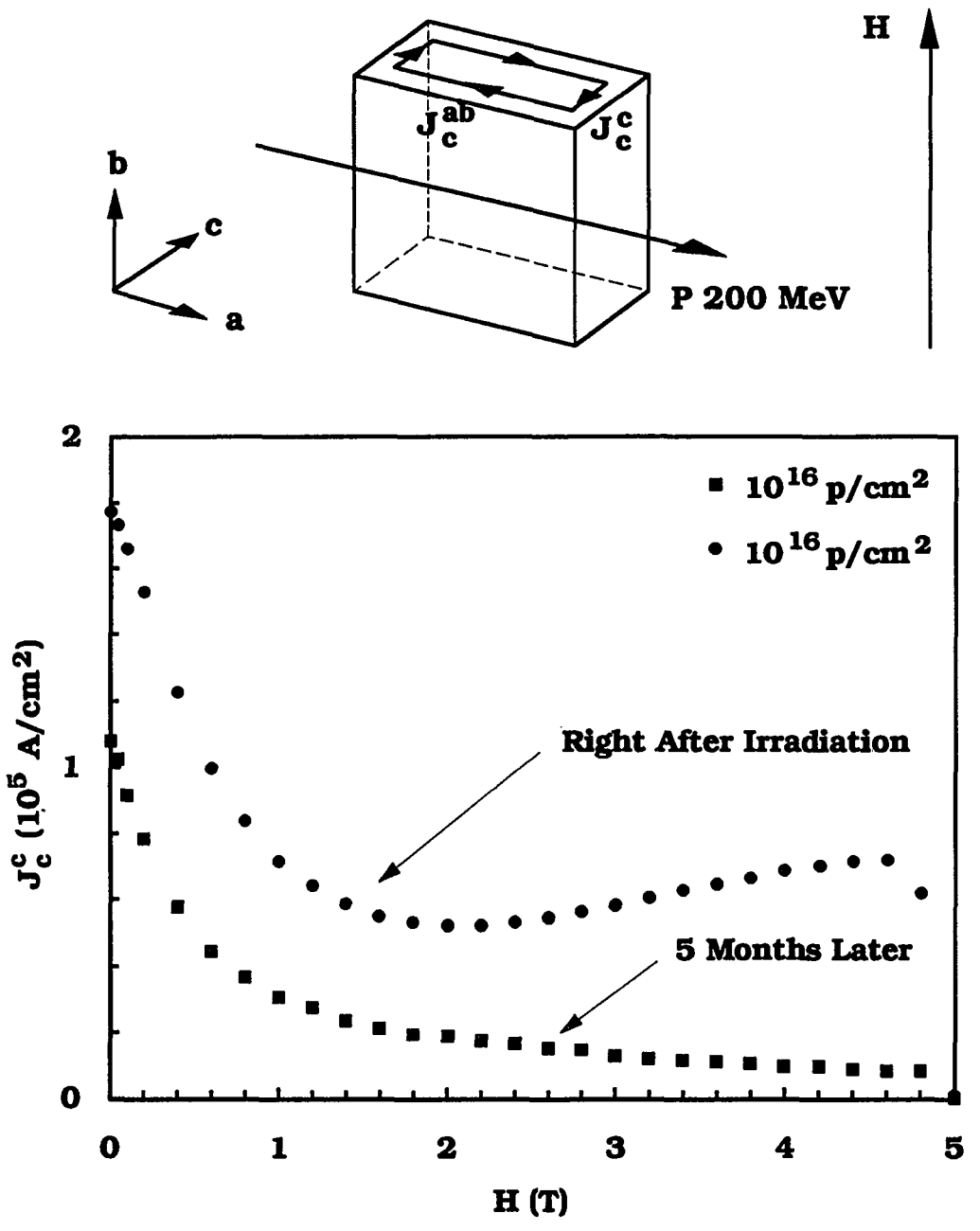

Fig. 4.24 $J_C{}^C$ decrease at 10 K for fields parallel to the a-b plane and also perpendicular to the damage tracks after the enhancement by high fluence proton irradiation parallel to the a-b plane.

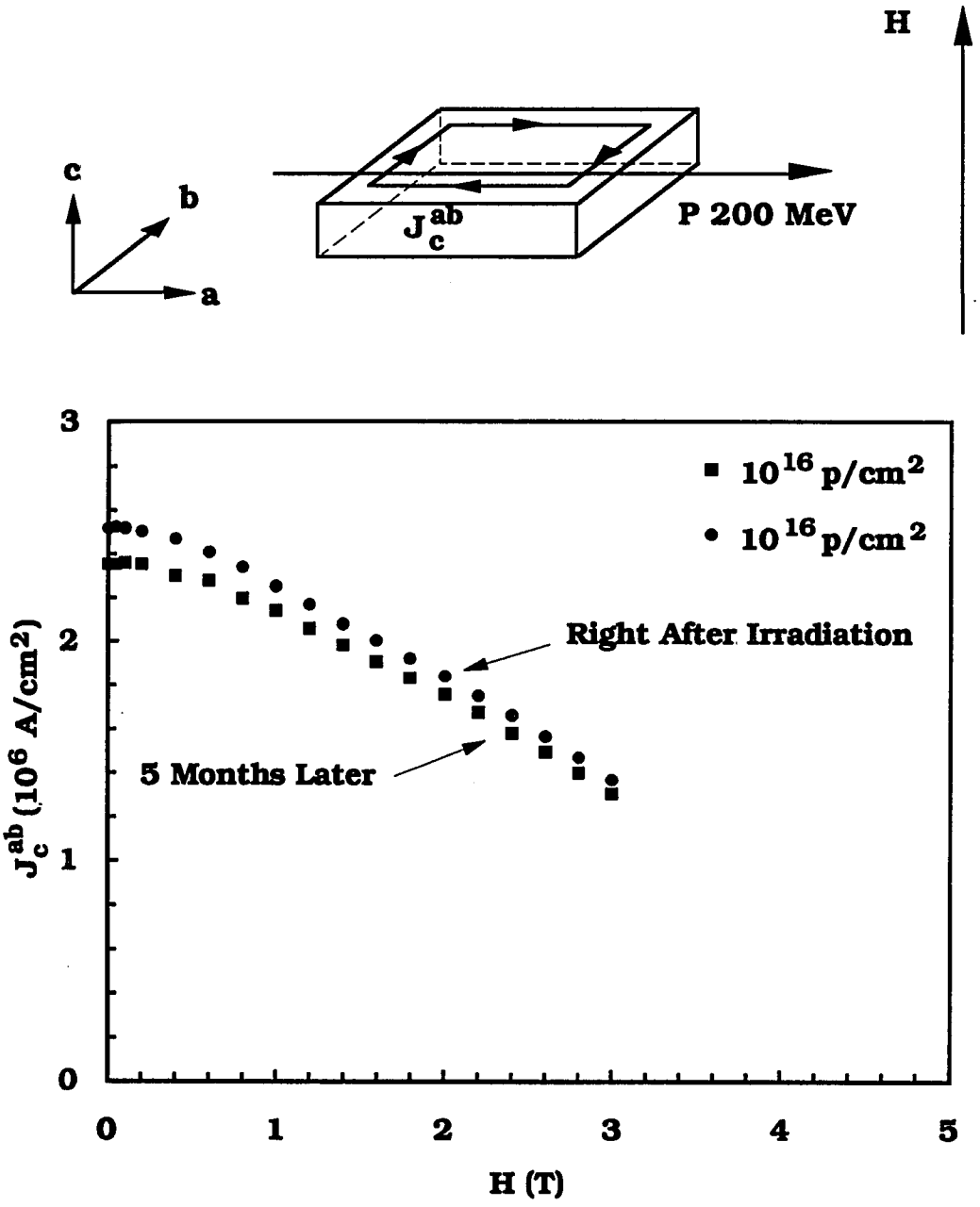

Fig. 4.25 J_c^{ab} decrease at 10 K for fields parallel to the c axis after the enhancement by high fluence proton irradiation parallel to the a-b plane.

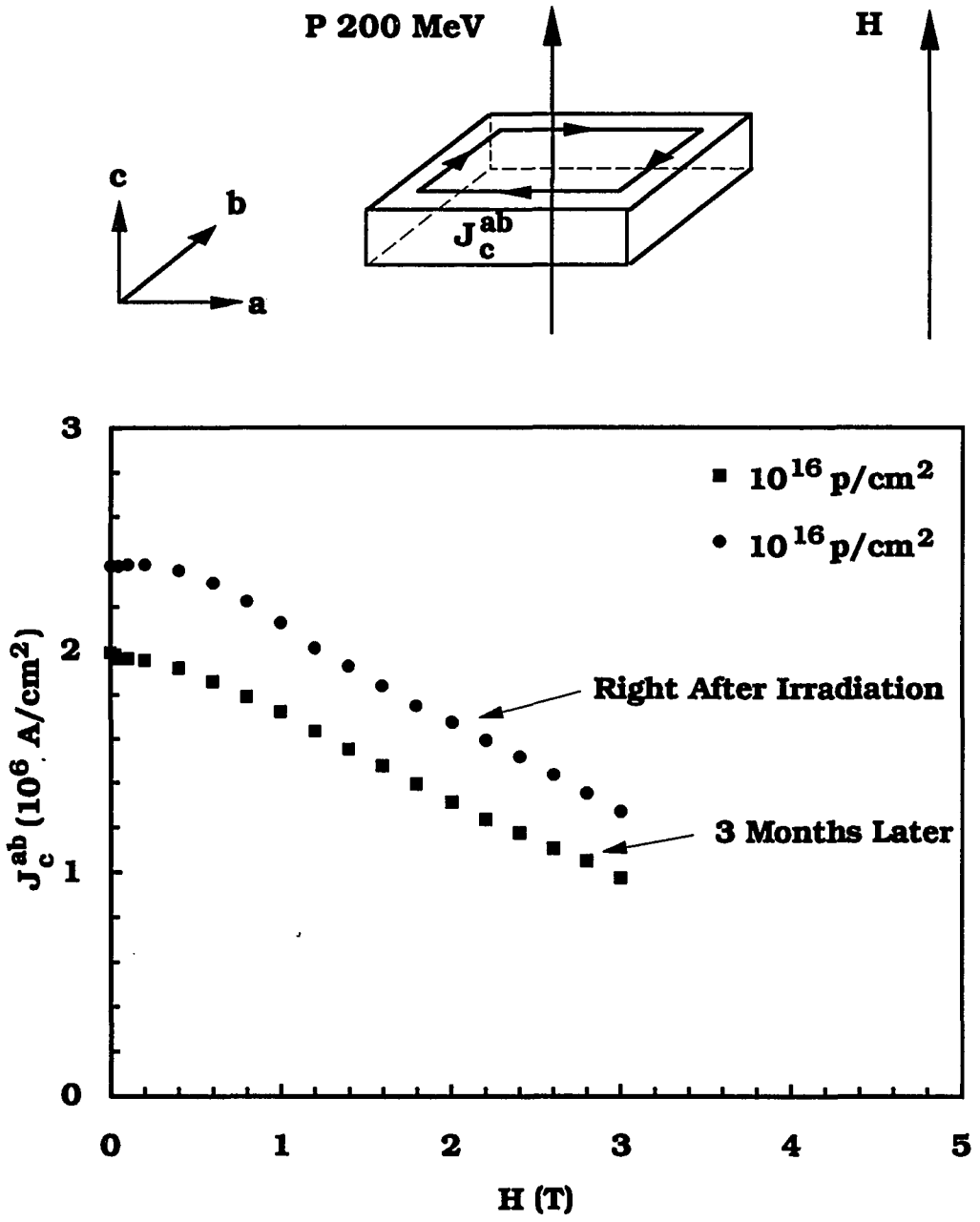

Fig. 4.26 J_c^{ab} decrease at 10 K for fields parallel to the c axis after the enhancement by high fluence proton irradiation parallel to the c axis.

0.1 nm. Therefore, the track nature of the irradiation damage could not be lost by the motion of the point defects either perpendicular or parallel to the damage tracks. The decrease of J_c^c was likely due to the decreasing of the point defect density because of the annealing.

If the magnetic field was directed to the c axis, the critical current density J_c^{ab} for fields parallel to the c axis decreased only slightly with long anneals. As shown in Fig. 4.25, J_c^{ab} at 10 K and 1 T decreased from 2,300,000 A/cm^2 to 2,200,00 A/cm^2 5 months after the enhancement by irradiation, only 5%. Because the damage tracks was perpendicular to the field direction, the decrease of J_c^{ab} was likely due to the decreasing of the point defect density because of the annealing.

For high fluence 10^{16} protons/cm^2 irradiation parallel to the c axis, the annealing of J_c^{ab} for fields parallel to the c axis was modest. As shown in Fig. 4.26, J_c^{ab} at 10 K and 1 T decreased from 2,100,000 A/cm^2 to 1,700,000 A/cm^2 3 months after the enhancement by irradiation, about 26%. Again, because the average damage track spacing was approximately the same as the atomic spacing, the track nature of the irradiation damage could not be lost by the motion of the defects, the decrease of J_c^{ab} thus was very likely due to the decreasing of point defect density because of the annealing.

In summary, at high fluence 10^{16} protons/cm^2, the annealing of critical current density was about 5 to 57% several months after the enhancement by the irradiation. The decrease was very likely due to the annealing of the point defects instead of the loss of the track nature of the defects.

4.5 The Length Scale Of The Crystal

Even though the samples used in this experiment were single crystals, it was possible that there were internal defect distributions that would cause the samples to show granular behavior. This internal granularity could be studied using the 'reverse leg' of the magnetization loop discussed in section 2.3.3. A crystal from the same batch as the crystal 'A', 'B', 'C' was examined for the granularity. The dimensions of the crystal were typically $0.56 \times 0.37 \times 0.31$ mm^3. As shown in Fig. 4.27, the 'reverse legs' of the magnetization had approximately the same slopes at various fields as predicted by Eq. 2.47 or Eq. 2.50. These slopes were the measures of the length scale of the crystal. When measuring the initial slopes of the 'reverse legs' of the magnetization, the increase of the magnetization by initial field decrement of several tens of Gauss was at the same level as the increase due to flux creeping during the time of measurements. As result of flux creeping, the 'reverse legs' of the magnetization were no longer linear in field, but very like logarithmic in field. This could be understood if one realized the time intervals between the measurements were approximately the same and flux creeping effect was equally strong. To avoid this flux creeping effect in the 'reverse leg' measurement, a hysteresis pause of 1 hour was given at each field before reversing the field. As shown in Fig. 4.28, the slopes of the 'reverse legs' were linear in field except a little trace of curvature due to flux creeping. As shown in Table 4.1, the length scales of the crystal from analyzing these data by Eq. 2.47 or Eq. 2.50 were larger than the half of geometric average of the crystal ($\sqrt{ab}\,/\,2 = 0.23$ mm). This discrepancy was expected because the crystal was thick and square instead of thin and circular as assumed in the theory.

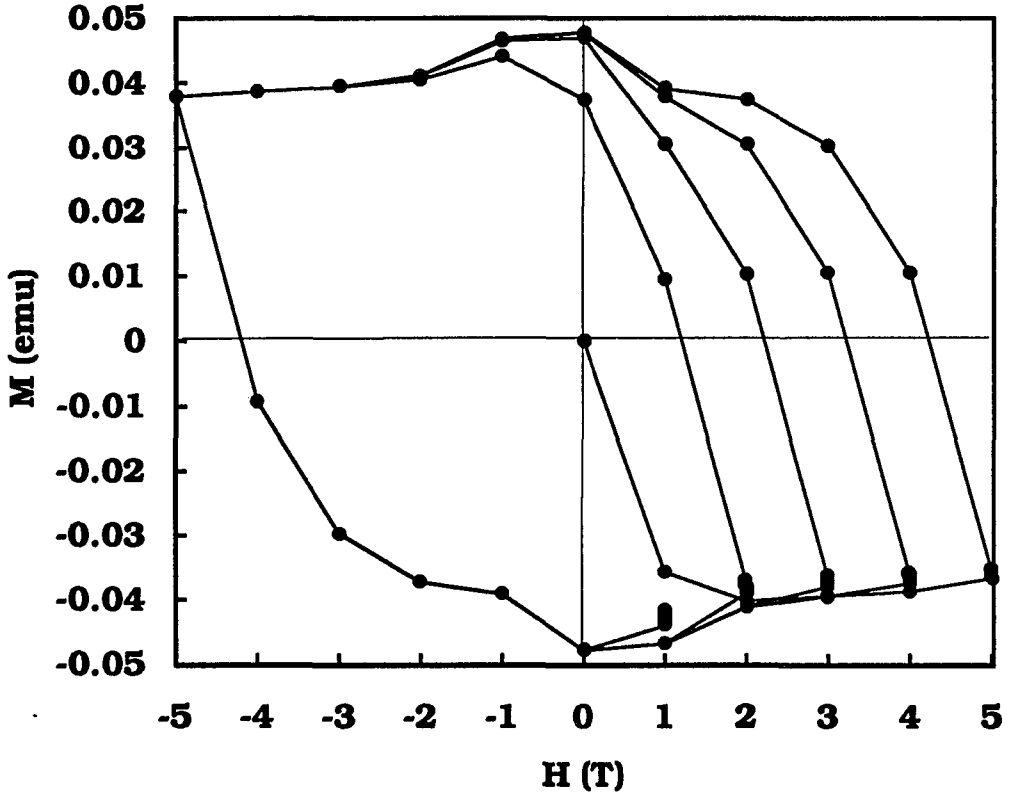

Fig. 4.27 A hysteresis loop of a single crystal showing constant slopes of the 'reverse legs' at different fields. The field was parallel to the c axis.

In summary, the crystals in our experiment were fully connected up to 5 T field. There were no granularities in these crystals. The use of physical dimensions in the Bean model to derive critical current densities was justified.

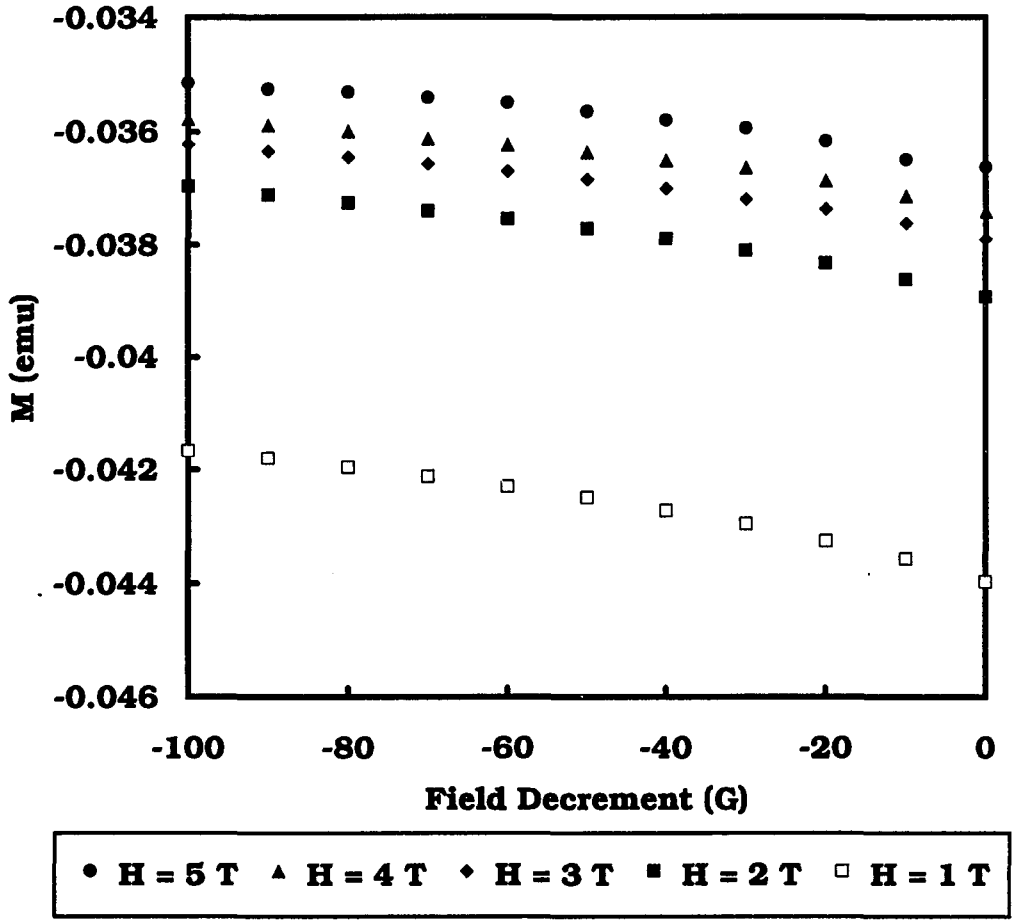

Fig. 4.28 The initial 'reverse legs' of the magnetization shown linear behavior and constant slope at fields of 5, 4, 3, 2, 1 Tesla respectively.

Table 4.1 The Length Scale of the Crystal from the Measurement of the 'Reverse Leg' of the Magnetization.

H (T)	dm/dH (emu/T)	R by Eq. 2.47 (mm)	Λ by Eq. 2.50 (mm)
1	-1.7×10^{-5}	0.33	0.59
2	-1.5×10^{-5}	0.31	0.49
3	-1.3×10^{-5}	0.29	0.42
4	-1.3×10^{-5}	0.29	0.41
5	-1.2×10^{-5}	0.29	0.38

The crystal length: a = 0.56 mm

The crystal width: b = 0.37 mm

The crystal thickness: c = 0.31 mm

The length scale of the crystal = $\sqrt{ab}$ / 2 = 0.23 mm

CHAPTER 5. CONCLUSIONS

In this experiment, a series of $YBa_2Cu_3O_7$ single crystals were irradiated by 200 MeV protons along two major symmetry axes with various fluence for 10^{12} to 10^{16} proton/cm^2. The critical current densities were enhanced to certain levels depending on the fluence of the radiation and the direction of the currents.

For low fluence (10^{12}-10^{14} protons/cm^2) radiation parallel to the a-b plane, the critical current density J_c^c for field parallel to the damage tracks was greatly enhanced. There was a steady rise in J_c^c at 10 K and 1 T from 50,000 to 220,000 A/cm^2 as the fluence increased from 0 to 10^{12} to 10^{13} to 10^{14} protons/cm^2. A strong anisotropy in J_c^c was observed in the a-b plane. A typical ratio of J_c^c for a parallel field to a perpendicular field with respect to the damage track direction was about 17 at 10 K and 1 T. For low fluence radiation parallel to the c axis, the critical current density remained constant.

For high fluence (10^{16} protons/cm^2) radiation parallel the a-b plane, the critical current density J_c^c at 10 K and 1 T was enhanced even more to 900,000 A/cm^2 when the fields were parallel to the damage tracks. The anisotropy in J_c^c in the a-b plane was still strong. A typical ratio of J_c^c for a parallel field to a perpendicular field with respect to the damage track direction was about 13 at 10 K and 1 T . When the fields were rotated parallel to the c axis, J_c^{ab} the critical current density that could be carried out in the a-b plane was greatly enhanced also to a typical value of 2,500,000 A/cm^2 at 10 K and 1 T. For high fluence radiation parallel to the c axis, the critical current densities J_c^{ab} and J_c^c were both greatly enhanced when fields were either parallel or perpendicular to the

damage tracks. There was a steady rise in J_c^{ab} at 10 K and 1 T from 570,000 to 2,100,000 A/cm^2 as the fluence increased from 0 to 10^{15} to 10^{16} protons/cm^2. J_c^c was also enhanced to a typical value of 420,000 A/cm^2. The transition temperature of the crystal was suppressed about 1 K at high fluence for irradiation parallel to either the a-b plane or the c axis.

The enhanced critical current densities were not stable in room temperature. They annealed significantly over a typical period of 5 months. For low fluence radiation enhanced critical current density J_c^c, the annealing was very strong. Typically J_c^c at 10 K and 1 T decreased to 1/10 of the enhanced value 5 months after the irradiation when the measuring field was parallel to the damage tracks. For high fluence enhanced critical current densities, the annealing was quite modest when fields were either parallel or perpendicular to the damage tracks. Typically the critical current densities decreased by 5 to 57% of the enhanced values after a few months in room temperature. Therefore, to have a stable enhanced critical current densities by 200 MeV proton irradiation, high fluence was essential.

The crystals used in this experiment were fully connected up to 5 T field. There was no evidence of granularities of the crystals.

REFERENCES

A. A. Abrikosov, Zh. Eksp. Teor. Fiz. **32**, 1442 (1957).

P. B. Allen, in *Physical Properties Of High Temperature Superconductors* , edited by Donald M. Ginsberg, (World Scientific Publishing Co. Pte. Ltd., 1989).

M. A. Angadi, A. D. Caplin, J. R. Laverty and Z. X. Shen, Physica C, **177**, 479 (1991).

G. Balestrino, S. Barbanera, and P. Paroli, Journal of Crystal Growth, **85**, 585 (1987).

J. Bardeen, Rev. Mod. Phys. **34**, 667 (1962).

J. Bardeen, L. N. Cooper, and J. R. Schrieffer, Phys. Rev. **108**, 1175 (1957).

C. P. Bean, Phys. Rev. Lett. **8**, 250 (1962).

C. P. Bean, Rev. Mod. Phys. **36**, 31 (1964).

J. G. Bednorz and K. A. Müller, Z. Phys. B **64**, 189 (1986).

J. P. Biersack, and W. Eckstein, Appl. Phys. A, **34**, 73 (1984).

J. P. Biersack, and L. G. Haggmark, Nuclear Instrument and Methods, **174**, 257 (1980).

A. M. Campbell and J. E. Evetts, *Critical Currents In Superconductors*, (Taylor & Francis Ltd., London, 1972), p. 159.

P. Chaddah, K. V. Bhagwat, and G. Ravikumar, Physica C, **159**, 570 (1989).

D. X. Chen, A Sanchez, and J. S. Munoz, J. Appl. Phys., **67**, 3430 (April, 1990).

D. X. Chen, and R. B. Goldfarb, J. Appl. Phys., **66**, 2489 (1989).

L. Civale, A. D. Marwick, M. W. McElfresh, T. K. Worthington, A. P. Malozemoff, and F. H. Holtzberg, Phys. Rev. B, **65**, 1164 (1990).

L. Civale, M. W. McElfresh, A. D. Marwick, T. K. Worthington, A. P. Malozemoff, F. Holtzberg, C. Feild, J. R. Thompson, D. K. Christen, M. A. Kirk, *Proceedings Of The XII Winter Meeting On Low Temperature Physics*, Cuernavaca, Mexico (Jan. 13-16, 1991).

J. R. Clem, Phys. Rev. B, **43**, 7837 (1991).

R. I. Coote, J. E. Evetts and A. M. Campbell, Can. J. Phys. **50**, 421 (1972).

D. C. Cronemeyer, T. R. McGuire, A. P. Malozemoff, F. Holtzberg, preprint.

M. Daeumling, J. M. Seuntjens and D. C. Larbalestier, Nature, **346**, 332 (July, 1990).

M. A. Damento, K. A. Gschneider, Jr. and R. W. McCallum, Appl. Phys. Lett. **51**, 690 (1987), and U. S. Patent 4,824,826 (April 25, 1989).

B. N. Das, L. E. Toth, A. K. Singh, B. Bender, M. Oskofsky, C. S. Pande, N. C. Koon, and S. Wolf, J. Crystal Growth, **85**, 588 (1987).

T. R. Dinger, T. K. Worthington, W. J. Gallagher, and R. L. Sandstrom, Phys. Rev. B, **58**, 2687 (1987).

G. J. Dolan, G. V. Chandrashekhar, T. R. Dinger, C. Feild, and F. Holtzberg, Phys. Rev. B, **62**, 827 (1989).

W. A. Fietz, M. R. Beasley, J. Silcox, and W. W. Webb, Phys. Rev. A, **136**, 335 (1964).

V. L. Ginzburg and L. D. Landau, Zh. Eksp. Teor. Fiz. **20**, 1064 (1950).

Junho Gohng and D. K. Finnemore, Phys. Rev. B **42**, 7946 (1990).

Frederick W. Grover, *Inductance Calculations*, (Dover Publications, New York, (1962).

E. M. Gyorgy, R. B. van Dover, K. A. Jackson, L. F. Schneemeyer, and J. V. Waszczak, Appl. Phys. Lett. **55** (3), 283 (July, 1989).

K. L. Kaiser, F. Holtzber, B. A. Scott, and T. R. McGuire, Appl. Phys. Lett., **51**, 1040 (1987).

Kenneth L. Keester, J. Crystal Growth, **91**, 295 (1988).

Y. B. Kim, C. F. Hempstead, and A. R. Strnad, Phys. Rev. Lett. **9**, 306 (1962).

Y. B. Kim, C. F. Hempstead, and A. R. Strnad, Phys. Rev., **129**, 528 (1963).

V. G. Kogan, M. M. Fang, and Sreeparna Mitra, Phys. Rev. B, **38**, 11958 (1988).

V. G. Kogan, Phys. Rev. B, **24**, 1572 (1981).

T. Konaka, I. Sankawa, and M. Sato, J. Crystal Growth, **91**, 278 (1988).

M. J. Kramer, Qiang Qian, and D. K. Finnemore, to be published in Physica C (1992)

R. A. Laudise, L. F. Schneemeyer, and R. L. Barns, J. Crystal Growth, 85, 569 (1987).

Byeong-Joo Lee, and Dong Nyung Lee, J. Am. Ceram. Soc., **74**, 78 (1991).

K. S. Lichtenberger, Ph.D. Thesis, Iowa State University, 1991.

C. T. Lin, W. Zhou, W. Y. Liang, E. Schonherr, and H. Bender, Physica C, **195**, 291 (1992).

M. P. Maley, P. J. Kung, J. Y. Coulter, W. L. Carter, G. N. Riley, M. E. McHenry, Phys. Rev. B, **45**, 7566 (1992).

W. Meissner and R. Ochsenfeld, Naturwissenschaften **21**, 787 (1933).

M. J. V. Menken, and A. A. Menovsky, J. Crystal Growth, 91, 264 (1988).

H. K. Onnes, Leiden Comm. **120b, 122b, 124c** (1911)

Akira Ono, and Takaho Tanaka, Jap. J. Appl. Phys. **26**, L825 (1987).

M. S. Osofsky, J. L. Cohn, E. F. Skelton, M. Miller, R. J. Soulen, Jr., S. A. Wolf, and T. A. Vanderah, Phys. Rev. B, **45**, 4916 (1992).

R. L. Peterson, preprint (1990).

Qian Qiang, M. J. Kramer, and D. K. Finnemore, submitted to Applied Superconductor Conference, Chicago, Aug. 23-28, 1992.

J. P. Rice, B. G. Pazol, D. M. Ginsberg, T. J. Moran, and M. B. Weissman, J. Low Temp. Phys. **72**, 345 (1988).

A. C. Ross-Innes and E. H. Rhoderick, *Introduction to Superconductivity* (Pergamon Press, Inc. Oxford, 1988).

F. M. Sauerzoph, H. P. Wiesinger, and H. W. Weber, Cryogenics, **30**, 650 (July, 1990).

H. J. Scheel, and P. Holba, J. Crystal Growth,

S. Senoussi, M. Oussena, G. Collin, and I. A. Campbell, Phys. Rev. B, 37, 9792 (June, 1988).

Humihiko Takei, Hiroyuki Takeya, Yasuhiro Iye, Tsuyoshi Tamegai and Fumiko Sakai, Jap. J. Appl. Phys., **26**, L1452 (1987).

M. Tinkham, *Introduction to Superconductivity*, (McGraw-Hill, New York, 1975), p. 246.

M. Tuominen, A. M. Goldman, Y. Z. Chang, and P. Z. Jiang, Phys. Rev. B, **42**, 412 (1990).

A. Umezawa, G. W. Crabtree, J. Z. Liu, H. W. Weber, W. K. Kwok, L. H. Nunez, and H. Claus, Phys. Rev. B, **36**, 7151 (1987).

Joao L. Vargas, and David C. Larbalestier, Appl. Phys. Lett., **60**, 1741 (April, 1992).

B. D. Weaver, M. E. Reeves, G. P. Summers, R. J. Soulen, W. L. Olson, M. M. Eddy, T. W. James, and E. J. Smith, Appl. Phys. Lett., **59**, 2600 (1991).

H. W. Weber, and G. W. Crabtree, in *Studies Of High Temperature Superconductors*, edited by A. V. Narlikar (Nova Science Publisher, New York, 1991).

U. Welp, S. Fleshler, W. K. Kwok, J. Downey, Y. Fang, G. W. Crabtree, and J. Z. Liu, to be published in Phys. Rev. B, (July, 1990).

M. K. Wu, J. R. Ashburn, C. J. Torng, P. H. Hor, R. L. Meng, L. Gao, Z. J. Huang, Y. Q. Wang, and C. W. Chu, Phys. Rev. Lett. **58**, 908 (1987).

Youwen Xu, M. Suenaga, A. R. Moodenbaugh, and D. O. Welch, Phys. Rev. B **40**, 10882 (1989).

J. F. Ziegler, J. P. Biersack, U. Littmark, *The Stopping And Range Of Ions In Solids*, (Pergamon Press, Inc., Oxford, 1985), p. 13.

ACKNOWLEDGMENTS

I'd like to express my deepest gratitude to professor Douglas K. Finnemore for his kindness, patience and encouragement in guiding me through this Ph. D. program. Working and studying under his supervision have been very enjoyable throughout my graduate school years. I also would like to thank Jerry Ostenson for his generously teaching of many skills and techniques needed in the experiments. I would like to extend my thanks to Dr. Ming Xu for many enlightening discussions and intimate friendship. I thank Dr. John Clem, Dr. V. Kogan, Dr. D. Lewis, Dr. C. Stassis, Dr. D. Johnston, Dr. K. Gshneidner and Dr. B. Young for their time and efforts spent on my graduate committee. I thank Dr. Steve Sanders, Dr. Okbae Hyun, Dr. Qiang Li, Dr. Karl Lichtenberger, and Junghyun Sok for their friendship and aids in various occasions.

Finally, I thank to my parents for their love and support. I thank my dearest friend Hsiao-chin Liu for her love and companionship that make me capable of finishing this work.

This work was performed at Ames Laboratory under contract No. W-7405-eng-82 with the U. S. Department of Energy. The United States government has assigned the DOE Report number IS-T 1452 to this thesis.